Computer Modelling of Positive Electrode Materials for Lithium and Sodium Batteries

Clark, John

Award date:
2014

Awarding institution:
University of Bath

Computer Modelling of Positive Electrode Materials for Lithium and Sodium Batteries

Submitted by

John Matthew Clark

for the degree of Doctor of Philosophy of the

University of Bath

Department of Chemistry

May 2014

Contents

List of Figures

List of Tables

Abstract

Providing cleaner sources of energy will require significant improvements to the solid-state materials available for energy storage and conversion technologies. Rechargeable lithium and sodium batteries are generally regarded as the best available candidates for future energy storage applications, particularly with regard to implementation within hybrid or fully electric vehicles, due to their high energy density. However, production of the next generation of rechargeable batteries will require significant improvements in the materials available for the cathode, anode and electrolyte. Modern computer modelling techniques enable valuable insights into the fundamental defect, ion transport and voltage properties of battery materials at the atomic level. Polyanionic framework materials are being investigated as alternative cathodes to $LiCoO_2$ in Li-ion batteries largely due to their greater stability, cost and environmental benefits. In this thesis, four types of polyanion materials are examined using computational techniques. Firstly, the pyrophosphate material, $Li_2FeP_2O_7$ is investigated, which has the highest voltage (3.5 V) for an iron-based phosphate cathode. In this pyrophosphate material the anti-site defect in which the Li^+ and Fe^{2+} cations exchange positions is the intrinsic defect type found with the lowest energy. Lithium ion diffusion will follow non-linear, curved paths in the b-axis and c-axis directions, which show low migration energies. Hence, in contrast to 1D diffusion in $LiFePO_4$, fast Li^+ transport in $Li_2FeP_2O_7$ is predicted to be through a 2D network in the bc-plane, which is important for good rate capability and for the function of particles without nano-sizing. Favourable doping is found for Na^+ on the Li^+ site, and isovalent dopants (e.g., Mn^{2+}, Co^{2+}, Cu^{2+}) on the Fe^{2+} site; the latter could be used in attempts to increase the Fe^{2+}/Fe^{3+} redox potential towards 4V. Secondly, the relative abundance and low cost associated with Na-ion batteries now make them an attractive alternative for large-scale grid storage. Therefore, defect chemistry and ion migration results are presented for the sodium-based pyrophosphate framework, $Na_2MP_2O_7$ (where M = Fe, Mn). Formation energies for Na/M ion exchange are found to be higher than Li/Fe exchange, which has been related to the larger size of the Na ion compared to the Li ion. Low activation energies are found for long-range diffusion in all crystallographic directions in $Na_2MP_2O_7$ suggesting three-dimensional (3D) Na-diffusion. Thirdly, the search for high voltage cathodes for lithium-ion batteries has led to recent interest in the $Li_2Fe(SO_4)_2$ material which has a voltage of 3.83 V

vs lithium, the highest recorded for a fluorine-free iron-based compound. Ion conduction paths through the $Li_2M(SO_4)_2$ (M = Fe, Mn, Co) marinite family of cathode materials, show low activation energies for lithium migration along the a-axis channels giving rise to long-range 1D diffusion, supported by molecular dynamics (MD) simulations. Density functional theory (DFT) simulations were used to reproduce the observed high voltage of $Li_2Fe(SO_4)_2$ and to make predictions of the voltages of both $Li_2Mn(SO_4)_2$ and $Li_2Co(SO_4)_2$, and also examine local structural distortions on lithium extraction. Finally, the layered and tavorite polymorphs of $LiFeSO_4OH$ have recently attracted interest as sustainable cathode materials offering low temperature synthesis routes. Using DFT techniques the experimental voltage and structural parameters are accurately reproduced for the tavorite polymorph. An important result for the layered structure, is that similar accuracy in both cell voltage and structure can only be obtained if a van der Waals functional is included in the DFT methodology to account for the inter-layer binding.

Acknowledgments

Firstly, I would like to sincerely thank all members of the Saiful Islam group, both past and present, for the efforts they have made to assist me during my PhD, making it not only a productive but also a thoroughly enjoyable experience. I feel very fortunate to have been able to work with such a friendly and knowledgeable team (in no specific order my gratitude extends to Pooja Panchmatia, Chris Eames, David Tompsett, Paul Weaver, Grahame Gardiner, Jesse Dufton and Stephen Wood). Of these individuals I would especially like to highlight the efforts of Grahame for all the help and support he gave me when starting and Chris for his technical assistance and for introducing me to the weird and wonderful world of DFT.

I would also like to pay special thanks to Saiful for giving me the opportunity to complete my PhD in his group, in addition to the fantastic support, supervision and guidance he has provided me, which has been especially telling during the production of this thesis.

This work was funded by a studentship provided by the UK EPSRC Supergen consortium. Many calculations were only made possible thanks to the MCC providing access to the UK's high performance computing services, namely HECToR and ARCHER.

From the Parker group I would very much like to thank Steve Parker for his theoretical insight and kindness, in addition to all the postdocs and doctoral students from his group with which I have shared my time. Of whom, I would especially like to acknowledge Tom Shapley for his incredibly witty banter and assistance with Pauling, Jenny Crabtree for her help with LyX and Nick Williams for his unwavering friendship, philosophical discussions and not-so-witty banter.

Last, but definitely not least, I would like also like to express my appreciation to my immediate family (my mum Rose, my dad Paul and brother Tom) and close friends Jon Fraser, Dom Van der Waals, Jon Cherry, Jess Sharpe, Dave McClymont, Karen McClymont, Patricia Pérez Esteban and Ali Bradley. All of whom have played key roles in my development both from a personal (and occasionally) academic viewpoint. Thanks guys!

Finally, there is an almost endless list of people who I would, and indeed should, like to thank for their assistance and support during the completion of my PhD. So, if you're reading this and feel I haven't mentioned you directly, when I perhaps should of done, then I can only but apologise and attempt to reassure you that your omission was not intentional!

List of Publications and Presentations

Publications

1. Clark, J. M.; Nishimura, S.; Yamada, A.; Islam, M. S., High Voltage Pyrophosphate Cathode: Insights Into Local Structure and Lithium Diffusion Pathways, *Angewandte Chemie International Edition*, **2012**, *51*, 13149. [Appendix B] (Citations =10)

2. Clark, J. M.; Eames, C.; Reynaud, M.; Rousse, G.; Chotard, J.-N; Tarascon, J.-M.; Islam, M. S., High-Voltage Sulphate Cathodes $Li_2M(SO_4)_2$ (M = Fe, Mn, Co): Atomic-Scale Studies of Lithium Diffusion, Surfaces and Voltage Trends, *Journal of Materials Chemistry A*, **2014**, 2, 7446. [Appendix C]

3. Clark, J. M.; Eames, C.; Rousse, G.; Tarascon, J.-M.; Islam, M. S., Lithium Migration Pathways and van der Waals Effects in the $LiFeSO_4OH$ Battery Material, *Chemistry of Materials*, (dx.doi.org/10.1021/cm5008203). [Appendix D]

4. Clark, J. M.; Barpanda, P.; Yamada, A.; Islam, M. S., Sodium-Ion Battery Cathodes $Na_2FeP_2O_7$ and $Na_2MnP_2O_7$: Diffusion Behaviour for High Rate Performance, *Journal of Materials Chemistry A*, (in press). [Appendix E]

Oral Presentations

1. **December 2013,** RSC Annual Solid State Group Meeting, University of Bath. *"Atomic-Scale Insights into High Voltage Pyrophosphate Materials for Lithium and Sodium Batteries."*

2. **November 2013,** Molecular Graphics and Modelling Society (MGMS) Young Modellers' Forum, SOAS, University of London. *"Atomic-Scale Insights into New Iron-Phosphate Materials for Li Batteries."* (**Prize Winner**)

3. **May 2013,** Chemistry Departmental Postgraduate Symposium, University of Bath. *"New Polyanion Materials for Li Batteries: Insights at the Atomic Scale."*

4. **Sept 2012,** South West Computational Chemistry, University of Oxford. *"Atomic-Scale Insights into a New Pyrophosphate Li-ion Battery Material."*

5. **Feb 2012,** Chemistry Departmental Postgraduate Seminar, University of Bath. *"Computer Modelling Studies: Materials for Rechargeable Li-ion Batteries."*

6. **Feb 2011,** Supergen Energy Storage Consortium, University of Oxford. *"Modelling Studies of Materials for Rechargeable Li-ion Batteries."*

Poster Presentations

1. **June 2014,** International Meeting on Lithium Batteries (IMLB), Como, Italy. *"High Voltage Pyrophosphate Cathodes for Li- and Na-Ion Batteries: Atomic-Scale Insights into Defects and Diffusion."*

2. **June 2013,** Supergen Energy Storage Consortium, University of Oxford. *"Atomic-Scale Insights into the $Li_2FeP_2O_7$ Cathode Material."*

3. **April 2013,** Advances in Li-Battery Research, University of Huddersfield. *"Atomic-Scale Insights into the $Li_2FeP_2O_7$ Cathode Material."*

4. **March 2013,** International Battery Association (IBA) Meeting, Barcelona, Spain. *"Atomic-Scale Insights into the $Li_2FeP_2O_7$ Cathode Material."*

5. **Sept 2012,** CCP5 Annual Conference, University of Huddersfield. *"Atomic-Scale Insights into Phosphate-Based Lithium Battery Materials."*

6. **June 2012,** Transforming Materials Chemistry Meeting, University of St Andrews. *"Atomic-Scale Insights into Phosphate-Based Lithium Battery Materials."*

7. **Dec 2011,** RSC Annual Solid State Group Meeting, University of Liverpool. *"Atomic Insight into Mixed-Metal Phosphate Materials for Rechargeable Li-ion Batteries."* (**Prize Winner**)

8. **June 2011,** Lithium Battery Discussion (LiBD) Meeting, Arcachon , France. *"Anti-Site Defects and Clustering in Mixed-Metal $LiFe_{0.5}M_{0.5}PO_4$ (M = Mn, Ni, Co) Materials."*

9. **May 2011,** Chemistry Departmental Postgraduate Symposium, University of Bath. *"Atomic Insight into Mixed-Metal Phosphate Materials for Rechargeable Li-ion Batteries."* (**Prize Winner**)

Chapter 1

Introduction

1.1 Background: Energy Storage

The environmental threat posed by global warming, coupled with the increase in energy demand and a finite supply of fossil fuels, has intensified the challenge of developing alternative sources of energy that are both cleaner and sustainable [1, 2]. Unfortunately, at this time, there is still no single solution to this global problem [3–6].

Energy storage technologies appear to be one of the major clean energy options [7–15]. The overall performance of such technologies is entirely dependent upon the properties and characterisation of their component materials. Hence, in terms of research, the field of innovative materials chemistry has been at the heart of the advances made thus far, and will remain central to future progress [3, 5].

The rechargeable lithium ion battery, which has become an essential component for the information-rich, mobile society in which we live, is an excellent example of an energy storage technology that has been developed in order to meet consumer demands. Indeed, given that lithium batteries have far superior energy density in comparison to conventional batteries they have dominated the consumer electronics market in recent years. In order to put this into perspective one only needs to think of the vast amount of consumer electronic applications for which lithium batteries are used: mobile phones, digital audio players (e.g. iPods), laptop computers and power tools [5, 16].

However, the need to reduce carbon dioxide emissions from our roads is set to make the

electrification of road transport a necessity; a requirement that will involve the design of new hybrid or fully electric vehicles that incorporate low weight, safe and inexpensive batteries. Additionally, with a shift towards utilising natural renewable energy resources, which are inherently intermittent, energy storage technologies will also play a vital role in local and large scale grid energy storage. Therefore, it is likely that our future will see a requirement for different types of lithium (and sodium) batteries for a diverse range of applications. For portable electronic devices, low power and high capacity batteries; for hybrid electric vehicles (HEVs) and fully electric vehicles, high power and high capacity batteries; whilst for load levelling grid storage, inexpensive and high energy density batteries [5].

Despite the significant developments made with regard to batteries as an energy storage technology, it has become increasingly clear that in order to meet the demands of the diverse range of future applications it is of vital importance that a new generation of rechargeable batteries are made available. The main barrier to progress is a lack of suitable electrode materials and electrolytes, which can cause significant issues with regard to safety, cost and cycle life. Therefore, developing the next generation of lithium batteries will crucially require materials scientists and engineers to design novel electrode materials, which are both more efficient and sustainable [3, 5].

Often an understanding of the structural, defect and transport properties which underpin these complex lithium battery materials at the atomic-level is lacking. Through a combination of computer modelling and experimental techniques it is hoped that researchers within the field of materials chemistry will be able to improve the existing systems and develop newer, more efficient systems. This thesis details the study of several new promising cathode materials for both lithium-ion and sodium-ion batteries investigated by computational modelling techniques. The following sections of this chapter will provide an overview of the rechargeable battery concept (initially focusing on lithium batteries), their component materials, and the key cathode materials and objectives covered within this thesis.

1.2 Overview of Lithium-Ion Batteries

A battery contains a number of electrochemical cells, which act as a transducer by converting chemical energy into electrical energy and vice-versa. The cells are connected in series and/or

parallel in order to provide the desired voltage and capacity. Each cell contains two electrodes (anode and cathode) in addition to an electrolyte solution, which contains dissociated salts. The electrolyte has two functions: firstly, it acts to separate the positive and negative electrodes and secondly, it provides a medium through which the ions can transfer. An external connection between the anode and the cathode allows their chemical reactions to proceed in tandem. This process liberates electrons, which form the current that can be utilised for a specific purpose [16,17].

Whilst batteries are essentially simple in concept, the progress of their development has been relatively slow in comparison to other areas of electronics. As a result the battery is often considered as the heaviest, costliest and least 'environmentally friendly' component of any electronic device. The slow progress in battery development is rationalised by the lack of suitable materials for the electrodes and electrolytes, in addition to significant problems in understanding the different electrode/electrolyte interfaces [18].

1.2.1 From Primary to Secondary Cells

Lithium is both the most electropositive metal (with a redox potential of -3.04 V versus the standard hydrogen electrode), and it is also the lightest metal (M_r = 6.94 g mol^{-1}) [16]. In addition, lithium has two other very significant features: it has a wide temperature range of operation and a low self-discharge rate [19]. The initial motivation to design a lithium based battery occurred upon recognition that lithium metal could provide access to such properties, and that the combination of these properties would fulfill the optimum design requirement for storage systems with high energy densities. The first demonstration of the benefits of using lithium metal in electrochemical cells occurred in the 1970's. Due to their high capacity and variable discharge rates the potential of the lithium (primary) cell was apparent immediately, and they were rapidly implemented as the power sources in many devices such as watches and calculators. At a similar time intercalation compounds were discovered. These 'intercalation compounds' described the many inorganic compounds that were found to allow for the reversible insertion and extraction of alkali metals such as lithium. Their discovery was a major step forward and changed the research focus towards the development, and production, of high-energy rechargeable (secondary) lithium based battery systems [16,17].

The first example of a rechargeable (secondary) lithium based battery was developed by Exxon who used TiS_2 as the cathode, which was regarded as the best intercalation compound available at the time, Li metal as the anode and lithium perchlorate in dioxolane as the electrolyte. Whilst TiS_2 enabled facile, reversible Li ion intercalation with minimal structural change the system was not considered to be a viable option due to the lithium anode posing a number of safety issues. Given that Li metal reacts in a violent manner with water, the cells had to be constructed in a dry atmosphere and built water tight, hence the production costs for the cell were increased. Further to this, it was also found that the constant stripping and re-plating of the lithium anode that occurred during each discharge-recharge cycle whilst the cell was in operation caused the formation of uneven (dendritic) Li growth at the anode. The branch-like dendrites would eventually span the electrolyte, bringing the anode and cathode into contact resulting in a short-circuit, which often led to hazardous explosions. A number of strategies were proposed in order to solve these problems, the most successful of which involved substituting the metallic lithium anode with a second insertion material. The replacement of the lithium metal anode with a second insertion material required the lithium to be present in its ionic, rather than metallic, state thus negating the problematic dendritic growth and making the cells safer [16,17]. The same concept of utilising intercalation compounds at both the cathode and the anode is still used by modern rechargeable lithium-ion batteries.

In order to function as an energy storage technology the rechargeable lithium ion battery is first charged by the application of an electrical potential to the system, which pushes the Li^+ cations up an energy gradient towards the anode. Once at the anode the Li^+ cations are intercalated within its crystalline lattice. When the anode and cathode are connected via an external circuit discharge occurs, during which the Li^+ cations release their built-up chemical energy as they leave the intercalation sites within the anode and move through the electrolyte to the cathode. At the same time as the Li^+ cations are migrating to the cathode, electrons also flow to the cathode via the external circuit creating an electric current that can be tapped into by the user for their specific purpose (Figure 1.1) [20,21]. The reactions occuring at the electrodes during discharge can be written according to equations 1.1 and 1.2.

$$\text{Anode}: \ \mathrm{Li}_x\mathrm{C}_6(\mathrm{s}) \rightarrow x\mathrm{Li}^+(\mathrm{soln}) + 6\mathrm{C}(\mathrm{s}) + x\mathrm{e}^- \tag{1.1}$$

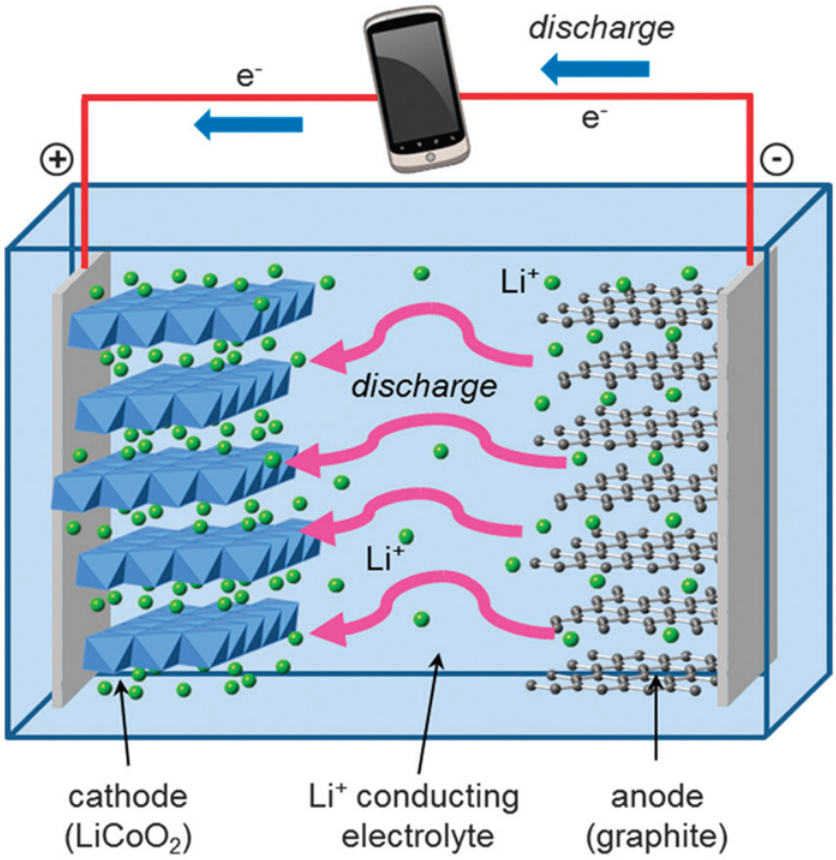

Figure 1.1: Schematic representation of a rechargeable Li-ion battery [20]. During charging, Li^+ ions flow to the negative electrode through the electrolyte and electrons flow from the external circuit. During discharge the directions are reversed, generating useful power for the electronic application.

$$\text{Cathode}: \ \text{Li}_{1-x}\text{CoO}_2(\text{s}) + x\text{Li}^+(\text{soln}) + x\text{e}^- \rightarrow \text{LiCoO}_2(\text{s}) \tag{1.2}$$

In 1990, Sony released the first rechargeable lithium ion battery onto the worldwide market. This battery, known as the Sony cell, has long since been deemed to be the first commercially successful example of a rechargeable lithium ion battery. The Sony cell is now considered to be the forerunner to subsequent examples of rechargeable lithium batteries and as such, it can be thought of as being the initial seed in the attempts to develop significantly improved sources of mobile electrical power [22]. Since the initial release of the Sony cell, there has been a consequent increase in demand for rechargeable batteries with higher energy densities for use in portable electronic devices that require higher power capabilities. With the enhanced

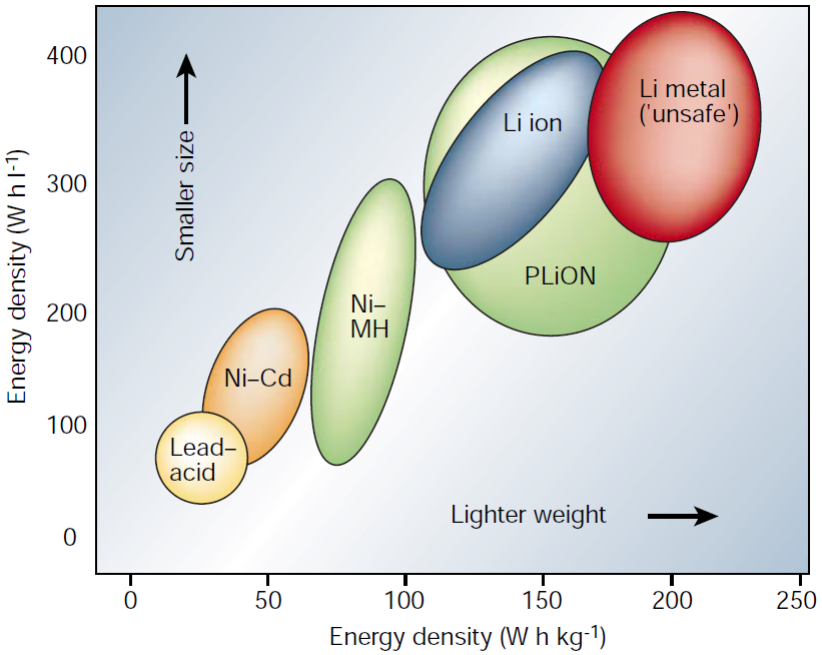

Figure 1.2: Graph displaying the volumetric and gravimetric energy densities for the current commercially available battery technologies, which clearly shows the increased energy density of the lithium ion in comparison to the other available systems [16].

requirements in terms of energy density, it comes as no surprise that rechargeable lithium ion batteries have been viewed as the battery technology of choice. Lithium batteries have all but monopolised the consumer market place, since they offer not only a high energy density, but also a flexible and lightweight design in addition to a longer lifespan than other comparable battery technologies, such as the nickel metal hydride and toxic nickel cadmium systems [16, 23]. From Figure 1.2 it is clear that lithium ion batteries have the highest energy density of any of the current commercially available battery technologies. Due to the enhanced energy density of the lithium ion the majority of the research carried out on rechargeable batteries has been, and will continue to be, centred upon lithium ion technology [21].

Despite the development of the rechargeable Li-ion battery, and the remarkable commercial success of the Sony cell in powering the portable electronics revolution, there are still significant improvements that will be required for this energy storage technology to continue sustainably into the future. It is important that measures are taken in order to reduce the cost of this technology, particularly with regard to large scale applications, by utilising cheaper more abundant materials, whilst maintaining the reliability and safety performance of the Li-ion

batteries currently deployed within portable electronic devices.

1.2.2 Component Materials

The remainder of this chapter will discuss the historical developments of the lithium ion battery components, before focusing on the current cathode materials used and considered for implementation within both lithium-ion and sodium-ion batteries. Following on from this, discussion will focus upon other examples of Li-ion battery technology currently attracting significant research interest. However, given that the focus of the research presented in this thesis is centred upon novel positive electrode materials for implementation within commercially available Li-ion and Na-ion cells, this area will be covered in much greater detail.

(i) Electrolyte

The electrolyte is required to facilitate Li-ion transport between the anode and cathode through the thin porous material that separates them. Therefore, to enable facile lithium diffusion the electrolyte must be an excellent ionic conductor. However, it is also required to be an electronic insulator to prevent a short circuit of the cell.

The electrolyte typically consists of a lithium salt, such as $LiPF_6$, dissolved in an organic solvent, such as ethylene/diethylene carbonate. For each battery, the choice of electrolyte composition is vital. The criteria on which this choice is based differs for batteries that are polymer-based and liquid-based. In lithium batteries the electrolyte components need to be able to function outside their window of thermodynamic stability (3.5 V), which is necessary since the highly oxidising cathode materials can have potentials that exceed 4 V. As a result of this, the initial research discounted the very positive cathode materials. Fortunately, it has since been recognised that the control of the electrolyte stability is kinetic in origin; hence non-aqueous electrolytes can now be utilised for potentials up to, and including, 5.5 V [16,24]. However, whilst the decomposition of electrolytes is slow, it will still occur on a continuous basis leading to a gradual decline in the performance of the cell over time. In an ideal world the available electrolytes would have significantly higher thermodynamic stability, and therefore degradation would not occur even in cells with very high voltages.

In order to meet the performance demands associated with electric vehicles and other large

scale applications, such as load-leveling equipment, it will be necessary to scale-up the lithium ion battery design that has been so successful within portable electronic devices. A requirement of such scale-up would be to store much larger volumes of electrolyte, and as a consequence greater amounts of the volatile solvents, within each cell. Hence, the likely increase in the size of the battery pack has led to significant concerns with regard to safety. The majority of this concern centres on the high vapor pressure and liquid state of the solution based electrolytes giving rise to potential fire hazards. The likelihood of such a threat becoming a reality is heightened when the lithium battery is subjected to conditions of an abusive nature. Due to these concerns, research in this area has focused on the development of liquid-free electrolytes based on the principle benefit that the liquid-free electrolytes will allow for greater packing flexibility, thus removing the safety issues. In addition to removing the very real safety concerns, the development of liquid-free electrolytes can provide other benefits in terms of volume, weight and cost [25]. However, unfortunately such liquid-free electrolytes have only been found to operate efficiently at temperatures of $\sim$80 ^{o}C. At lower temperatures the liquid-free electrolytes offer poor ionic conduction [16, 26].

With the apparent drawbacks to both the conventional liquid and polymer type electrolytes many researchers have shifted their attention into developing 'hybrid' gel polymer electrolytes (GPEs). The rationale for the development of these gel electrolytes centres on the theory of utilising the reliability and flexibility offered by polymer electrolytes, in addition to the enhanced performance capabilities that liquid electrolytes can provide. The concept of the GPE is relatively straightforward; by immobilising a large amount of liquid electrolyte (60-95%) within a polymer host, it is thought that the GPE will offer higher ionic conductivities than conventional polymer type electrolytes. Therefore in theory, the GPE should have the beneficial properties of maintaining the mechanical strength of a polymer type electrolyte in addition to an improved ionic conductivity [16, 27].

(ii) Electrodes

Whilst it is very important to find cheap sustainable materials, a significant amount of the primary research effort is focused upon improving the energy density of the lithium batteries. There are considered to be two main options for improving the overall energy density of a lithium battery; increasing the capacity of the electrode materials per unit volume (or

weight), or increasing the potential difference between the electrodes. Figure 1.3 shows a plot displaying capacity (A h kg^{-1}) versus potential difference against Li/Li^+(V) for various electrode (both anode and cathode) materials currently in use or of interest. In the ideal situation the cathode would be situated at the top right of the plot, with the anode located at the bottom right, thus ensuring both electrodes have a high capacity in addition to the prerequisite large potential difference. Currently an important limiting factor is the relatively low thermodynamic stability of the electrolyte; therefore maximising the potential difference between the electrodes can cause a reduction in the cycling performance of the cell. In the future it is hoped that improvements will be made to the electrolyte, which will enable pairs of cathodes and anodes to be chosen that will provide large voltages without causing a loss of performance.

(iii) Anode

An ideal anode material will have a low potential vs Li/Li^+ and will allow for highly reversible intercalation of Li ions during the continuous discharge-recharge cycles. As described previously, lithium metal was incorporated in the first early cells as the anode material. Being not only the lightest, but also the most electropositive metal, initially the use of a lithium anode appeared obvious [16]. However, its reactivity and the problems involved with plating and striping it with high efficiency gave rise to uneven (dendritic) Li growth during each successive discharge-recharge cycle as the metal was re-plated. Subsequently it was found that these dendrites were able to penetrate the electrolyte solution, causing the cell to short, leading to widespread concern with regard to the performance of the anode design and more importantly its safety [16, 22, 23]. It should be noted that, since Li metal offers a higher capacity than any of its possible replacements (see Figure 1.3), there is still a significant amount of ongoing research looking at rechargeable battery cells using Li metal anodes [18]. The most successful approach used to solve the problems associated with the Li metal anode involved replacing it with an intercalation material. However, it took nearly 10 years to find a suitable intercalation material to act as the anode therefore hindering the development of the Li-ion cell.

After the worldwide commercial success of the Sony cell subsequent rechargeable lithium ion batteries have, almost always, deployed carbonaceous materials to act as the anode component. This is due to the ability of graphite to reversibly intercalate lithium between the layers

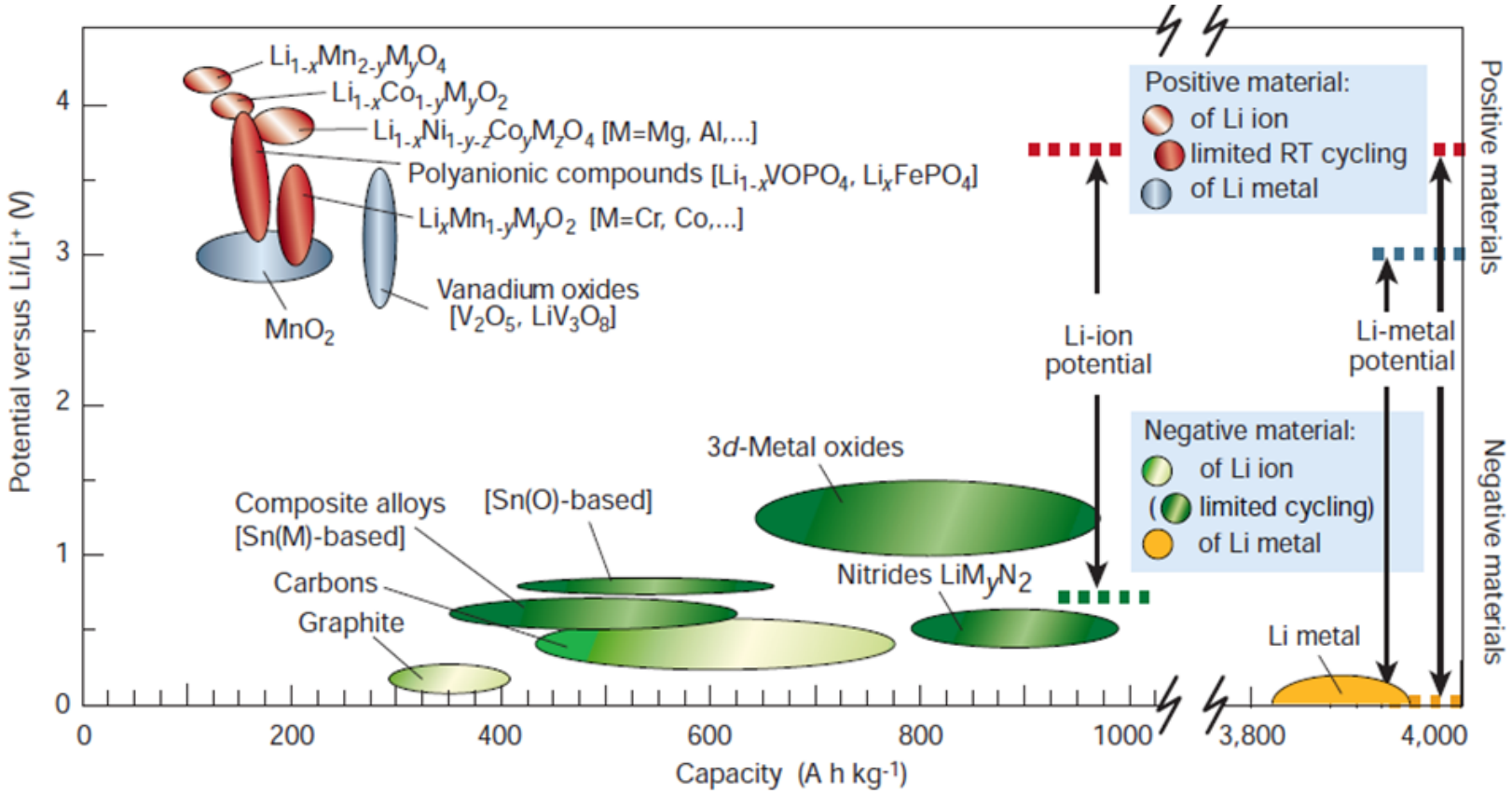

Figure 1.3: Plot of voltage vs capacity for anode and cathode materials, either in current use or under development [16].

of carbon within its structure [16, 23]. The lithium graphite intercalation compounds (LiC_6) are examples of such carbonaceous materials that are used at the anode, since they combine the beneficial properties of pure lithium without the formation of lithium dendrites [19]. LiC_6 has a considerably reduced storage capacity in comparison to pure lithium (340 mA h g^{-1} and 3800 mA h g^{-1} respectively) which is a significant drawback [23]. However, in addition to enabling Li-ion intercalation, graphite does have many advantages; with carbon being both cheap and readily available, further to which it also offers excellent electronic conduction properties. Despite these favourable properties, research attention has focused on developing anodes with higher capacities [28–33].

Research into the use of transition metal nitrides as potential anode materials initially provided promising results, with the cobalt member offering a large, stable and reversible capacity of 600 mA h g^{-1}, significantly larger than that offered by graphite. Unfortunately, the electrochemical performance of the other transition metal nitrides was found to be inferior to that of the cobalt member. Therefore, given the cost and toxicity issues associated with cobalt this particular avenue of anode research was not taken any further.

Using a variety of metallic and semi-metallic elements such as Bi, Pb, Sn and Cd, attempts were made to create various Li based alloys, however it was found that cycling these materials resulted in substantial volume changes (in some cases $\geq 200\%$) leading to the materials disintegrating. Further to this, a series of metal oxides, which showed large capacities (double that of graphite), were also investigated. However, the large volume changes which occurred during their first charge cycle resulted in large irreversible capacity loss and poor long term cyclability, which initially prevented these materials from being considered as viable alternative anodes [16, 31].

Since the turn of the millennium there have been significant advances in nano-science, with nano-structured materials found to give rise to a reduction in lithium ion diffusion distances in addition to providing greater structural flexibility. These findings have prompted a renewed interest in some of the anode materials previously dismissed, with researchers revisiting both metal oxides and the Li-alloys as potential anodes. The nano-structured anode materials were found to overcome problems such as poor electrochemical performance and large volume changes [31].

Considerable research attention has been given to nano-structured anatase (TiO_2) [34], in

part due to its low voltage, but also because of the superior lithium diffusion kinetics it offers when compared to other titanate polymorphs such as TiO_2-B and rutile [31]. Anatase also offers enhanced stability properties, due to the ease with which it can modify its nano-scale structure, which in turn allows for a longer cycle life than comparable materials. Unfortunately, as with other TiO_2 based anodes, anatase suffers from the the major drawback of having a lower capacity than other comparative technologies. Of these other anode technologies SnO_2 offers a particularly favourable theoretical capacity of 993 mA h g^{-1}, which is more than double the capacity of graphite. However, for SnO_2 to be truly considered as a potential anode material, there will be a requirement to improve its cycling stability; nano-sizing is a potential strategy that could have the desired effect [31,32].

Both of these oxide-based anode materials (TiO_2 and SnO_2) would currently offer lower overall cell voltages for a given cathode material than graphite due to their higher discharge potentials. Whilst this would allow for greater electrolyte stability and improved safety, it would ultimately lead to a reduced energy density. Therefore, in order to improve the energy densities of these oxide-based anode materials it would be necessary to connect them in a cell with a higher voltage cathode material. [32]

Further to these oxide-based anode materials, nano-structured silicon has also been widely championed as a potential anode material [28,30,33]. Theoretically the use of nano-structured silicon as a replacement anode for graphite could potentially enable a magnitude higher capacity to be attained in addition to providing comparable cell voltages to current materials.

(iv) Cathode

The cathode material is considered to be the current bottleneck to battery development. This is due to the fact that the current range of cathode materials typically offer much lower capacities than the corresponding anodes. From Figure 1.3, it is apparent that all of the cathode materials are located towards the left hand side of the plot with associated low capacities. It is for this reason that my research has focused on this area of the rechargeable lithium-ion battery, since novel positive electrode materials provide the greatest opportunity for improved battery efficiency.

The aim of research targeting the cathode has to be to find novel materials which can uptake greater amounts of active mass into smaller volumes, whilst at the same time maintaining

the overall safety and performance characteristics required. Figure 1.4 shows a time-line summarising cathode development. The text that follows will provide a detailed insight into the historical developments of the cathode materials summarised, after which there will be a section introducing a selection of the promising new cathode materials currently being developed.

In the quest to develop a fully functioning rechargeable (secondary) lithium battery the first intercalation materials investigated as potential cathodes were a series of dichalcogenides [35]. During the 1970's the dichalcogenides were found to offer good electrochemical performance. However, of the series investigated it was deemed that $LiTiS_2$ was the most appealing material for implementation as the cathode. There were several reasons for the choice of $LiTiS_2$ as the intercalation host. Firstly, it could potentially offer the highest capacity (increased energy density) as it was the lightest material. Secondly, there would be no requirement for a conductive coating as it showed semi-metallic behaviour and thirdly, lithium could be intercalated/de-intercalated in a highly reversible manner since no phase changes were observed during cycling [17]. In contrast to this last point, more recent materials have been shown to offer two-phase intercalation behaviour, which has given rise to limited de-intercalation (extraction) of lithium from the cathode host [36]. Whilst the heavier dichalcogenides exhibited properties that would be favourable for cathode materials, the research focus shifted towards the lighter oxides in the hope of finding suitable materials with increased energy densities [16].

Following the shift of focus from TiS_2, and the other dichalcogenides, the layered oxides of molybdenum (MoO_3) and vanadium (V_2O_5) were heavily investigated as intercalation hosts. However, of these layered oxides, interest in MoO_3 was fleeting due to its reduced reactivity with lithium. In comparison, V_2O_5 was found to react favourably with lithium with the intercalation of up to three Li ions per V_2O_5 formula unit. Unfortunately, it was discovered that the V_2O_5 formula unit underwent permanent structural changes when the Li intercalation was increased beyond unity. Whilst this structural change allowed V_2O_5 to reversibly intercalate 3 Li ions this material was found to rapidly lose capacity, when employed as the cathode, during the continuous charge/re-charge cycles [17].

Following on from this, the 1980's saw research focus move towards layered oxide materials. For these layered oxide materials significant variation was found with regard to the stacking of the MO_2 layers, which in turn was shown to be related to the Li content. Therefore, the intercalation/de-intercaltion of lithium gave rise to structural changes. Hence, as a result of

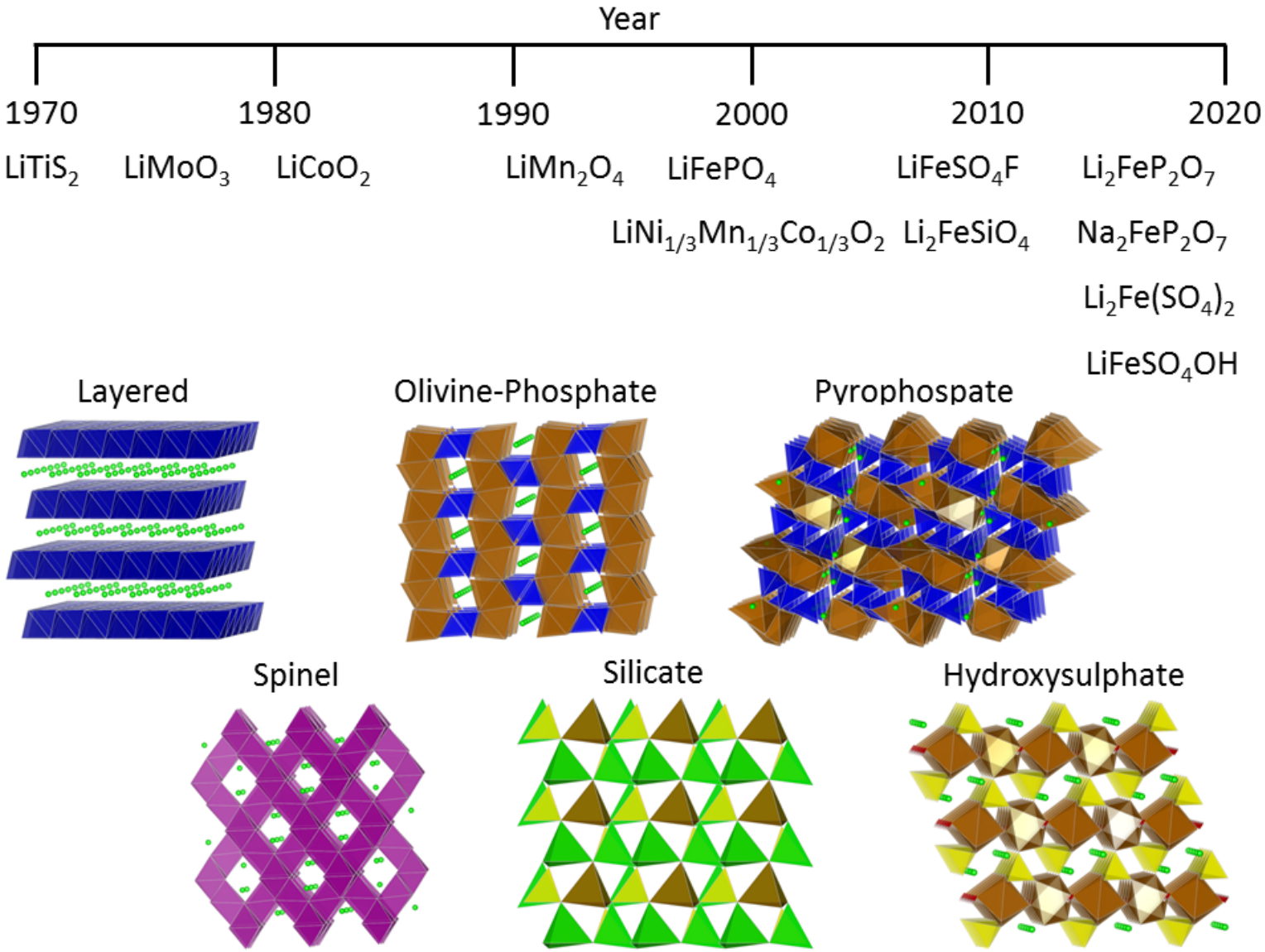

Figure 1.4: Time-line summarising cathode development and main structure types.

the inherent structural changes that occurred upon cycling, the electrochemical performance of the layered oxide materials was reduced. Despite the aforementioned problems with the layered $LiCoO_2$, which was first investigated as a potential positive electrode material by Goodenough in 1980, it showed excellent performance characteristics as a cathode. [17]

In 1990 Sony released the world's first commercial rechargeable lithium ion battery, known as the Sony cell, it combined a $LiCoO_2$ cathode with a graphite anode. With the Li ions shuttling between the cathode and anode during cycling the cell coined the "rocking chair" moniker. With the Sony Cell built in the discharged state the source of lithium ions was provided by the $LiCoO_2$. In terms of electrochemical properties the Sony cell offers a potential of $\sim$4 V with a moderate capacity of 130 mA h g^{-1}. This value, which is only half the theoretical capacity of $LiCoO_2$, is due to the structural changes that occur upon cycling as alluded to previously. Indeed, when the $LiCoO_2$ cathode is exposed to delithiation greater than 50% (i.e., Li_xCoO_2 for $x \leq 0.5$) the resulting phase changes give rise to reduced reaction rates and a consequential loss of capacity [17]. When the $LiCoO_2$ cathode is exposed to low lithium concentration (i.e. a state of high charge) the consequent high concentration of Co^{4+} raises safety concerns. This is because Co^{4+} is a highly oxidising species and, in order to revert to the more stable Co^{3+}state, it can cause oxidation of the electrolyte. The combination of the heat generated by such a reaction and the volatile nature of the electrolyte presents a very real risk of a fire or explosion. At best this scenario will lead to the cell losing capacity [22].

The worldwide supply of cobalt is limited, because of its low natural abundance, therefore its use and that of the $LiCoO_2$ cathode is limited to small scale (portable electronic) applications. Additionally due to the toxic nature of cobalt, it is environmentally hazardous. Hence, materials designed from cheaper, more abundant and less toxic elements will be needed in order to meet the sustainable power demands of electric vehicles [16, 17]. The combination of these reasons makes a compelling argument to continue the search for viable alternative cathode materials.

1.3 Current Cathode Materials

Since the inception of modern rechargeable lithium ion batteries there have been three main cathode materials which have dominated within the production of commercial lithium cells.

These are specifically: the LiMO$_2$ layered oxides, the LiMn$_2$O$_4$ spinel and the LiFePO$_4$ olivine phosphate, and each are reviewed in the following sections.

1.3.1 LiMO$_2$ Layered Oxides

LiMO$_2$ is the general form taken by layered structures (where M = V, Cr, Mn, Fe, Co, Ni). Within the LiMO$_2$ structure a cubic close packed arrangement is adopted by the oxide ions, with the M^{3+} ions occupying the edge-sharing octahedral sites that are present between the layers of adjacent oxide ions. The M^{3+} ions are only found to occupy edge-sharing octahedral sites in alternate layers with the Li^+ ions occupying the equivalent sites within the remaining layers [22], as shown in Figure 1.5.

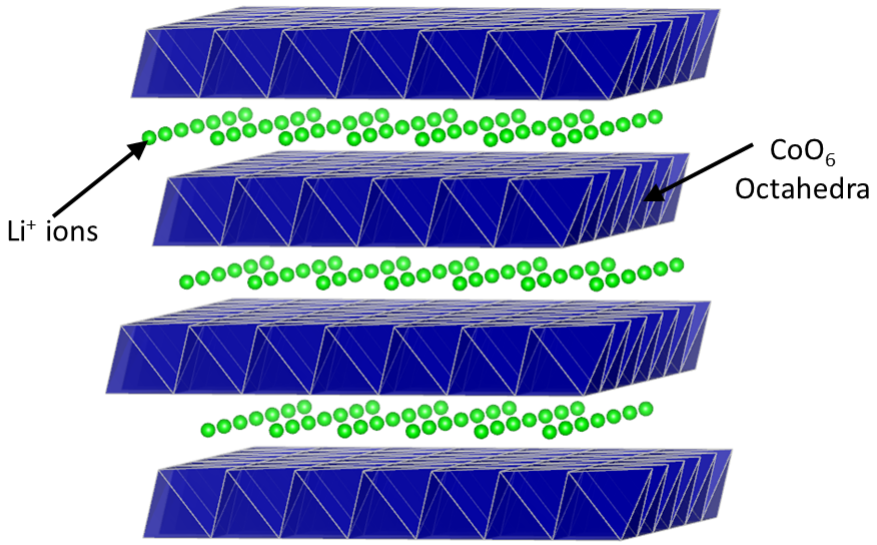

Figure 1.5: Layered structure of LiCoO$_2$ which consists of lithium ions that reside in edge-sharing LiO$_6$ octahedra between layers of edge-sharing cobalt oxide (CoO$_6$) octahedral sheets [17].

The LiMO$_2$ materials have been shown to have a slightly distorted α-NaFeO$_2$ structure possessing trigonal symmetry and assigned to the $R\bar{3}m$ space group. The layered structure of the LiMO$_2$ materials allows for two dimensional lithium diffusion within the layers of LiO$_6$ octahedra [22]. Within the LiMO$_2$ family of cathode materials most research attention has been focused on LiCoO$_2$, however compounds containing the other transition metals have been studied.

As nickel is both cheaper and more readily available than cobalt, $LiNiO_2$ has been considered as an alternative cathode material not least because of the potential of assembling a cheaper cell, but also one that in principle would offer higher capacities [22]. However, despite these apparent beneficial properties $LiNiO_2$ has not been implemented as a cathode material within a lithium battery cell in its pure state [17]. There are many reasons for this; firstly numerous reports suggest that preparation of stoichiometric $LiNiO_2$ is not possible. Instead the compounds produced have been found to have a $Li_{1-\delta}Ni_{1+\delta}O_2$ formula. The non-stoichiometry of the lithium nickel oxide material leads to a deficiency of lithium ions in addition to the presence of surplus Ni^{2+} ions within the lithium layers. These additional Ni^{2+} ions effectively act so as to pin the layers of oxide ions together, therefore the diffusivity of the lithium ions and consequently the electrochemical performance of the cell is reduced [17, 22]. The use of $LiNiO_2$ also raises similar safety concerns as described previously for $LiCoO_2$; with structural changes observed upon cycling and Ni^{4+} ions also highly oxidising, especially when present in the significant concentrations associated with a state of high charge.

In an attempt to overcome the various issues affecting the $LiNiO_2$ cathode a range of solid solutions have been investigated. From such studies it has been found that susbstituting cobalt for $\sim$30% of the nickel has maintained the site ordering within the structure, preventing the movement of Ni^{2+} ions into the lithium layers [17, 22]. Further to this, by introducing small amounts of aluminum or magnesium, which are redox inactive species, complete delithiation of the material is avoided which provides a stabilising effect when in a state of high charge [17,22].

The $LiFeO_2$ material would be an ideal alternative to both $LiCoO_2$ and $LiNiO_2$ in terms of prioritising reduced toxicity levels in addition to using a cheap and abundant element. However, $LiFeO_2$ is not considered for commercial application due to its low operating voltage. Due to the enhanced stability of Mn^{4+} ions with respect to Co^{4+} ions, the $LiMnO_2$ material has also been considered to be an attractive alternative to $LiCoO_2$ since the stable Mn^{4+} ions would allow the full capacity to be utilised [22]. Unfortunately, $LiMnO_2$ does not form a stable layered structure, instead upon cycling it is found to revert to the more stable spinel phase [17, 22] (see section 1.3.2).

Within the layered framework researchers have extensively studied solid solutions of Ni, Mn and Co, investigating stoichiometries such as $LiNi_{0.4}Mn_{0.4}Co_{0.2}O_2$ and $LiNi_{1/3}Mn_{1/3}Co_{1/3}O_2$ (known as NMC). Within these solid solutions Ni is used as the electrochemically redox active

species, Mn provides improved structural stability, whilst Co prevents further movement of Ni into the Li layers in addition to providing a further electrochemically active species at low lithium content. However, within the lithium layer low concentrations of Ni are required in order to avoid the occurrence of structural changes during delithiation. With such phase changes reducing the performance of the cathode the Co content of these solid solutions is carefully tuned. It should be noted however that the optimum solid solution composition is yet to be determined, with all variants displaying low electrical conductivity [17].

1.3.2 $LiMn_2O_4$ Spinel

In searching for an alternative cathode material to replace layered $LiCoO_2$, initially lithium manganese oxide appeared a reasonably viable replacement, particularly with its many beneficial properties compared to $LiCoO_2$. In comparison to $LiCoO_2$ lithium manganese oxides not only cost significantly less, but they also have much lower toxicity and are inherently safer. The fact that lithium manganese oxides are safer than $LiCoO_2$ is of particular importance to the development of lithium ion batteries of increased size for applications that require high power, such as HEVs [22,37]. Unlike nickel and cobalt that both form stable $LiMO_2$ layered structures, manganese does not form a stable phase with the α-$NaFeO_2$ layered structure. Instead it forms a spinel structure with a stable phase composition of $Li_{0.5}MnO_2$. Goodenough et al [38] were responsible for the original proposal of the $LiMn_2O_4$ spinel cathode structure (Figure 1.6), which has been found to be adopted by many other compounds of the form LiM_2O_4 (where M = Co, Ni, Ga) [17].

The structure of the $LiMn_2O_4$ spinel material is very similar to the α-$NaFeO_2$ layered structure of $LiCoO_2$, in that it is based on an arrangement of cubic close packed oxide ions. The major difference between the spinel and the layered structure is the way in which the cations are distributed in the available tetrahedral and octahedral sites [17]. Within the cubic close packed oxide array of the spinel structure ($Fd\bar{3}m$ space group) one-eighth of the tetrahedral sites are occupied by Li^+ ions, whilst Mn^{2+} ions occupy half of the available octahedral sites. In comparison to the layered oxide cathode materials which are two-dimensional hosts, the spinel cathode acts as a three-dimensional host material with intersecting tunnels that allow for rapid Li^+ ion diffusion. Another benefit of the spinel structure, not possessed by the

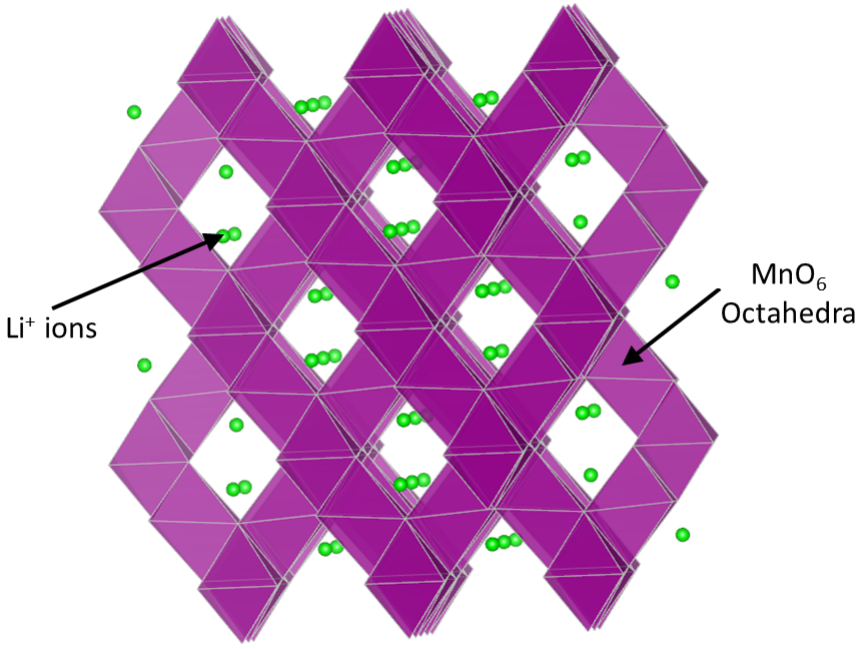

Figure 1.6: Spinel oxide structure of $LiMn_2O_4$ which consists of LiO_4 tetrahedra and MnO_6 octahedra within a three dimensional network.

comparative layered structures, is their enhanced structural rigidity, which enables the spinel to have increased selectivity of Li^+ ions over larger cations or solvent molecules [22]. First reported in 1983, by 1996 Nipon Moli had implemented $LiMn_2O_4$ within the first commercial lithium battery cell not containing a $LiCoO_2$ cathode. The primary motivations for the change of cathode was the environmentally benign nature of manganese in addition to its greater abundance and reduced cost compared to cobalt (manganese costs ~1% of the cost of cobalt).

The spinel framework allows for the intercalation of lithium up until the maximum composition of $Li_2Mn_2O_4$ is reached. Within $Li_xMn_2O_4$ the intercalation of lithium is found to occur at two different potentials, when $0 < x < 1$ lithium is inserted into the tetrahedral sites at a potential of 4 V, whilst for $1 < x < 2$ lithium is inserted into the octahedral sites at a potential of 3 V. In both cases the intercalation is associated with the Mn^{3+}/Mn^{4+} redox couple, hence the variation in the respective energies of the tetrahedral and octahedral sites is thought to account for the different potentials required to facilitate lithium insertion [22].

The major drawback of the spinel structure is the occurrence of phase changes upon lithium insertion, which is related to the increase in the concentration of Jahn-Teller active high spin Mn^{3+} species. These structural changes that take place during cycling can have pronounced

effects upon the volume of the material, with changes as large as 6%, causing contact to be lost between the particles of $Li_xMn_2O_4$. The storage capabilities of these isolated particles is reduced, therefore resulting in an overall loss of capacity for the cell. The formation of solid solutions by substituting small quantities of Mn with other metals (Li, Be, Mg, Cr, Co, Ni, Cu, Zn, Ga) has been used as a method to protect against such effects by enhancing the structural stability. Of these solid solutions a composition that is of significant interest for high power applications such as HEVs is that of $LiMn_{1.5}Ni_{0.5}O_4$ since it provides a high operating potential of 4.7 V, has a high rate capability and shows reasonable stability during cycling. However, gradual structural degradation during cycling has still been shown for this material. Such results have therefore motivated researchers to further improve the structural integrity of the spinel by replacing small amounts of Mn with Mg to form solid solutions with compositions such as $LiMg_{0.05}Mn_{1.5}Ni_{0.45}O_4$ [39]. The obvious downside to such measures is that the substitution of Mn with any species that is redox inactive will inevitably lead to a reduction in the capacity of the cell [22].

Much of the interest in the spinel structure has centred on its potential for use within a highly powered lithium ion battery for a HEV, but unfortunately it has been found that the capacity of the spinel falls to ~80 mA g^{-1} under high drain rates. Whilst the spinel is still considered for application within HEVs, the material has had additional problems involving self-discharge when it is left fully charged. This problem seems to be particularly apparent with increased temperatures. However, given that the root cause of this loss of capacity is thought to be brought about by the presence of the acidic HF, which is seemingly generated by the fluoride-containing $LiPF_6$ salt and trace amounts of moisture, a solution to this problem may be to change the salt to LiBOB [17].

1.3.3 LiMPO$_4$ Olivine Phosphates

In 1997 Goodenough et al [36] found that changing the traditional anions, such as oxides used within previous cathodes, and instead using polyanions, such as phosphates and sulphates enabled the Fe^{2+}/Fe^{3+} potential to be increased to a level that was commercially attractive (3.5 V). This finding was considered to be caused by a destabilisation of the Fe^{3+} state, which has become known as the inductive effect [40]. Further to which, by deploying abundant iron

as a full Fe^{2+}/Fe^{3+} one-electron redox system and by ensuring that all oxygen atoms are fixed via strong covalent P-O bonds, the potential pitfalls of expense and safety involved with the use of $LiFePO_4$ can be negotiated with little or no effect upon the energy density [41, 42].

LiMPO$_4$ has an olivine type structure, which crystallises in the *Pnma* space group (Figure 1.7). The olivine structure consists of a hcp array of oxygen, with lithium or M (M = Mn, Fe, Ni, Co) occupying half of the the octahedral holes and phosphorus occupying an eighth of the tetrahedral holes. This combination gives rise to layers of edge-sharing MO_6 octahedra linked with PO_4 tetrahedra, thus forming a one dimensional channel structure. Within these channels the Li^+ ions are found in chains of edge-sharing octahedra [43–45]. In general the olivine family of phosphates have been found to offer high voltages and good thermal stability.

In contrast to the multidimensional Li^+ diffusion within layered $LiCoO_2$ (2D) and spinel $LiMn_2O_4$ (3D) structures the channel structure of the olivine LiMPO$_4$ phosphates only allows for 1D Li^+ diffusion, and consequently it has a comparatively low rate of Li conduction. Fortunately, by manipulating the crystal morphology plate-like particles can be created for which the lithium channels are parallel to the short dimension, therefore reducing the distance required for Li diffusion, which improves the rate of Li conduction. However, defects and impurities can cause the 1D channels of the LiMPO$_4$ phosphates to become blocked, negatively effecting the Li diffusion characteristics and reducing the capacity of the cell. Anti-site defects, involving Fe ions and Li ions swapping sites, have been shown by both atomistic simulation [45] and experimental [46] investigations to be favourable in $LiFePO_4$. More recent studies indicate that whilst anti-site defects are intrinsic within the olivine LiMPO$_4$ phosphates, their distribution within the structures may be possible to control, hence limiting their effect upon the rate of Li conduction [47].

Since the work of Goodenough et al [36] most of the attention given to the LiMPO$_4$ olivine structured phosphates has centred on $LiFePO_4$. In summary, $LiFePO_4$ is viewed as a cathode material that offers substantial promise not only due to its large theoretical capacity ($\sim$170 mA h g^{-1}) and high operating voltage ($\sim$3.5 V vs. Li/Li^+) but also due to its relative low cost, environmentally benign nature and significant safety advantages [16,18,36,45]. Indeed, lithium battery cells based on the $LiFePO_4$ cathode have been commercialised by both A123 and Phostech, and have been implemented as the energy storage technology for various appliances, such as power tools and mobile phones. However interest remains in the other LiMPO$_4$

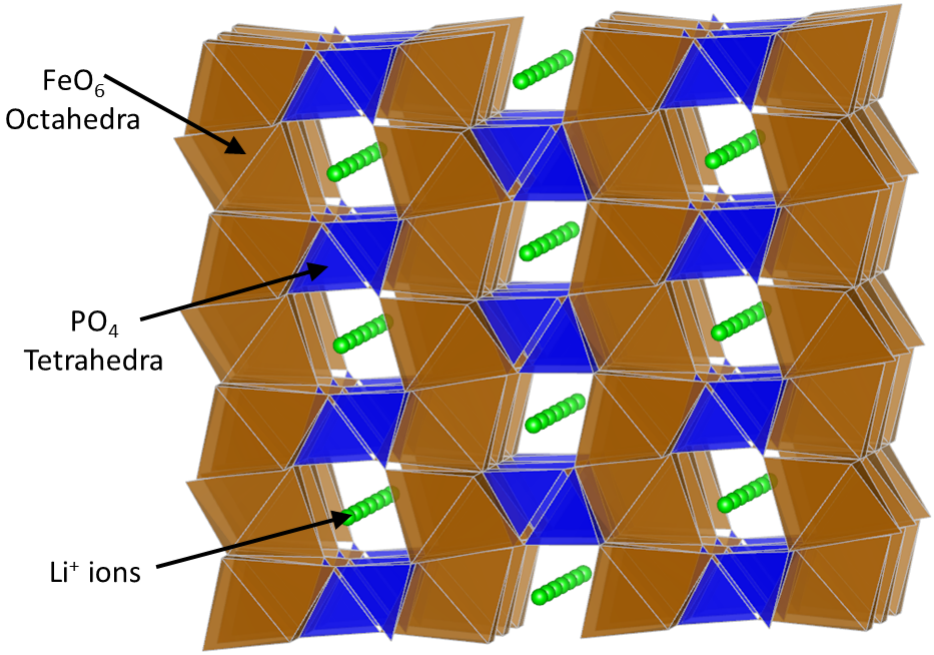

Figure 1.7: Olivine structure of $LiFePO_4$ [44].

olivine structured orthophosphate systems [48–52], particularly in light of the fact that each of these alternative systems would in theory allow for higher cell voltages to be obtained. Unfortunately, each of the alternative $LiMPO_4$ materials suffer from a number of problems that need to be overcome before they can be considered as viable replacements for $LiFePO_4$ [45].

The problem for the $LiCoPO_4$ and $LiNiPO_4$ materials is that, in order to make them useable, advances in the chemistry of the electrolyte will be required to enable their upper charge voltages to be accessed. Further problems experienced by $LiNiPO_4$ are that it displays very low charge/discharge capacity in addition to being a poor electronic conductor. For $LiMnPO_4$ the major failing of the material is that its lithium ion conductivity is inferior to that of $LiFePO_4$. However, the possibility of improved energy density over $LiFePO_4$ means that interest in the alternative $LiMPO_4$ systems is maintained. The major advantage for the alternative $LiMPO_4$ systems is that in principle each material will allow for cell voltages ($>$ 4 V) to be reached that are in excess of those currently obtained from $LiFePO_4$ [45,53].

In an attempt to find novel cathode materials based on the layered-oxide structure there have been investigations into mixed-metal materials such as $LiNi_{0.5}Mn_{0.5}O_2$ [54–56]. Similarly, mixed-metal materials have been investigated for the spinel type material, with studies having

been conducted on both $LiMnFeO_4$ [57] and $LiMnCoO_4$ [58]. Consequently, forming olivine-structured solid solutions of the type $LiM_{1-x}M'_xPO_4$ may provide a potential solution to the problems encountered by the $LiMPO_4$ end-member materials [45,59]. There have already been investigations into solid-solutions of mixed-metal phosphate materials such as $LiFe_{1-y}Mn_yPO_4$ and $LiFe_{0.5}Mn_{0.5}PO_4$ [36, 60, 61]. Padhi et al [36] demonstrated that the for $y < 0.45$ the $LiFe_{1-y}Mn_yO_4$ solid-solution would allow access to the Mn^{3+}/Mn^{2+} couple. It was also found that these mixed-metal phosphates investigated were isostructural with their end members ($LiMnPO_4$ and $LiFePO_4$), and as such they adopted the same olivine-type lattice structure [53].

Wolfenstine et al suggested that the potential of the Ni^{3+}/Ni^{2+} redox couple within $LiNiPO_4$ appears to lie between 5.1 and 5.3 V. Unfortunately this research also indicates that $LiNiPO_4$ has a low rate capability which comes as a consequence of the material showing very poor electrical conductivity and slow Li^+ ion diffusion [62].

A study of the $LiMnPO_4$ end-member by Liu et al [63] concluded that it had a very good overall reversible capacity of 140 mA h g^{-1}, which was obtained at room temperature and a high redox potential of 4.1 V vs. Li/Li^+. Additionally it was proposed that the $LiMnPO_4$ end-member showed excellent thermal stability. Unfortunately, in terms of ionic conductivity it has been shown that the electrochemical performance of $LiMnPO_4$ is lower than that of $LiFePO_4$ by approximately five orders of magnitude and that complete delithiation of $LiMnPO_4$ does not occur due to possible blocking of the Li^+ ion migration channels [64, 65].

The ability of $LiCoPO_4$ to reversibly intercalate Li^+ ions and then delithiate at the very high redox potential of 4.8 V vs. Li/Li^+ means that it is a material that can be considered for application within a high-voltage lithium ion battery [66]. Unfortunately, the inherent problems associated with cobalt in terms of its limited supply and expensive nature may make production of a pure $LiCoPO_4$ olivine type cathode material very costly.

In general, the $LiMPO_4$ olivine phosphates display low intrinsic electronic conductivity, with various methods considered as solutions to this problem, including: carbon coating; cation doping; and using synthetic strategies to reduce the particle size [17, 18, 43–45]. However, as of yet, a consistent level of improvement for the electronic conductivity has not been demonstrated.

Before introducing a range of materials that are currently in development, it would seem appropriate to summarise the key criteria which are necessary requirements for a high perfor-

mance cathode material:

- Designed from cheap, abundant materials that are environmentally benign.
- Excellent performance characteristic as an intercalation host, allowing facile lithium insertion and removal in tandem with excellent structural stability.
- High operating voltage (electrolyte stability currently limits this requirement).
- Large operating capacity.
- Favourable electronic conductivity, therefore removing the need for additional processing such as carbon coating.
- Rapid ionic conductivity, of particular importance for high power applications, such as HEVs, which need large instantaneous amounts of energy.

The current commercial batteries described previously do meet many of these requirements. However, as of yet no single cathode material has a strong showing for all the criteria outlined.

1.4 New Polyanion Cathode Materials and Project Objectives

This thesis examines several novel materials, which have shown promise as alternative cathode materials when compared to those currently commercially available. During the following sections each material (or family of materials) is introduced via a brief summary, with the corresponding objectives of our computer modelling investigation outlined.

1.4.1 $Li_2FeP_2O_7$ Pyrophosphate

Recently, it has been proposed that the pyrophosphate, $Li_2FeP_2O_7$ [67–69] and related compounds [70–73] may provide a new platform for important electrode research. The previously known composition $LiFeP_2O_7$, was found to have significant drawbacks which prevented it from being considered for cathode use [36, 74–76]. In comparison, $Li_2FeP_2O_7$ shows ease of synthesis via conventional solid-state reaction coupled with its high voltage of 3.5 V vs. Li/Li^+ without nano-sizing or carbon coating [67]. This voltage is the highest of the known Fe-based

phosphate cathodes. Although the capacity of $Li_2FeP_2O_7$ is limited to a one-electron theoretical value of ~110 mA h g^{-1}, the chemical composition $Li_{2-x}MP_2O_7$ allows for the possibility of a two-electron reaction where the theoretical capacity could reach 220 mA h g^{-1}.

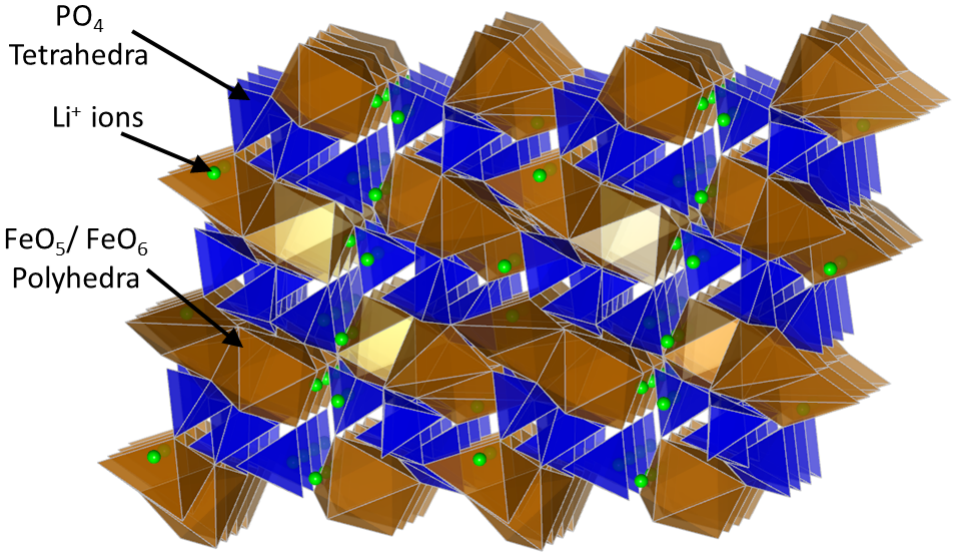

Figure 1.8: $Li_2FeP_2O_7$ structure.

The crystal structure of the pyrophosphate is complex and was investigated previously for a lithium deficient composition ($Li_{1.75}FeP_2O_7$) using synchrotron x-ray diffraction experiments [67]. This refinement showed that $Li_2FeP_2O_7$ is essentially isostructural (space group $P2_1/c$) with $Li_2MnP_2O_7$ [77] comprised of $[P_2O_7]^{4-}$ anions which are corner shared dimers of PO_4 tetrahedra. Each of the polyhedral units share their corners or edges to form a three-dimensional framework structure (Figure 1.8). The difference between the structures is the existence of significant static disordering among the Li and Fe sites. Li atoms occupy five crystallographic sites and form distorted LiO_4 tetrahedra or distorted LiO_5 trigonal-bi-pyramids. Fe atoms occupy three sites as FeO_6 octahedra or distorted FeO_5 trigonal-bi-pyramids. Two of the Li sites and two of the Fe sites are crystallographically identical giving rise to a structure with both Li and Fe mixed occupancies; these sites are labeled Li4/Fe2 and Li5/Fe3 and have occupancies of approximately $\frac{1}{3}$:$\frac{2}{3}$ and $\frac{2}{3}$:$\frac{1}{3}$ respectively.

To fully understand the factors influencing the electrochemical behaviour of the newly synthesised lithium iron pyrophosphate with composition $Li_2FeP_2O_7$ it is clear that fundamental knowledge of the underlying defect and transport properties is needed on the atomic scale. The

study, detailed in **Chapter 3**, uses advanced simulation techniques to investigate important issues related to point defects, dopants and lithium ion migration in the $Li_2FeP_2O_7$ material and in sodium-based pyrophosphates (described in the next section).

1.4.2 Sodium-Ion Batteries and $Na_2MP_2O_7$ Pyrophosphates

The portable energy storage market has been dominated by Li-ion batteries in the past two decades [4,6,18,43,78–80] due to their light-weight, high energy density and high power: which all depend critically on fast Li-ion mobility. Despite the widespread use of Li-ion cells, batteries based on alternative carrier ions such as sodium ions could be more suitable for large-scale grid storage systems. Whilst the higher gravimetric capacity afforded by Li-ion cells is critical for portable applications, the relative abundance and low cost associated with Na-ion batteries now make them an attractive alternative for large-scale grid storage. Where gravimetric energy density is not a concern, Na-ion batteries are a possible option. Moreover, the need for battery technology to meet the demands of such large-scale stationary energy storage is only likely to increase; particularly in view of the heightened interest shown towards renewable energy sources that provide intermittent power, for which load-levelling will be required [81,82].

Substantial effort has been expended in previous decades to prepare electrode materials that can easily intercalate and transport Na-ions at suitable potentials. Amongst the positive electrode materials, a variety of layered oxides; Na_xCO_2, $NaCrO_2$, $NaVO_2$, $Na_x[Fe_{0.5}Mn_{0.5}]O_2$ and polyanionic compounds; $NaFePO_4$, $Na_3V_2(PO_4)_3$, Na_2FePO_4F, $NaFeSO_4F$ have been reported [83–90]. Recent studies have suggested the Na^+ diffusion coefficient for certain Na-analogues of positive electrode materials can be as high, if not higher than the comparative Li^+ diffusion coefficient (perhaps due to less polarisation), particularly for layered oxides [91].

Often sodium and lithium compounds are not found to be isostructural. This is particularly evident for polyanion materials where the alkali size/charge ratio has a significant influence in determining the phase that is most thermodynamically stable. Consequently varying electrochemical properties are found and, amongst the various lithium and sodium positive electrode materials, intriguing differences have emerged [81,92].

An additional challenge faced by Na-ion batteries has been to find a suitable negative electrode material for low-potential insertion, since soft carbons such as the graphitic materials

used in Li-ion cells were found to be unsuitable [93, 94]. With much scope for porous carbon design, significant strides have been taken in this area; with materials involving novel forms of hard carbon, metal alloys and synthesised metal oxides investigated. From such studies the capabilities of sodium metal dioxides based on vanadium and titanium have been highlighted, particularly in view of their low voltage properties. Of these the $Na_2Ti_3O_7$ material [94–96] has been the focus of significant research interest. An advantage for the development of negative electrodes for Na-ion batteries is provided by the (generally) lower voltage of the Na compounds, meaning that enhanced overall operating voltages and therefore energy densities can be accessed. Inevitably the potential of the sodium containing positive electrode would also be lowered, however this presents an opportunity to probe materials for which the potential of the lithium analogues were beyond the stability range of the available electrolytes [81, 92].

From recent electrochemical studies, it has been found that Na-compounds that crystallise with either open or layered structures have been shown to be the most viable options for intercalation compounds. This finding has been linked with the observation that such structural frameworks are better able to accommodate the larger Na^+ ion sizes. Further, in terms of phase stability, open and layered structures have also been found to generally exhibit Na and Li versions of the same compound. However, the development of new structures specifically based on sodium (i.e., not from variations of lithium analogues) is likely to be of great importance to the advancement of the next generation of Na-ion batteries. Therefore, in order to develop materials with favourable intercalation properties, it may be necessary to design solid state structures capable of overcoming the large volume expansions/contractions caused by the removal/insertion of the large Na^+ ion. In conclusion, recent findings suggest that overall Na-ion batteries offer many favourable properties that could allow them to compete with their Li-ion counterparts, and this area of research is one that appears to provide much promise and opportunity [81, 92].

Motivated by the significance of Na-ion batteries for large-scale storage systems in addition to the promising properties of $Li_2FeP_2O_7$, attempts were made to synthesise a sodium version of the Fe-based pyrophosphate ($Na_2FeP_2O_7$). [97–99] Further to this attempts were made to synthesise other Na-analogues using different transition-metal active redox species such as a new polymorph of $Na_2MnP_2O_7$ (β-$Na_2MnP_2O_7$) [100, 101].

Yamada et al. [97] were able to prepare $Na_2FeP_2O_7$ via a conventional one-step solid-

state synthesis. With no further optimisation, the as-synthesised $Na_2FeP_2O_7$ cathode was found to be electrochemically active, delivering a reversible capacity of 82 mA h g^{-1} with an operating voltage around 3 V vs. Na/Na^+. With its theoretical capacity of ~100 mA h g^{-1} and good rate capability $Na_2FeP_2O_7$ is widely considered to be a highly promising novel cathode material. From a crystal structure view-point, the change of alkali ions from Li to Na results in different crystal frameworks: while $Li_2FeP_2O_7$ adopts the monoclinic ($P2_1/c$) structure [67], $Na_2FeP_2O_7$ adopts the triclinic ($P\bar{1}$) structure [98].

Recently β-$Na_2MnP_2O_7$ [100] has also been unveiled as a new potential pyrophosphate cathode material for a sodium-ion battery, and was found to offer similar (if not slightly superior) electrochemical performance to $Na_2FeP_2O_7$. The β-$Na_2MnP_2O_7$ polymorph was found to crystallise in the triclinic ($P1$) space group [100], isostructural to rose-polymorph of $Na_2CoP_2O_7$ [102]. β-$Na_2MnP_2O_7$ displays a discharge capacity close to 80 mA h g^{-1} (at 25 °C) with a voltage located at 3.6 V vs. Na/Na^+, the highest Mn^{3+}/Mn^{2+} redox potential amongst all Mn-based sodium cathodes. The electrochemical activity of this Mn-containing cathode material is remarkable, especially when compared to its Li counterpart ($Li_2MnP_2O_7$), which is almost inactive at room temperature owing to its sluggish kinetics [101]. Therefore, the room-temperature cycling of the as-synthesised micro-metric β-$Na_2MnP_2O_7$ comes as a surprise.

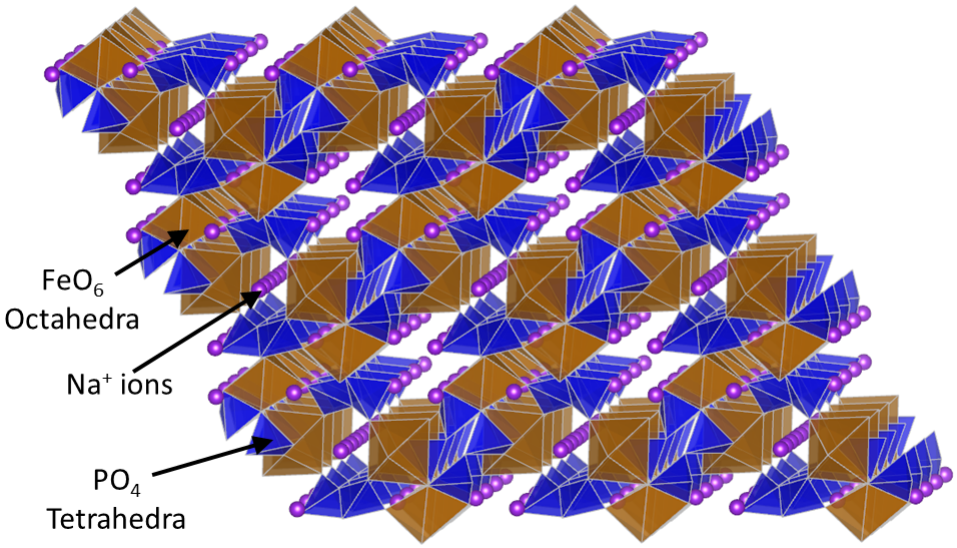

Figure 1.9: $Na_2FeP_2O_7$ structure.

The structure exhibited by $Na_2FeP_2O_7$ is triclinic ($P\bar{1}$) (Figure 1.9) [98]. Comprised of corner-sharing FeO_6 octahedra creating Fe_2O_{11} dimers, which are interconnected by both corner-sharing and edge-sharing with the P_2O_7 pyrophosphate groups. The FeO_6 octahedra and PO_4 tetrahedra are connected in a staggered fashion thus creating large tunnels along the [011] direction within which the Na atoms are present. The Na ions occupy six distinct crystallographic sites; three of which are fully occupied (Na1, Na2, Na3), whilst the other three adopt sites that are partially occupied (Na4, Na5, Na6).

The triclinic ($P1$) structure exhibited by β-$Na_2MnP_2O_7$ [100] consists of distorted MnO_6 octahedral and tetrahedral building blocks which are connected in a staggered manner thus creating tunnels along the [001] direction for potential Na^+ migration. The structures have corner-sharing isolated MnO_6-MnO_6 (Mn_2O_{11}) dimers, which are in turn connected by the P_2O_7 pyrophosphate units by a mixed edge and corner-sharing fashion. The constituent Na atoms are located in eight nonequivalent crystallographic sites. It has been postulated that the complex nature of this triclinic ($P1$) structure may allow for multidimensional Na^+ diffusion [97].

Our study, outlined in **Chapter 3**, provides a systematic examination of the intrinsic defect chemistry and Na-ion migration in $Na_2MP_2O_7$ (M = Fe, Mn) pyrophosphate cathodes in comparison with $Li_2FeP_2O_7$ by using atomistic modelling techniques for the first time.

1.4.3 $Li_2M(SO_4)_2$ Sulphates

The recently synthesised lithium iron sulphate, with composition $Li_2Fe(SO_4)_2$, was found to display a theoretical capacity of 102 mA h g^{-1} and a high potential of 3.83 V vs. Li/Li^+ for the Fe^{2+}/Fe^{3+} redox couple, which is the highest reported voltage for a fluorine-free iron-based compound [103]. There is also interest in both the previously reported $Li_2Co(SO_4)_2$ phase [103] and the recently synthesised $Li_2Mn(SO_4)_2$ phase [104].

The structures of the marinite $Li_2M(SO_4)_2$ (M = Fe, Mn, Co) sulphate compounds comprises isolated MO_6 octahedra linked through shared oxygen vertices with the surrounding SO_4 tetrahedra. Each octahedron is linked to six SO_4 tetrahedra which are orientated in a star or pinwheel pattern when viewed along the b-axis. Conversely, each SO_4 is only bound to three MO_6 octahedra and the fourth unshared corner of the SO_4 tetrahedron points into

an open channel where the lithium resides, as shown in Figure 1.10.

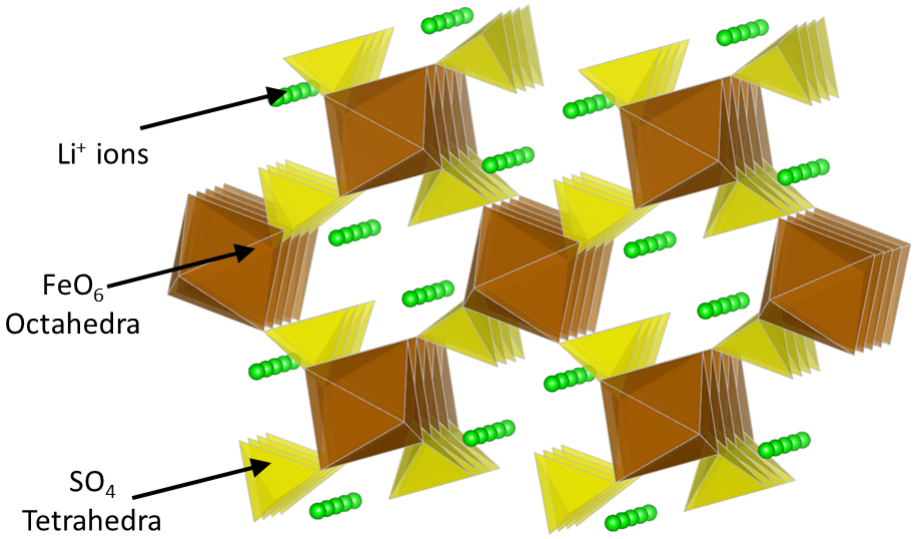

Figure 1.10: The $Li_2M(SO_4)_2$ (M = Fe, Mn, Co) structure.

Despite the isostructural nature of the three $Li_2M(SO_4)_2$ phases, only the Fe analogue is observed to be electrochemically active [103, 104]. Upon cycling, the $Li_2Fe(SO_4)_2$ material transforms to the delithiated phase $LiFe(SO_4)_2$ through a biphasic mechanism, as suggested by the plateau observed at 3.83 V vs. Li/Li^+ on the electrochemical curve and further confirmed by in-situ XRD measurements [103]. The delithiated phase $LiFe(SO_4)_2$ can also be obtained through chemical oxidation of $Li_2Fe(SO_4)_2$. It was found that the delithiated phase maintains the general 3D framework of $Li_2Fe(SO_4)_2$ [104], but the FeO_6 octahedra and SO_4 tetrahedra undergo slight rotations upon lithium removal. As a result, each octahedron is still linked to six SO_4 tetrahedra with the fourth unshared corner of the SO_4 tetrahedra pointing at the open channels where the lithium resides. However, in contrast to the lithiated phase, the lithium ions of the oxidised $LiFe(SO_4)_2$ were localized at the centre of the channels, in a half-occupied general position in the vicinity of the $(\frac{1}{2}\ 0\ \frac{1}{2})$ site [104].

The study, described in **Chapter 4**, uses combined atomistic modelling and density functional theory (DFT) techniques to investigate key issues related to the defect chemistry, lithium diffusion, surface structures and voltage trends within the $Li_2M(SO_4)_2$ (M = Fe, Mn, Co) family of electrode materials. It is hoped that such an investigation will provide useful insights into these significant sulphate systems and may subsequently provide a new platform for related

lithium battery electrode research.

1.4.4 $LiFeSO_4OH$ Hydroxysulphates

Recently, it has been proposed that the newly synthesised layered iron hydroxysulphate [105] ($P2_1/c$), with composition $LiFeSO_4OH$ and related compounds may provide a new platform for important positive electrode research. Direct synthesis of $LiFeSO_4OH$ was provided by Tarascon et al. [105] and results in the formation of a layered polymorph of the material. Electrochemical testing of the layered phase showed it to have a voltage of 3.6 V vs. Li/Li^+ for the Fe^{2+}/Fe^{3+} redox couple with a similar discharge capacity in the range 100-110 mA h g^{-1} observed upon cycling. The favourable properties of layered $LiFeSO_4OH$ suggest the possibility of commercial applications for this phase. In addition to the layered hydroxysulphate, tavorite $FeSO_4OH$ has previously been investigated by Reddy et al [106]. Recent work by Tarascon et al. [107] proposed this material to crystallise in the C2/c space group, into which Li could be inserted at a potential of 3.2 V vs. Li/Li^+ for the Fe^{2+}/Fe^{3+} redox couple with a stable discharge capacity of ~110 mA h g^{-1}. The resulting lithiated composition of Li_xFeSO_4OH ($P\bar{1}$, where $x < 1$) for this tavorite is therefore prepared by electrochemical insertion of Li into $FeSO_4OH$ and not by direct synthesis.

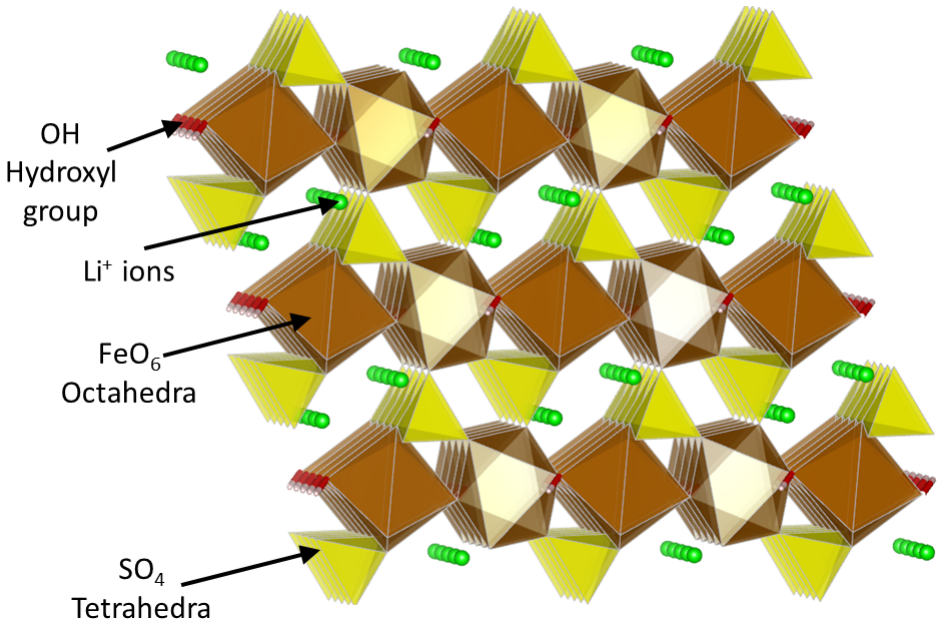

Figure 1.11: The $LiFeSO_4OH$ structure of the tavorite polymorph.

The layered $LiFeSO_4OH$ polymorph crystallises in the monoclinic ($P2_1/c$) space group, with edge-sharing FeO_6 octahedra that form a continuous zigzag chain that runs parallel to the b-axis direction. These chains are connected through shared oxygen vertices to form a layered structure. On each side of the layer of FeO_6 octahedra SO_4 tetrahedra are linked via oxygen vertices, hydroxyl groups form on the remaining oxygen vertices of the FeO_6 octahedra that are not shared with either SO_4 tetrahedra or other FeO_6 octahedra. Two of the oxygen vertices of the SO_4 tetrahedra are not shared with the FeO_6 octahedra and point into the open channel between the layers where the lithium resides, and as such the lithium atoms are tetrahedrally coordinated.

The delithiated tavorite $FeSO_4OH$ also crystallises in the monoclinic space group. However, with no experimental crystal structure reported for the tavorite $LiFeSO_4OH$ polymorph, the structure was set equivalent to that of the related tavorite $LiFeSO_4F$ in the triclinic ($P\bar{1}$) space group as suggested by Tarascon et. al [105] who observed a structural change upon discharging the tavorite $FeSO_4OH$ (C2/c). Hence, the structure of the tavorite $LiFeSO_4OH$ ($P\bar{1}$) polymorph (Figure 1.11) is believed to include chains of alternately orientated corner-sharing $FeO_4(OH)_2$ octahedra, that run parallel to the c-axis direction and share hydroxyl groups located on opposite oxygen vertices. The remaining oxygen vertices of the FeO_6 octahedra are bonded to a sulphur atom forming Fe-O-S-O-Fe chains that cross-link the structure. Unlike the structure of the layered $LiFeSO_4OH$ polymorph, all of the oxygen vertices of the SO_4 tetrahedra are shared with the FeO_6 octahedra.

Within the study presented in **Chapter 5**, the defect chemistry, lithium-ion transport and cell voltage properties of both layered and tavorite $LiFeSO_4OH$ polymorphs are investigated by atomistic modelling and density functional theory (DFT) methods. The combination of these techniques provide fresh insights into the structural van der Waals effects of the two $LiFeSO_4OH$ polymorphs.

For completion, this introductory chapter is concluded with brief overviews of other topical polyanion cathode materials and lithium battery concepts (Li-S, Li-O_2) that are being investigated by the wider research community.

1.5 Other Polyanion Cathodes: Fluorosulphates and Silicates

Considerable research attention has been given to many polyanionic framework cathode materials, some of which will be considered here (Figure 1.12). Firstly, the fluorosulphate family were discovered through structural modifications to the related fluorophosphates [108]. Previous investigations had showed that for certain materials tuning the covalency of the bonds in the polyanion group could increase the operating voltage. For polyanionic LiMXO$_4$ compounds substituting a PO_4^{3-} group with a SO_4^{2-} moiety was found to increase the operating voltage of the Li battery by ~0.6 - 0.8 V [109, 110]. Using such examples, as a proof of concept, an attempt was made to increase the operating voltage of the tavorite structure exhibited by Li_2FePO_4F. Therefore, whilst Li_2FePO_4F has only been shown to offer an operating voltage of 3.0 V, it was hoped that the $LiFeSO_4F$ material would offer a more favourable voltage, therefore producing a cathode with higher energy density capabilities [110, 111].

Tavorite structured $LiFeSO_4F$ (Figure 1.12a) is found to demonstrate excellent performance when implemented as a cathode material, with an operating voltage of 3.6 V and a theoretical capacity of 151 mA h g^{-1} [110]. When compared with the commercially successful $LiFePO_4$, whilst $LiFeSO_4F$ offers a lower capacity, this is offset by greater ionic conductivity and a larger operating voltage. The higher ionic conductivity of the $LiFeSO_4F$ has in part been associated with the 3D network of tunnels present within the material [110].

Based purely on materials cost and sustainability the Li_2FeSiO_4 cathode, which contains naturally abundant iron and silicon, appears to be a highly favourable option for implementation within a lithium battery cell. The structure of Li_2FeSiO_4 consists of a tetragonally packed oxide ion lattice, within which cations occupy half of the available tetrahedral sites. The high level of polymorphism exhibited by Li_2FeSiO_4 can be attributed to the varying nature of the cation ordering between the tetrahedral sites, and the differing tetrahedral geometry. Of the various polymorphs, the first reported structure of Li_2FeSiO_4 (β_{II}) [112] is shown in Figure (Figure 1.12b). Further to this, Li_2FeSiO_4 can also crystallise as either of the γ_S or γ_{II} polymorphs [113, 114], depending on the conditions of synthesis [43, 113].

A high reversible capacity of 140 mA h g^{-1} is offered by the Li_2FeSiO_4 cathode (~80 % of its theoretical value). Due to the nature of the different polymorphs described, the operating potential for a cell containing a Li_2FeSiO_4 cathode depends on which of the three as-prepared

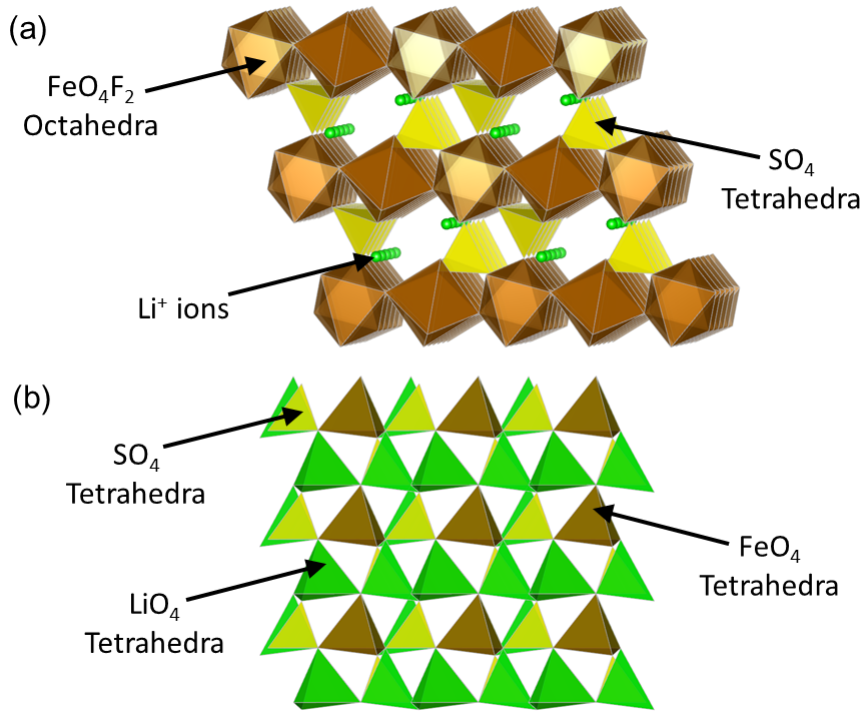

Figure 1.12: Other polyanion cathode materials (a) $LiFeSO_4F$; (b) Li_2FeSiO_4.

structures (β_{II}, γ_S or γ_{II}) is utilised. However, each polymorph is found to offer an operating potential in excess of 3 V. The first charge of Li_2FeSiO_4 is found to occur at ~3.1 V, however, regardless of which as-prepared structure is used, subsequent charges are all found at ~2.8 V. The cause of this voltage drop is the change in structure from those of the as-prepared polymorphs to the cycled structure (inverse-β_{II}) [113, 114].

Due to the electronic conductivity of the Li_2FeSiO_4 cathode being much lower than that of $LiFePO_4$, in addition to its lower operating potential, Li_2FeSiO_4 is not currently considered as a commercial alternative. However, due to the aforementioned favourable properties of this material in terms of cost and sustainability, research is still on-going and improvements will be sought in order to make it a viable option.

1.6 Beyond Li-ion Battery Technologies

The energy storage capabilities of intercalation-based Li-ion batteries, which contain the cathode materials described previously, are superior to all other commercially available recharge-

able battery technologies. However, the energy storage limits of these batteries mean that the long driving ranges ($>$ 400 km), required for road transport applications, will be difficult to be achieved without substantial developments. Therefore new battery technologies are being investigated with the hope of providing significantly improved energy storage capabilities at a reduced cost. There are currently few available technologies to meet the formidable challenge outlined by these requirements. However, both Li-air (also referred to as Li-O_2, as O_2 is the fuel) and Li-S batteries are receiving intense interest at the present time [115–121].

Li-air and Li-S cells (see Figure 1.13) have the potential to offer significantly higher theoretical specific energies than any of the comparative commercial Li-ion cells. This is because, for both of these alternative technologies, an anode made from Li metal rather than graphite is used and Li_2O_2/LiOH/Li_2S store more charge per unit mass than intercalation cathodes, such as $LiCoO_2$ or $LiFePO_4$. However, given that the cathodes cannot consist only of Li_2O_2, LiOH, or Li_2S and instead must include a conductive matrix within which the active discharged products form, mass and volume will inevitably be added to the cathodes. Therefore, the practical energy storage capabilities of these technologies will never reach the values theoretically possible. Whilst, the choice of a Li metal anode is an attractive option due to its high theoretical specific energy, in practice it is found to react with the electrolyte forming a solid electrolyte interface (SEI) layer, comprising lithium salts. In order for the Li anode to function such passivisation is essential, but the continuous reformation of the SEI layer with each charge cycle means that excess lithium is required to compensate for the inefficiency. Moreover, as with all cells, practical energy storage is further reduced by the inclusion of current collectors, packaging and, in the case of Li-O_2 cells, gas diffusion channels [116].

Operation of the rechargeable Li-S cell takes place with reduction of sulphur at the cathode upon discharge forming various polysulphides, which through combination with Li produce LiS_2. Given that sulphur has a high natural abundance and is therefore relatively cheap, it also offers a low equivalent weight and is non toxic. Unfortunately, despite these highly desirable characteristics, Li-S batteries have not yet been commercialised, since during cycling they are found to suffer from, amongst other issues, rapid capacity fade.

The first descriptions of non-aqueous and aqueous Li-air cells were respectively provided by Abraham [122] and Visco [123, 124]. The Li-air cells function as follows: during discharge, oxidation of the Li-metal anode occurs releasing Li^+ ions into the electrolyte with reduction

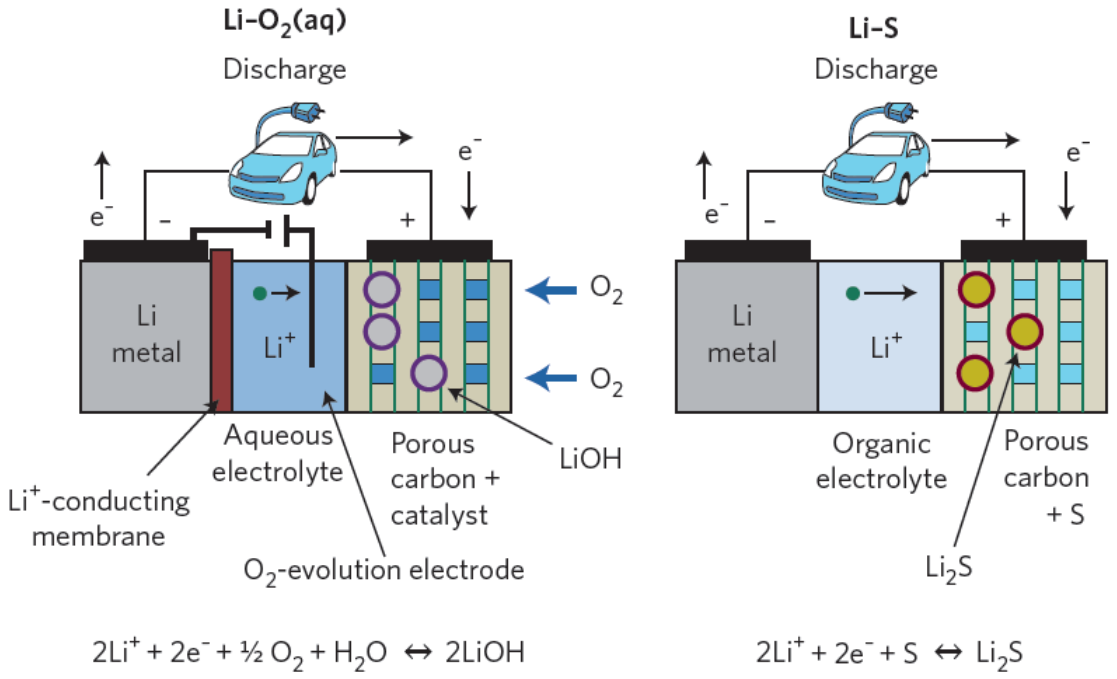

Figure 1.13: Schematic representation of Li-O_2 (aqueous) and Li-S cells [116].

of the O_2, taken from the air, occurring in the cathode pores that are flooded with electrolyte.

When the Li-O_2 cell contains a suitable non-aqueous electrolyte O_2^{2-} is formed, which combines with Li^+ to precipitate the final Li_2O_2 discharge product in the pores of the cathode. Upon charging this process is reversed, with the reformation of Li^+ and O_2 following the oxidation of Li_2O_2. In the case of an aqueous electrolyte, upon discharge OH^- and then LiOH form at the cathode, with the charging cycle resulting in the oxidation of LiOH.

As described above, Li-O_2 cells (aqueous and non-aqueous) offer the highest theoretical specific energy densities for any rechargeable battery technology. Further to which, given that the main constituent of the cathode, O_2, is obviously both free and has a high natural abundance; Li-O_2 cells are therefore prime candidates to meet the demands of the emerging applications in the transportation sector. However, many of the challenges associated with Li-O_2 cells centre on the lithium anode regarding its protection, cyclability, stability, and safety. Hence, in order to optimise the performance of the lithium anode, new Li^+ conductive protective membranes are required; that are thinner/better conductors, more stable, and allow for highly reversible and facile Li stripping and plating [115–117, 119, 120].

Ultimately whilst the Li-S and Li-O_2 battery technologies provide potential avenues to

exceed the stored energy capabilities of the conventional batteries, it is not yet clear if either will become a commercial success, particularly in light of their many drawbacks. In both cases, more intensive research will be needed to address the significant problems associated with these advanced technologies. Therefore, with neither Li-S nor Li-O_2 cells anywhere near to being viable options conventional Li-ion (and indeed Na-ion) batteries will be the most prominent energy storage technology for the foreseeable future. It is exciting to think that the lithium and sodium cathode materials investigated within this thesis could be instrumental in the development of the next generation of conventional Li-ion and Na-ion batteries.

Chapter 2

Computational Methods

2.1 Introduction

The field of computational simulation has undergone significant changes within the past twenty to thirty years; much of this change has arisen due to the development of computational hardware that is substantially more powerful. Whilst computational simulations were initially used to act as an aid for the interpretation of experimental data, they can now be conducted at adequate speed and with sufficient accuracy to provide detailed predictions which can be verified by experimentalists. Indeed, a major aspect of computational modelling is the strong level of cooperation involved between theoreticians and experimentalists [125–130].

These advances enable computational simulations to be successfully deployed to investigate different structural and dynamic properties of solid state ionics at the atomic and sub-atomic level. Lithium insertion sites, migration energies and point defects are examples of the atomic scale features of solid state ionics that can be investigated by computational simulation [128].

Given the difficulty in conducting experimental calculations on certain complex and disordered solids, such as minerals and non-stoichiometric compounds, computational simulation techniques have become a very important tool in the area of solid state chemistry. There are several reasons for the difficulties found in conducting experimental investigations into the various solid state materials. Firstly, it is necessary to determine a significant number of parameters from the structural descriptions of complex and disordered solids. Secondly, for each physical property there is a large and diverse range of contributing mechanisms and thirdly,

there can be many problems involved with the elucidation of specific structural information from certain materials [125].

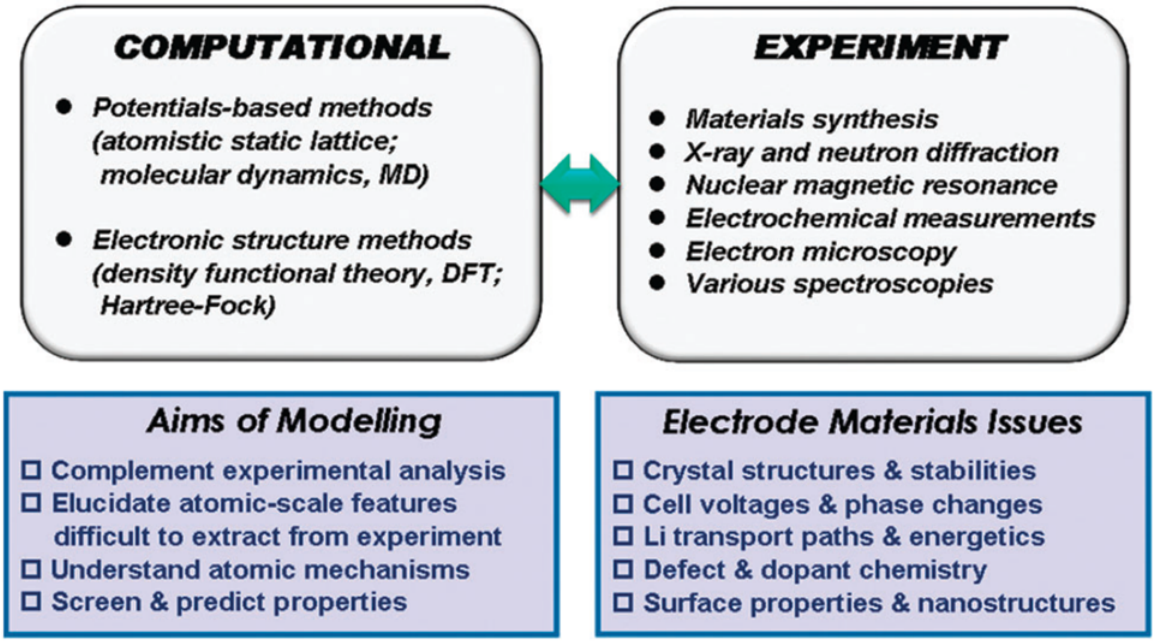

Figure 2.1: A schematic summary of the main computational methods and their aims, the links with complementary experimental techniques and the key materials issues in the development of positive electrodes [20].

In terms of simulation techniques there are three different types available to investigate the properties of the different solid state ionics (Figure 2.1). These techniques include; atomistic simulation, molecular dynamics and quantum mechanical methods [125,128]. All of these techniques are used to some extent in the studies presented within this thesis. For all simulation techniques a description of the interatomic interactions for the material of interest is required. This description of the interatomic interactions can be provided by either an atomistic (potentials-based) approach or derived from the fundamental principles of quantum physics (*ab initio*).

These techniques, detailed in the following sections, have been implemented in several software packages. Firstly, the General Utility Lattice Program (GULP) [127, 131] was used to perform static-lattice atomistic calculations, DL_POLY [132, 133] was used to perform atomistic molecular dynamics (MD) calculations and the Vienna Ab-inito Simulation Package (VASP) [134, 135] was used for static-lattice DFT investigations. As these computational

methodologies are described in extensive detail elsewhere [20, 125, 130, 136–139], this chapter serves to provide a more general overview.

2.2 Energy Minimisation

For a given chemical system the potential energy can be defined as a function of the coordinates for all N atoms within that system. Therefore the potential energy for all solid-state systems is dependent upon the positions of all constituent particles. This function is known as the potential energy (hyper)surface, with each point on the surface representing a different configuration of atomic coordinates. Due to the multidimensional nature of the potential energy surface function, it is difficult to visualise and evaluate the surface in its entirety. However, by using key component coordinates, chemical systems can often be approximated allowing certain subsets of the function to be visualised and evaluated leading to greater understanding.

For a given potential energy surface function the most important features, for the studies presented in this thesis, correspond to two principal types of stationary point:

Minima Such points represent stable states for chemical systems. For some systems multiple minima can be found, which correspond to separate polymorphs (chemical structures). The 'global minimum' refers to the lowest energy minimum and as such the structure favoured thermodynamically. All other minima, that are not the 'global minimum' are known as 'local minima'.

Saddle-point This is the name given to the point of maximum energy which can be found on the lowest energy path between two stable (minima) structures. A saddle-point is therefore referred to as a transition state. Transition states are vitally important to aid understanding of chemical systems since their presence indicates a reaction pathway, thus enabling the activation barrier to the reaction (difference in energy between the transition state and the reactant species) to be calculated.

The first derivatives of the potential energy surface function, with respect to distance, are zero for both of these principal types of stationary point (minima and saddle-points). However, the type of stationary point can be distinguished by analysis of their second derivatives with respect to distance. At a minimum the eigenvalues of the Hessian matrix of second derivatives

are all positive, whilst at a saddle-point one of the eigenvalues of the second derivative Hessian matrix is negative.

Given the descriptions above, it is not surprising that locating stationary points on the potential energy surface is of particular importance within the field of computational chemistry. In order to find such stationary points there are a range of energy minimisation algorithms, however problems and inefficiencies can arise when using these algorithms due to the complex nature of the potential energy function. These issues can be overcome by making the assumption that when close to the minima the potential energy function is harmonic (quadratic).

Energy minimisation is a very simple concept; by adjusting the structural parameters (cell dimensions and atomic coordinates) that define the energy of the crystal, it is possible to obtain the minimum energy configuration. There are several different available techniques for energy minimisation. Of these, the 'search' procedure is the easiest to comprehend since locating the global energy minimum simply requires scanning the parameter space. Unfortunately, in the majority of cases, this method is not particularly effective and so it is rarely applied and consequently other techniques of energy minimisation are used. However, given that these other energy minimisation techniques incorporate relatively complicated mathematical formulas, it is important for large solid state lattices to use the most appropriate technique or combination of techniques so that the global minimum can be obtained without using large amounts of computer time [125].

An example of a technique that is used more often than the 'search' procedure is the gradient (first-order minimisation) technique, which requires that the first derivative of the energy function (E_i) is calculated in terms of the atomic coordinates that are being varied (x_i) [125], as shown by equation 2.1.

$$g_i = \frac{\delta E_i}{\delta x_i} \tag{2.1}$$

Over the course of the following subsections the discussion will highlight several derivative-based energy minimisation techniques.

2.2.1 Steepest Descent

Of the available first derivative energy minimisation techniques, the steepest descent algorithm is the simplest, enabling the minimum to be found iteratively. In this technique the atomic coordinates are changed in the direction that enables the largest energy decrease, or in other words, the steepest gradient. If a system is described as having N atoms, then the corresponding direction in which the 3N Cartesian coordinates are moved can be illustrated by a 3N-dimensional gradient unit vector, denoted r_{i}, which points in the opposite direction to the gradient vector (g_{i}) as shown by equation 2.2.

$$r_i = -g_i \tag{2.2}$$

After deciding upon a direction in which to move, it is then necessary to define the distance to move along the gradient. Unfortunately, given that the potential energy function has been assumed to be quadratic, it is not possible to determine this distance analytically. Instead, this distance can be determined by either taking a step of arbitrary length (a_{i}) or by conducting a line search. However, adopting the line search technique to find the new coordinates along a_{i} may involve using a large amount of computer time; hence applying the arbitrary step length approach may be a preferable means to determine the distance to move. Using the step length approach, the new set of coordinates after a step i can be calculated from equation 2.3, where a_{i} denotes the step length, x_i the coordinates of the initial configuration and $x_{\mathrm{i+1}}$ the coordinates of the refined configuration.

$$x_{i+1} = x_i + \alpha_i r_i \tag{2.3}$$

The gradient at the minimum of the line search ($g_{\mathrm{i+1}}$) must not have any component in the direction of the line search, therefore the next iteration of the steepest descent algorithm will be orthogonal to the direction of the previous step. As a result the steepest descent method gradually converges on the minimum by a series of right angled turns.

The steepest descent algorithm provides an excellent method for removing the highest-energy features from an initial configuration since, for the direction of movement at each step, r_{i} is determined by the largest interatomic forces. Further to this, the steepest descent

algorithm is a very robust approach when the initial configuration is far from the minimum, in such cases a quadratic approximation holds less validity. However, because of all the right angled turns, it is a technique that is relatively inefficient at locating the minimum. This is particularly the case when proceeding down a long and narrow energy well as lots of iterations involving small steps may be required to locate the minimum [139].

2.2.2 Conjugate Gradients

The conjugate gradients algorithm can be regarded as a theoretical advancement on the steepest descent method, since the repeated re-introduction of errors with each separate iteration is eliminated. Unlike the steepest descent algorithm which minimises the energy of a series of orthogonal lines, the conjugate gradients algorithm uses a set of orthogonal search vectors $d_{(0)}$, $d_{(1)},\ldots,d_{(n-1)}$, and minimises the energy once. Minimising the energy with respect to each direction locates the minimum on the energy surface.

The conjugate gradients algorithm generates a new search vector (d_i) using the previous search vector (d_{i-1}) in addition to both the previous gradient (g_{i-1}) and current gradient (g_i) according to:

$$d_i = -g_i + \beta_i d_{i-1} \tag{2.4}$$

where

$$\beta_i = \frac{g_i \cdot g_i}{g_{i-1} \cdot g_{i-1}} \tag{2.5}$$

Minimising the energy function in this new direction enables a position closer to the minimum (x_{i+1}) to be generated:

$$x_{i+1} = x_i + \alpha_i d_i \tag{2.6}$$

With no previous gradient information the first iteration is the same as the corresponding step within the steepest descent algorithm, since the direction of steepest descent ($-g_i$) provides the initial search direction. The same line search technique is used to determine the step length (a_i) for each iteration.

The conjugate gradients method is more efficient than steepest descent with fewer iterations

required to locate the minimum energy; n steps will be needed to find the minimum for a quadratic function of n variables. Additionally, convergence towards the minimum is not hindered by the shape of the potential well. Therefore, the continuous zig-zag paths often required to find the minimum via steepest descent are not replicated. Moreover, the time of calculation for each step is relatively quick as only first derivative information is used in the conjugate gradients algorithm. However, the main problem with the conjugate gradients algorithm is the need to define a set of suitable search directions.

2.2.3 Newton-Raphson

The Newton-Raphson method is another iterative approach that is widely used to locate minima. Unlike the previously described steepest descent and conjugate gradients algorithms, the Newton-Raphson method is a second order technique, that converges on the minimum through first- and second-derivative information. Within this method, each new iteration ($x_{\mathrm{i}+1}$) is generated by using the atomic coordinates of the current configuration (x_{i}) and subtracting the corresponding gradient for that point (g_i) multiplied by the inverse Hessian matrix (H_i^{-1}). Therefore, the atomic coordinates are continually updated according to equation 2.7.

$$x_{i+1} = x_i - H_i^{-1} g_i \tag{2.7}$$

If the potential energy surface function is perfectly harmonic (a true quadratic) the Newton-Raphson approach will only need one step in order to find the minimum energy. However, as previously described, real chemical systems are not found to be perfectly harmonic, and therefore to locate the minimum the Newton-Raphson technique must be applied iteratively. Rapid convergence is provided by this approach when the configuration being evaluated is close to the minimum since, in this case, it is a valid assumption that the potential well is harmonic. When the configuration to be evaluated is further from the minimum Newton-Raphson is a less useful technique, as the potential energy surface cannot be assumed to be harmonic, hence minimisation can become unstable. Therefore, it is particularly important for this method to choose a suitable atomic configuration for the structure before starting the optimisation. For cases where the initial configuration is likely to be far from the minima, due to unavailability or inaccurate experimental structural data, a more efficient method may be to use a more robust

energy minimisation technique. In such circumstances either the steepest descent or conjugate gradients techniques are often used initially, in order to provide a configuration closer to the minimum, before switching to Newton-Raphson to accurately locate the energy minimum.

Whilst the use of the Hessian allows for faster convergence of the Newton-Raphson technique when near minima, the calculation and inversion of the Hessian matrix can be regarded as relatively computationally expensive. Fortunately, it is possible to make use of the fact that the Hessian (local shape of the energy surface) generally does not show significant change from consecutive iterations. The Broyden-Fletcher-Goldfarb-Shanno [140] (BFGS) update scheme is incorporated within the GULP code [127, 131] in order to approximate changes within the Hessian between each optimisation step. Using BFGS the full Hessian is only recalculated and inverted after certain criteria have been realised:

- The energy of the system falls by a value that exceeds a predefined cut-off value.
- There is a significant difference between the directions of the search vector and the gradient vector.
- The energy minimum cannot be located within the search direction.
- A predefined number of consecutive iterations are performed without the Hessian being recalculated.

2.2.4 Finding Transition States

Our energy minimisation discussion has thus far focused on locating only one type of stationary point on the potential energy surface, up until now this has been energy minima. However, in addition to finding energy minima, which can inform us about the stability of various structures, we are also interested in the kinetics of reactions (rate of conversion between stable structures). By locating the other type of stationary point, known as saddle-points (or transition states), we are able to determine energetic barriers for certain chemical events and determine the frequency with which they occur. This is possible since transition states can be found at positions of maximum energy along the minimum energy pathways, between stable (minima) reactant species.

For a given saddle-point, the Hessian matrix will contain one or more negative eigenvalues corresponding to one or more directions which point down on the potential energy surface. For the calculations described in this thesis the focus has been on first-order transition states, for which the Hessian only has one negative eigenvalue. Such transition states correspond to maximum energetic points along single pathways connecting two minima (stable reactant species), as described previously. For all directions perpendicular to the pathway connecting the stable reactant species these transition states are themselves minima. There are numerous methods available to find such transition states; the two techniques used in this work are constrained minimisation and nudged elastic band. Both of these techniques involve mapping out a series of points along the pathway of minimum energy connecting the two minima; this provides an estimate of the transition state energy, which corresponds to the point of highest energy.

Within this thesis, transition state minimisation techniques have been applied in the simulations in order to find activation barriers to both lithium and sodium migration for a range of cathode materials. The alkali-ion (lithium and sodium) migration processes for such materials, typically involve the incremental movement of a lithium or sodium ion from one crystallographic lattice site to a neighbouring vacant site.

Constrained Minimisation

Constrained minimisation is a simple method for determining energetic barriers to alkali-ion migration. The technique requires that the migrating species is placed at a series of incremental positions between two vacant crystallographic sites. For each incremental position occupied by the migrating species an energy minimisation algorithm is applied, however the motion of the migrating species is constrained in one direction (often the direction of the pathway). By constraining the motion of the migrating species in the direction of the pathway, relaxation of the species can occur in the directions perpendicular to the pathway thus finding the lowest energy route for alkali-ion migration. Using this knowledge, the corresponding energetic barrier to alkali-ion migration is simply the difference in energy between the starting point (often an alkali-ion vacancy) and the position of highest energy (the transition state).

Unfortunately, application of this transition state minimisation technique within the GULP code [127, 131] presents an important drawback; in that it is only possible for constraint to

be applied along the cartesian axes. This creates a problem for the technique since migration pathways are often not found to correspond with the cartesian axes, except for cases involving relatively simple systems with high symmetry. Apart from such high symmetry cases, the resulting relaxation produced by the constraint along the cartesian axes will not be directly perpendicular to the direction of the migration pathway. Therefore, direct comparison between the energetics of a linear (non-relaxed) migration pathway and a non-linear (relaxed) migration pathway are less trivial.

In essence, the main failing of the constrained minimisation technique is that it requires a significant amount of user input. However, it remains a very robust method for transition state minimisation and is found to show excellent results, particularly when applied to high symmetry crystal structures.

Nudged Elastic Band (NEB)

The nudged elastic band (NEB) method [141–143] is another transition state minimisation technique that can be employed to find the minimum energy pathway between two stable structures (minima). As with the constrained minimisation technique described above, a requirement of NEB is that both the initial and final states are known.

A typical NEB calculation involves the creation of a set of starting structures (also known as replicas) between the initial and final structures via a process known as linear interpolation. Initially, the set of replicas maps out a route between the initial and final structures, which is directly linear and serves as an initial guess at the minimum energy pathway for the migrating species. The replicas are all linked to their neighbouring replicas by a spring force, mimicking the concept of an elastic band. The spring force acts to hold the replicas together, and as such attempts to maintain the spacing between the replicas. Energy minimisation of the replicas takes place simultaneously resulting in the 'band' locating the pathway of minimum energy for the specific migrating species.

In order to stop the spring forces from interfering, with both the minimisation of the replicas and the atomic forces affecting the distribution of those replicas, a force projection is used. As a consequence only two components contribute to the energy minimisation of the band; the spring forces parallel to the band and the interatomic forces perpendicular to the band.

The NEB method is especially useful for determining the energetic barriers to alkali-ion migration within materials that have low symmetry crystal structures, for which the migration pathways are unlikely to be parallel to the cartesian axes. NEB calculations function using periodic boundary conditions. Therefore, it is important to use sufficiently large simulation cells in order to avoid interactions between replicas in neighbouring periodic images becoming significant.

2.3 Periodic Boundary Conditions

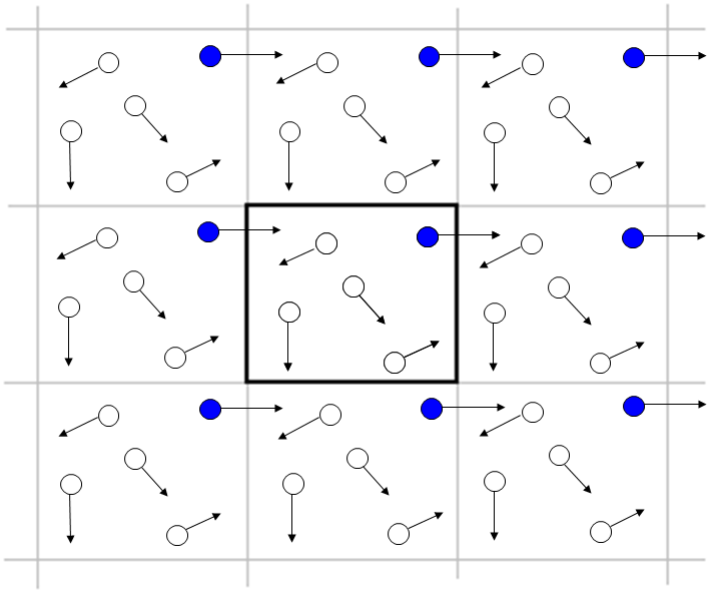

Figure 2.2: A schematic representation of periodic boundary conditions in two dimensions.

The use of periodic boundary conditions is essential for modelling the interatomic interactions in large extended solid state systems, since they reduce the amount of computational time required for simulation. Due to their symmetry, crystalline solids can be divided into unit cells consisting of relatively small numbers of atoms, ions or molecules. These units cells can then be repeated continuously in all three dimensions.

During a simulation the unit cell of interest is surrounded in all three dimensions by identical images of itself. These images enable the ions contained within the unit cell to

interact with each other, as well as the other ions contained within the images. The ions within the images only interact with the ions contained within the unit cell. Therefore, the periodic boundary conditions perform an essential role in making the simulation cell 'feel' as if it is part of a large extended solid state system. The theory behind the use of periodic boundary conditions is shown in Figure 2.2.

2.4 Molecular Dynamics

In the previous section various techniques of energy minimisation were outlined; often referred to as static lattice simulations. These techniques describe systems at absolute zero and as a consequence contain no kinetic energy information. Such calculations focus entirely on the potential energy of the system, and whilst vast amounts of information can be obtained from static lattice simulations, the effects of thermal energy are not considered.

In Molecular Dynamic (MD) simulations all atoms are assigned a velocity, therefore the kinetic energy of the atoms is included explicitly. The combined effect of all the velocities provides the system with temperature. A significant disadvantage of energy minimisation techniques (discussed in Section 2.2) is that they only travel down hill on the potential energy surface. In contrast MD simulations provide additional kinetic energy, which can allow the system under study to overcome local energetic barriers and potentially find configurations that offer improved thermodynamic stability. However, in reality even long timescale calculations often only allow for relatively short real-time simulations of systems, hence it is usually only possible to overcome energetic barriers of the order of a few $k_B T$.

Beyond enabling a larger amount of the potential energy surface to be explored, MD simulations can provide greater understanding to researchers, including information regarding time averaged structures and diffusion processes. The following section outlines the basis of such MD simulations. Further detailed information regarding the theory that underpins MD techniques can be found in the extensive reviews available [132, 133, 139].

The simulation of dynamic properties, including crystal vibrations and ion transport, requires a method to calculate the ion trajectories in order to describe how the velocities and positions of the ions change with time. Effectively this requires that Newton's laws of motion are integrated for the whole system within a finite period of time. Knowing the force (f) that

acts upon an atom allows for the acceleration (a) of that atom to be determined, since it is the second derivative of the atom's position (r) with regard to time (t).

$$f = m\frac{d^2r}{dt^2} = ma \tag{2.8}$$

For a simple example, such as when the force acting between ions remains constant the current positions and velocities after a change in time (dt) can be calculated from equations 2.9 and 2.10 respectively.

$$r_{t+dt} = r_t + v_t dt + \frac{1}{2}a_t dt^2 \tag{2.9}$$

$$v_{t+dt} = v_t + a_t dt \tag{2.10}$$

However, for real systems the forces acting on an ion will change based on the separation of the ion from the other ions, therefore equations 2.9 and 2.10 only hold true for infinitesimal changes in time. Since this is a coupled many-body problem, the motion of ions can only be described over greater time-scales, which offer more statistical relevance, by using numerical integration algorithms.

2.4.1 Integration Algorithms

In order to update ion trajectories over a finite time step integration algorithms are employed. These algorithms separate the integration into a series of discrete steps, each of which are separated by a finite time (Δt). For each individual ion, the force acting upon it at a given time (t) is calculated by summing the interaction of that ion with all other ions within the system. Determined from the force, the acceleration is combined with the velocities and positions at time t in order to generate the updated velocities and positions at time $t+\Delta t$. Between the times t and $t+\Delta t$ a constant force is assumed, which gives rise to the main source of inaccuracy within this methodology. This overall process is repeated throughout the run-time of the simulation.

In order to integrate the equations of motion there are numerous different integration algorithms available. However, all use a Taylor series expansion (described below) to approximate the velocities, positions and accelerations. By reducing the time step and including higher

order terms from the Taylor series expansion it is possible to improve the accuracy of the properties calculated.

The Verlet algorithm [144] (a form of which is used for the MD calculations in this thesis) is used widely in MD simulations. Derivation of the Verlet algorithm is made possible by approximating the trajectory of ions as a Taylor series about the current set of ion positions (r_t) truncated at the term of the third derivative.

$$r_{t+\triangle t} = r_t + v_t \triangle t + \frac{a_t}{2} \triangle t^2 + \frac{b_t}{6} \triangle t^3 + \theta(\triangle t^4) \tag{2.11}$$

where v_t, a_t and b_t respectively represent the velocities, accelerations and jerks (acceleration changes); θ represents an error term. Note that the first, second and third derivatives of position with respect to time are represented by the velocity, acceleration and jerk.

$$v_t = \dot{r_t} \tag{2.12}$$

$$a_t = \dot{v_t} = \ddot{r_t} \tag{2.13}$$

$$b_t = \dot{a_t} = \ddot{v_t} = \dddot{r_t} \tag{2.14}$$

Of these, the b term, which effectively accounts for the change in force is difficult to compute. Fortunately, Verlet devised a clever mathematical trick in order to overcome this obstacle, which involved the use of information from the previous time step ($r_{t-\triangle t}$). This enabled the information of the third derivative to be included implicitly.

Using the same derivation strategy as equation 2.11, the Taylor series at t-Δt is:

$$r_{t-\triangle t} = r_t - v_t \triangle t + \frac{a_t}{2} \triangle t^2 - \frac{b_t}{6} \triangle t^3 + \theta(\triangle t^4) \tag{2.15}$$

Therefore the overall Verlet algorithm is given by the sum of equations 2.11 and 2.15, as shown below:

$$r_{t+\triangle t} = 2r_t - r_{t-\triangle t} + a_t \triangle t^2 + \theta(\triangle t^4) \tag{2.16}$$

By using the information contained within the previous time-step the Verlet algorithm eliminates the requirement to calculate the third derivative term. However, there is a down-side to this approach in that the error will increase. This is due to the fact that the errors inherent from the calculation of both r_t and $r_{t-\triangle t}$ are both carried forward and used in the approximation of $r_{t+\triangle t}$.

Although explicit calculation of the velocities is not a necessary requirement of the Verlet algorithm, given that the ion trajectories can be generated without them, they remain an important quantity to compute. Knowledge of the velocities is of importance, not least because they are scaled to maintain the temperature of the system, but also since it is necessary to compute the kinetic energy in order to calculate the total system energy. The velocities can be recovered from the Verlet trajectory by subtracting equation 2.11 from equation 2.15, as shown:

$$v_t = \frac{r_{t+\triangle t} - r_{t-\triangle t}}{2 \triangle t} + \theta(\triangle t^2) \tag{2.17}$$

From this equation it is clear that, until the positions have been calculated at the next step, the velocities cannot be computed. Also the calculation of velocities using this approach introduces a greater degree of numerical inaccuracy, with the error being of the order of $\triangle t^2$.

Many of the deficiencies associated with the Verlet algorithm are avoided in the widely-used variant of the Verlet algorithm, known as the Verlet-leapfrog. All molecular dynamics calculations within this thesis were based on simulations performed using DL_POLY (version 2.2), for which the Verlet-leapfrog algorithm is the default. Within the Verlet-leapfrog algorithm the velocities are evaluated at half time-steps:

$$v_{t-\frac{1}{2}\triangle t} = \frac{r_t - r_{t-\triangle t}}{\triangle t} \tag{2.18}$$

$$v_{t+\frac{1}{2}\triangle t} = \frac{r_{t+\triangle t} - r_t}{\triangle t} \tag{2.19}$$

Therefore, an expression for the calculation of the new positions from the previous positions and velocities at the half time-step is:

$$r_{t+\triangle t} = r_t + v_{t+\frac{1}{2}\triangle t} \triangle t + \theta(\triangle t^4) \tag{2.20}$$

with the velocities updated according to:

$$v_{t+\frac{1}{2}\triangle t} = v_{t-\frac{1}{2}\triangle t} + a_t \triangle t + \theta(\triangle t^3) \tag{2.21}$$

Implementing the Verlet-leapfrog algorithm requires that the accelerations at the current time-step are calculated by evaluating the forces, and are used in order to generate velocities from the previous $t-\frac{1}{2}\triangle t$ to an updated set at $t+\frac{1}{2}\triangle t$ by using equation 2.21. By updating the velocities, they in effect "leapfrog" the current positions at the current time-step (t). Following this equation 2.20 is then used to update the positions at $t+\triangle t$, this time "leapfrogging" the velocities (hence the Verlet-leapfrog algorithm name), and the process continues.

The main advantage of the Verlet-leapfrog algorithm in comparison to the Verlet algorithm is that it includes the velocities explicitly, hence they are calculated with an order of magnitude greater accuracy. However, the Verlet-leapfrog does present a clear disadvantage in that the positions and velocities are no longer synchronised, therefore preventing an accurate calculation of the kinetic and potential energy contributions at the same time. Calculation of the full-step velocities requires that two centred half-step velocities are averaged, as shown in equation 2.22:

$$v_t = \frac{1}{2}(v_{t+\frac{1}{2}\triangle t} + v_{t-\frac{1}{2}\triangle t}) + \theta(\triangle t^2) \tag{2.22}$$

However, it should be noted that, in order to calculate the full-step velocities equation 2.22 carries forward the inherent errors within both half-step velocities, hence the value determined for v_t is less accurate.

It is also worth noting that neither the Verlet nor the Verlet-leapfrog algorithm are self starting, because they both require information from the previous step. Therefore, velocities are initially assigned. In practice they are assigned randomly, whilst importantly ensuring that the system starts at the desired temperature and that it has no translational momentum. The conditions required are shown in equations 2.23 and 2.24, where the number of atoms is represented as N and the Boltzmann constant is denoted k_B.

$$\sum_{i=1}^{N} m_i v_i^2 = 3Nk_BT \tag{2.23}$$

$$\sum_{i=1}^{N} m_i v_i = 0 \tag{2.24}$$

2.4.2 Time Step and Equilibration

Choosing an appropriate value for the time-step ($\triangle t$) within MD simulations is both highly important and non-trivial. If the value chosen for the time-step is too small, then the simulations will take an unnecessarily long time to move through the different states available in the system. However, if a value that is too large is chosen, then there is the potential of instabilities arising which can lead to ions moving unphysical distances or colliding with excessive energy; this can cause the simulation to fail. The ideal choice for the time-step value would be as large as possible, thus enabling the calculation to quickly simulate as much "real time" as possible, but without any instability. In practice values ranging between 0.1 and 1 femto-seconds are found to be appropriate for such calculations.

The equilibration period is the initial stage of an MD simulation. This period is designed to allow the starting configuration of the system with its accompanying assigned velocities to reach a state of equilibrium. Within the equilibration time period several properties of the system are monitored, including the total energy which is the sum of the potential energy from the atomic arrangement, and kinetic energy due to atomic motion. When these properties have 'settled' into a steady pattern equilibrium is achieved. In order to ensure a satisfactory level of convergence the equilibration period is often set to last for tens of thousands of time-steps. Upon completion of the equilibration period the production phase can commence. It is from the production phase that the desirable statistics of the calculation can be extracted.

2.4.3 Ensembles

An ensemble describes the set of constraints applied to a system that gives rise to the distribution of thermally accessible states. Throughout the duration of an MD simulation the atomic coordinates of the system under study vary with time. Therefore, the different atomic arrangements of the system correspond to different states; with the different types of ensemble

requiring different sets of constraints.

The micro-canonical (NVE) ensemble maintains a constant number of atoms (N), volume (V) of the simulation cell and total energy (E). Whilst the total energy of the micro-canonical (NVE) ensemble remains constant the potential and kinetic energy contributions can change. The conserved quantity of the total energy can be represented according to equation 2.25:

$$\mathscr{H} = \mathscr{K} + \mathscr{V} \tag{2.25}$$

where the Hamiltonian ($\mathscr{H}$) is an operator which corresponds to the total energy of the system, which consists of contributions from the kinetic ($\mathscr{K}$) and potential energy ($\mathscr{V}$) components.

Since the micro-canonical ensemble allows for large variations in temperature and pressure, the conditions produced are different from the 'real' conditions under which most experimental investigations take place. Of the alternatives to the micro-canonical ensemble, the canonical (NVT) and isobaric-isothermal (NPT) ensembles are the most commonly used. The canonical ensemble allows the system under study to be probed as a function of temperature, whilst the isobaric-isothermal ensemble allows the system to be studied as a function of pressure. Controlling both the temperature and pressure during the simulation of systems is important, this is made possible using mathematical thermostats and barostats. An additional benefit of simulating systems under controlled conditions is that the controls help to compensate for the slow accumulation of rounding errors that develops over time.

The instantaneous temperature of a system is proportional to the average kinetic energy of the constituent atoms within that system, which is directly related to the velocities of the atoms:

$$T \propto \frac{1}{2} \sum_{i=1}^{N} m_i v_i^2 \tag{2.26}$$

Hence, an easy way to provide temperature control, and ensure that the system maintains the required temperature, is to scale the velocities at each step. However, this approach would produce an unphysical model, since no fluctuations in temperature would be allowed.

The MD simulations described in this thesis use an improved thermostat that was de-

veloped by Berendsen [145], for which the simulation cell is coupled to a fixed temperature hypothetical external heat bath (T_{bath}). At each step the velocities are scaled so as to keep the rate of change of temperature proportional to the temperature difference between the simulation cell and the heat bath:

$$\frac{dT(t)}{dt} = \frac{1}{\tau}(T_{bath} - T(t)) \tag{2.27}$$

where the empirical parameter (τ) is used to determine the strength of the coupling between the simulation cell and the heat bath.

Care needs to be taken when selecting the value of the empirical parameter (τ), since at low values there is strong coupling giving rise to unrealistically small temperature fluctuations. Whilst for high values of τ the coupling is weak, therefore as $\tau \to \infty$ the Berendsen thermostat is effectively removed, resulting in the simulation imposing the constraints of the micro-canonical (NVE) ensemble. Typically, for MD simulations of condensed-phase systems, the value of $\tau \sim 0.1$ ps.

In order to scale simulation cell volume, rather than temperature, it is possible to alter the Berendsen thermostat in order to provide a barostat. A similar theory applies when acting as a barostat, with the simulation cell now connected to a hypothetical external pressure bath. Using the Berendsen barostat the rate of change of pressure can be calculated such that:

$$\frac{dP(t)}{dt} = \frac{1}{\tau}(P_{bath} - P(t)) \tag{2.28}$$

again τ represents an empirical coupling parameter (determining the strength of the coupling between the simulation cell and the pressure bath) with the pressure of the bath denoted P_{bath}. Depending on the pressure difference the positions of the atoms are simply scaled so that the simulation cell is compressed or expanded as appropriate.

2.4.4 MD Data Analysis

The production phase of MD simulations can provide much useful data for different systems, regarding such properties as the diffusivity of ions and time averaged structures. It is possible to directly extract the data for these properties from the simulated ion trajectories.

Radial Distribution Function

The radial distribution function (RDF) gives a useful and informative insight into the structure of the dynamic system under study. Using a specific atom as a reference the RDF describes how the density of the system changes upon moving spherically outward from the reference atom. The RDF can be defined as the probability of finding an atom at a distance (r) from the reference atom, relative to that for an ideal gas. Further to this the RDF quantifies the ordering in a material, both in terms of the amount and the range, and given that it can also be generated using experimental diffraction techniques it is a useful comparative tool.

Generation of an RDF occurs by sorting the atoms that neighbour the reference atom into a series of distance 'bins' or histograms (as shown in Figure 2.3). A thickness ($\triangle r$) provides the separation between each bin, with the number of neighbour atoms present within each bin summed and then averaged over the entire ensemble.

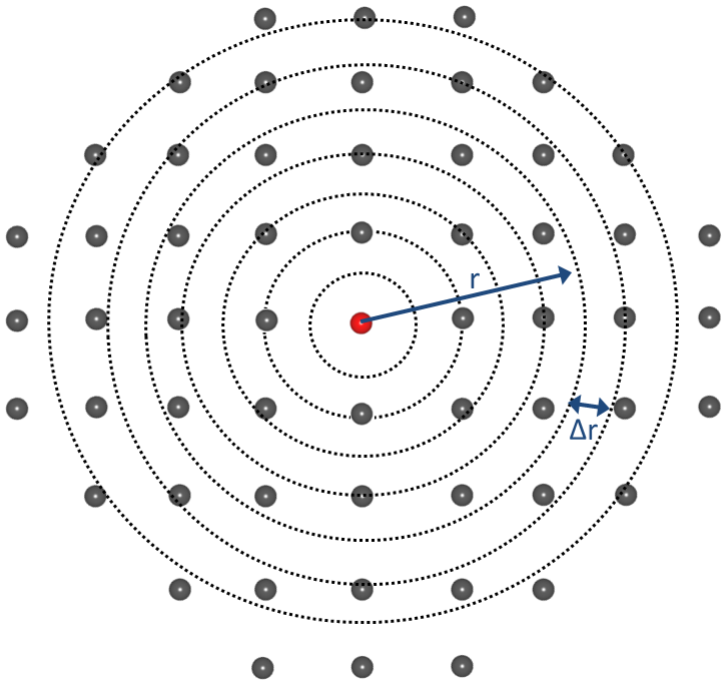

Figure 2.3: Schematic showing a regular crystal lattice cross section. The 'bins' are represented by the dotted lines. Each bin has maximum radius r and thickness $\triangle r$.

The radial distribution function denoted $g(r)$ can be defined according to equation 2.29:

$$g(r) = \left\langle \frac{V}{N^2} \sum_{i,j=1}^{N} \delta\left(r - r_{ij}\right) \right\rangle \tag{2.29}$$

where the angle brackets denote that the RDF is the mean value of all configurations. N is the total number of atoms, r_{ij} is the distance between the atoms (i, j) and δ is a function which is non zero for small input values. Therefore, pairs of atoms are only 'counted' when their separation (r_{ij}) is close to the desired value of r. V is the volume of a spherical shell of inner radius r and thickness $\triangle r$, given by:

$$V \approx 4\pi r^2 \triangle r \tag{2.30}$$

which accounts for the increasing numbers of atoms in shells of increased radius within an ideal gas.

For the crystalline types of material detailed throughout this thesis the RDF plots would consist of a series of sharp peaks with similar separations. The cathode materials described within this thesis would be expected to produce such RDF plots, since the atoms in these crystals adopt regular ordered lattice structures, hence the atomic density will vary regularly with distance. An example RDF plot of a crystalline material (similar to those described in this thesis) is shown in Figure 2.4.

Time-Averaged Densities

In systems, such as cathode materials for lithium-ion or sodium-ion batteries, where ionic diffusion/migration occurs it can be particularly useful to visualise the associated mechanisms. One possible way to achieve such an insight is provided by time-averaged atomic density plots of the simulation cell. These plots are generated directly from the ion trajectory data and allow for the various pathways of the ions within the system to be viewed.

The approach taken to generate such plots requires splitting the simulation cell into a grid of three-dimensional boxes. At each time step the position of the specified atoms are all superimposed with the total number of atoms in each three-dimensional box counted and the final data set normalised. This process ultimately yields a density image, which shows all the areas of the simulation cell through which the chosen ion has moved during the calculation.

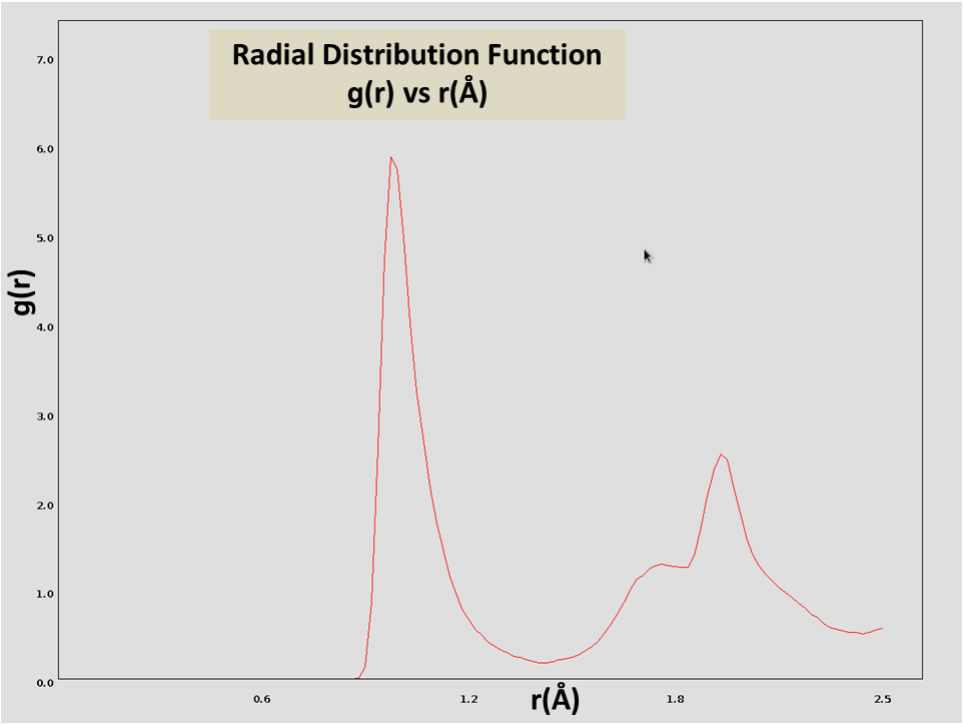

Figure 2.4: Example radial distribution plot for a crystalline material. Note the presence of well defined peaks at large ion separations.

As a technique this produces similar output to the results obtained from the experimental neutron diffraction maximum entropy method (ND-MEM).

Mean Square Displacement

Mean square displacement (MSD,$\langle r_i^2 \rangle$) provides a measure of the distances moved by the atoms within the simulation cell in relation to the atomic coordinates of their initial location. Therefore, through examination of MSDs with respect to time it is possible to gain valuable information regarding the diffusion rates of atoms within different systems. An MSD is calculated by determining the square of the displacement of each atom from its initial location at time t, with the mean calculated over all the examined atoms, as shown in equation 2.31:

$$MSD(t) = \frac{1}{N} \sum_{i=0}^{N} \mid r_i(t) - r_i(0) \mid^2 \tag{2.31}$$

where N is the total number of atoms, and $r_i(0)$ and $r_i(t)$ are the initial and current positions of atom i respectively. It is common practice for $r_i(0)$ to be reset, as a further

averaging technique, when generating an MSD vs. time data set.

The gradient of the MSD plot, when considered for sufficiently long time-scales, is directly related to the self-diffusion coefficient (D) for the atomic species of interest according to the Einstein relation (equation 2.32):

$$MSD(t) = 2dDt \tag{2.32}$$

where d denotes the system's dimensionality. Hence, when considering systems in three-dimensions:

$$D = \frac{1}{6} \lim_{t \to \infty} \frac{d}{dt} MSD \tag{2.33}$$

Further to this using an Arrhenius plot, with diffusion data gained from a set of MSDs produced at different temperatures, it is possible to estimate the activation energy barrier for migration of the species of interest. For calculation of activation energy barriers to migration the Arrhenius takes the form shown in equation 2.34:

$$\ln D = \frac{-E_a}{RT} + \ln A \tag{2.34}$$

where the gas constant is denoted R. From the Arrhenius equation the gradient of the slope, produced by plotting $\ln D$ vs. $\frac{1}{T}$, will be proportional to the activation energy (E_a) and the intercept will be equivalent to the pre-exponential factor A. This is an example of the insights and information, with regard to activation energy barriers, that can be provided by MD simulations, but which cannot be accessed by static lattice simulations.

2.5 Atomistic Modelling

Both the energy minimisation and molecular dynamics (MD) techniques, discussed in the previous sections, require that the forces between atoms (interatomic interactions) are evaluated at each step. The remainder of this methodology chapter focuses upon the description of such interatomic interactions and their use to calculate the total energy of a system. The description of such interatomic interactions can be separated into two distinct methodologies: atomistic techniques; and *ab initio* techniques.

Atomistic simulation techniques (discussed in this section) employ simple empirically derived equations to describe the interatomic interactions. In comparison *ab initio* techniques (discussed in Section 2.6; Electronic Structure Techniques) are based upon the fundamental principles of quantum mechanics, and as such present an increased level of complexity. For theoreticians the choice between which of these different techniques to employ is often determined by the information required coupled with the computational time and resources available.

Using atomistic techniques it is possible to simulate large numbers (tens of thousands) of atoms. Hence such methods are particularly suited to modelling the relaxation around defects, the influence of which can extend significantly into the crystal lattice of a system. Atomistic techniques are also ideal for producing accurate statistical data from MD simulations, enabling the use of the prerequisite large simulation cells and long simulation times. *Ab initio* techniques can be used to provide a material study offering a much more detailed insight into the underlying chemistry. However, such techniques are significantly more computationally expensive, and are therefore more appropriate for smaller systems.

2.5.1 Interatomic Potentials

The development of a potential model is the starting point for all atomistic simulation techniques; it uses mathematical terminology to provide a description of the energy of the complex and disordered solids as a function of particle coordinates. The extent to which a potential model represents a system under investigation will directly affect the results obtained from the simulations. The property of the different solid state compounds that is of most importance for the potential model to accurately calculate is the lattice energy (U_{L}). The lattice energy can be defined as; the change in energy upon bringing gaseous ions together from an infinite distance to their equilibrium positions within the solid that they form. By using an application of Hess's Law known, as the Born-Harer cycle, it is possible to determine a specific lattice energy from experiment. The general expression used to calculate the lattice energy (U_{L}) is a series expansion of pairwise, three-body, and increasingly larger body terms, as shown in equation 2.35:

$$U_L = \sum_{ij} V_{ij}\left(r_{ij}\right) + \sum_{ijk} V_{ijk}\left(r_{ijk}\right) + ... \tag{2.35}$$

Within an individual crystal the summation terms given in equation 2.35 refer to all ion pairs (i and j) and all ion trios (ijk). Theoretically equation 2.35 could include terms that represent even larger numbers of ions; however in the majority of computational simulations it is not deemed necessary to include summations that exceed the 'three-body' terms.

The representative potential model for each crystal system is comprised of a number of interatomic equations (empirically derived, parameterised equations) which can be summed to give the lattice energy. The parameters of these interatomic potentials can be adjusted and made appropriate for the chemical factors, such as bond strength, atomic radius and atomic mass, of the crystal structure they represent.

The potential models used for the work within this thesis are based upon the Born model [146] (equation 2.36), which includes predominantly the pairwise (two-body) terms from the lattice energy series expansion. These two-body terms can be further divided into short-range interactions and long-range Coulombic interactions. The short-range interaction terms provide a description for both the attractive and repulsive forces. The attractive forces can be attributed to the presence of dispersive (London) interactions in addition to the covalence in semi-ionic systems, whilst it is the overlap of ion charge clouds that gives rise to the repulsive forces. [125]

$$U_L = \sum_{ij} \frac{q_i q_j}{4\pi\epsilon_0 r_{ij}} + \sum_{ij} \Phi_{ij}\left(r_{ij}\right) + ... \tag{2.36}$$

It is common place to model the short-range interaction terms with simple analytical functions known as interatomic potentials. Perhaps the best known examples of these interatomic potentials are the Buckingham [147] and the Morse [148] potentials (Figure 2.5). Of these functions, the Buckingham potential (Figure 2.5a) has been used to successfully model a variety of solid state ionic materials [149–152]. As can be seen from equation 2.37, the Buckingham can be divided into two component parts. The first of which is an exponentially repulsive term, which represents the repulsion of the electronic charge cloud of the ions, containing the A and ρ parameters. The second component part contains the C parameter and forms an attractive $(\mathrm{C}_{ij}/{r_{ij}}^6)$ term based on van der Waals interactions. [125]

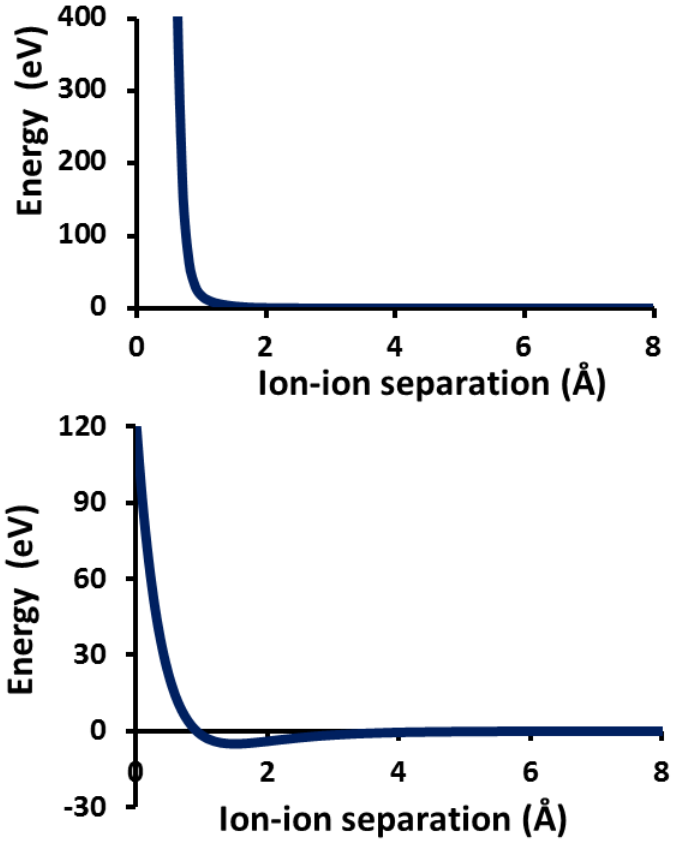

Figure 2.5: Plot of interatomic potentials (a) Buckingham; (b) Morse.

$$\Phi_{ij}(r_{ij}) = A\exp\left(\frac{-r_{ij}}{\rho_{ij}}\right) - \frac{C_{ij}}{r_{ij}^6} \tag{2.37}$$

In the investigations of both the sulphate and hydroxysulphate materials (detailed in chapters 4 and 5), a Morse potential (Figure 2.5b) was used to model the S-O bonds in the SO_4 units and the O-H bonds in the hydroxyl units. The covalent nature of the S-O and O-H bonds, for which the interatomic separations can differ greatly from the equilibrium distance, is accounted for by the Morse potential [148]. Equation 2.38 shows the standard form taken by the Morse potential.

$$\Phi_{ij}(r_{ij}) = D_e\left[\{1-\exp(-a(r_{ij}-r_0))\}^2 - 1\right] \tag{2.38}$$

where the bond dissociation energy (equivalent to the depth of the potential well) is denoted

D_e, the width of the potential well is controlled by the parameter a and the equilibrium bond distance is assigned r_0. It is important to note that in order for the interaction energy to have a value of zero at infinite separation the bond dissociation energy is subtracted. Pairwise interactions within both the SO_4 tetrahedra and O-H hydroxyl units are also Coulomb subtracted in this work, therefore each of the SO_4^{2-} moieties and OH^- units are treated as individual molecular anion units. For the sulphate (SO_4) component, this interatomic model has been successfully formulated to simulate M_2SO_4 (M = Na, K, Rb and Cs) and XSO_4 (X = Sr, Ca, Ba) [153–156]. Similarly for the hydroxyl (OH) component, the attractive Morse potential used to model the O-H interaction has recently been applied successfully to protonic defects and water incorporation in fuel cell materials [157,158].

Further, for the studies of the sulphate and hydroxysulphate materials (detailed in chapters 4 and 5) it has been necessary to include an additional three-body term to each of the respective potential models. This additional three-body term is required to model the SO_4 units and accounts for not only the rigidity of the O-S-O bonds but also their angle-dependent nature. It is centred on the sulphur ion within the SO_4 tetrahedral unit and takes the form of a harmonic angle-bending potential, as shown:

$$\Phi_{ijk} = 0.5K_{ijk}\left(\Theta - \Theta_0\right)^2 \tag{2.39}$$

In equation 2.39 the equilibrium bond angle for a tetrahedron is represented as Θ_0 and the force constant is denoted K. The three-body term acts so that any deviation from the equilibrium bond angle (Θ_0) is penalized by an increase in energy. The implementation of similar three-body terms has proved particularly successful for modelling the PO_4 tetrahedra of $LiFePO_4$, [41,44,45] and the SO_4 tetrahedra of $LiFeSO_4F$ [159].

Ewald Summation

Coulombic interaction terms can be slow to converge, hence their summation can cause problems for the different simulation techniques. [125] The rationale for the slow convergence of this term is that the Coulombic interaction that occurs between the ion pairs (i and j) decays with direct proportionality to the inverse of the inter-ionic separation ($\frac{1}{r_{ij}}$). However, the number of interacting ions increases linearly with the surface area of a sphere, $4\pi r^2$. Hence, whilst we

might expect the Coulombic interaction term to decay, in actual fact the energy density of the interaction increases with inter-ionic separation. Thankfully, there are methods available to counteract this problem; an example of one such method, proposed by Evjen [160], involves the summation of groups of atoms that are neutrally charged. However, for three-dimensional materials the Ewald method [161] is used most regularly to negotiate the problem of slow convergence. This method divides the sum into real and reciprocal space components and requires that the unit cell has a zero dipole moment in addition to being neutrally charged.

In the first series (U_{real}) the point charges of the ions are shielded by Gaussian charge distributions, which are oppositely charged and act to exactly cancel the point charges. The electrostatic interaction encountered by a neighbouring atom comes from the fraction of charge not screened; therefore as the interatomic separation increases this series will rapidly converge to zero. Given the rapid convergence for this series, the screened charges can be summed and calculated in real space. The second series ($U_{Reciprocal}$) is made up of a set of compensating Gaussian charge distributions, which effectively negate the presence of the screening charges in the first series. This therefore leaves only the interactions due to the point charges as the sum of the two series. In this second series, the compensating charge distributions form a smooth periodic function which can be represented, in reciprocal space, as a rapidly convergent Fourier series. Further to this, in order to account for the self interactions that occur between a point charge and its screening charge a correction term (U_{Self}) is also required. The combination of these conditions yields a series that can rapidly converge with a well-defined limit, see Figure 2.6. [131, 162]

2.5.2 Deriving Interatomic Potentials

For atomistic calculations to provide relevant atomic-scale insights, it is necessary that the components that make up the potential models are derived so that observable properties of the material can be reproduced. It is possible to achieve such results through empirical fitting to experimental data and/or materials properties, such as dielectric and elastic constants. Crystal structure information obtained from experimental neutron or x-ray diffraction studies is often the most readily available data with which to make such comparisons. However, the incorporation of other properties including dielectric and elastic constants can be beneficial to

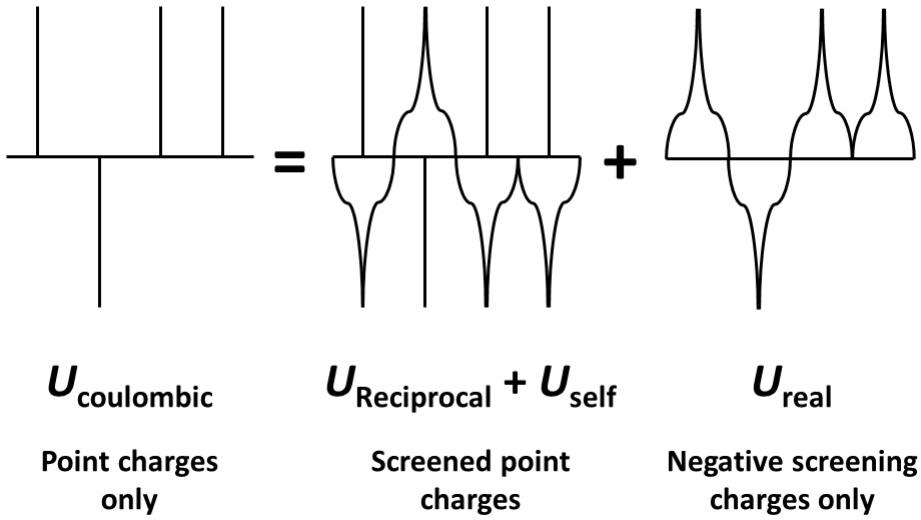

Figure 2.6: Schematic diagram explaining the Ewald summation concept: The sum of a set of point charges ($U_{Coulombic}$) is calculated from a set of screened charges (U_{Real}) in addition to a set of compensating charges which counteract the screening ($U_{Reciprocal}$).

the empirical fitting routine, since such properties provide additional potential energy surface information. It is possible to judge the quality of the fit by calculating the sum of squares (equation 2.40).

$$\sum_{i=1}^{N_{obs}} \omega_i \left(f_i^{obs} - f_i^{calc} \right)^2 \tag{2.40}$$

where the number of observables is denoted N_{obs}, the experimental and calculated values of the observable are assigned as f_i^{obs} and f_i^{calc} respectively and the weighting factor for the given observable is labeled ω_i. The last of these, the weighting factor, may be altered for each observable depending on its reliability and importance to the model. Ideally, the sum of squares would be equal to zero (i.e. a situation whereby simulation exactly matches experiment). However, such situations are highly unlikely except for the most simple of simulations.

The fitting process requires the potential parameters to be adjusted to minimise the sum of squares; the GULP software package achieves this through use of the incorporated Newton-Raphson minimisation algorithm. Effectively the fitting process can be viewed as the reverse of energy minimisation, since the interactions between the ions are adjusted to match the structure, rather than minimising the energy through iteratively modifying the structure.

2.5.3 Modelling Polarisation

For an individual atom it is not usually possible to assume a fixed dipole moment since the polarisability of a species is affected by both the direction and magnitude of the dipole within a crystal. [131] Given that polarisation occurs as a result of distortion of an ions electron charge cloud, which is due to the presence of an applied field, it is therefore absolutely essential to incorporate the effects of polarisation within the potential model. Therefore, the accurate modelling of polarisation effects is of vital importance within defect modelling, since the polarisation produced by the electric field as a result of a charged point defect will affect the lattice relaxation surrounding the defect species.

The simplest model available to describe polarisation is the Point Polarisable Ion (PPI) model. In the PPI model each ion is assigned with a dipole moment (μ). This is the product of the ions point polarisability (α) and the magnitude of the field (E), which enables the polarisability to be calculated by rearranging equation 2.41.

$$\mu = \alpha E \tag{2.41}$$

Unfortunately, when the PPI model is used for solid state ionic materials to calculate the dynamic and dielectric properties, the description it provides of the polarisability is inadequate. This inadequacy can be attributed to the absence of a term in the equation to account for the coupling between the short-range repulsion and the polarisation. This coupling is a key factor that needs to be considered when ions are polarised within solids. Since polarisation can be defined as the distortion that an electric field causes to the valence shell electron distribution of an ion, it will directly impinge on the short-range repulsion, which is the product of the valence shell orbitals of different atoms overlapping. This coupling effectively 'dampens' the effects of polarisation. [125]

The shell model (Figure 2.7), developed by Dick and Overhauser [163], is thought of as being the most successful model to incorporate the key coupling that occurs between the short-range repulsion and the polarisation. [125] It is a simple mechanical model within which each ion is separated into two parts, namely the core and the shell. The core (charge X) effectively accounts for the total mass of the ion, given that it is representative of not only the nucleus but also the inner electrons. In comparison the shell (charge Y) is effectively mass-less as it is

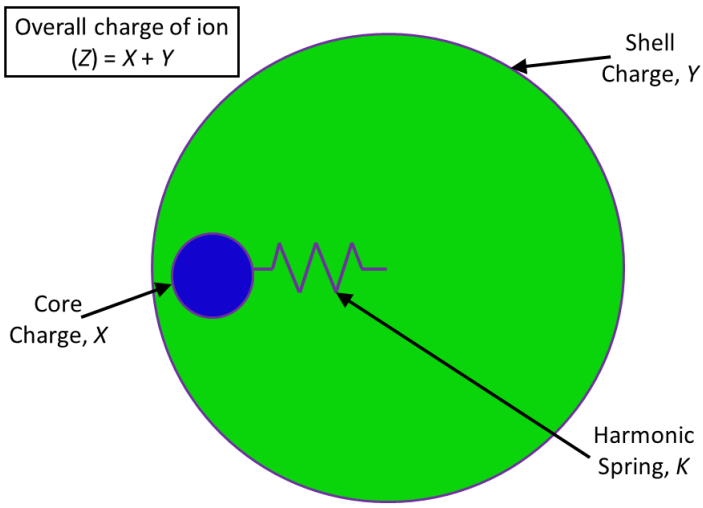

Figure 2.7: A schematic representation of the simple mechanical shell model.

merely representative of the polarisable valence electrons. In certain situations the shell can have a positive charge (often seen with metal cations) and so it would be wrong to explicitly consider the shell model to consist of a positive core and negative shell. Whilst the core and the shell components of the model are coulombically screened from each other, they are connected by a harmonic spring (spring constant k), displacement of the shell from the core gives rise to a dipole moment. [125,131] Hence, for a free-ion, the electronic polarisability can be calculated from equation 2.42 [164]:

$$\alpha = \frac{Y^2}{k} \tag{2.42}$$

2.5.4 Modelling Point Defects

Before outlining the methodology used to model defect species within crystal structures, it is first appropriate to provide an introduction to defect chemistry by highlighting some of the types of defects likely to be encountered. No crystal systems are perfect since, due to entropy, each structure will contain an intrinsic concentration of defects. Of the work contained within this thesis there are four main types of point defect species considered, as shown in the schematic representation provided by Figure 2.8, and detailed below:

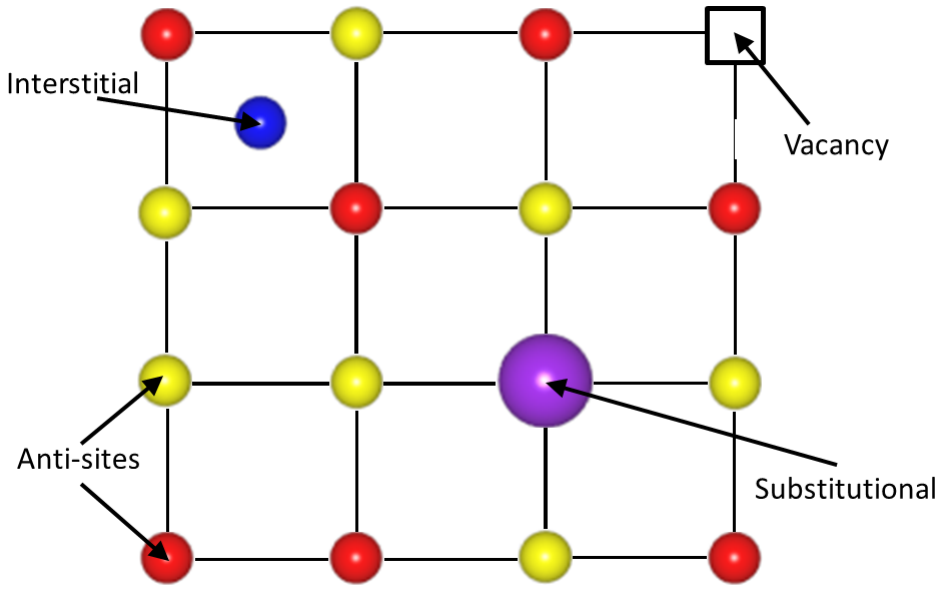

Figure 2.8: Schematic of a two-dimensional cross-section of a crystal lattice showing four different types of point defect.

Vacancy: A vacant lattice site.

Interstitial: The presence of an ion at a site not normally occupied.

Substitutional: A dopant ion on a lattice site.

Anti-site: The exchange of sites for two different lattice ions.

When calculating defect structures and energies, the lattice relaxation effect is an additional feature that has to be accounted for when simulating the addition of a defect to the perfect lattice. Given that the atoms directly surrounding the defect species generally experience an extensive perturbation, it is clear that the relaxation of the lattice has a relatively large effect. Within ionic crystals this perturbation, caused by the defect, is effectively Coulombic since the field of relaxation is relatively long-range. In terms of simulating defects it is very important that all calculations take account of the lattice relaxation caused by the defect species. [131] Lattice relaxtion gives rise to a reduction in the symmetry of the crystal, hence modelling the system as an infinite array of symmetrical unit cells is no longer appropriate.

The Mott-Littleton approximation [165] (Figure 2.9) is a method of defect modelling that attempts to account for the lattice relaxation effect. It requires that the crystal lattice is

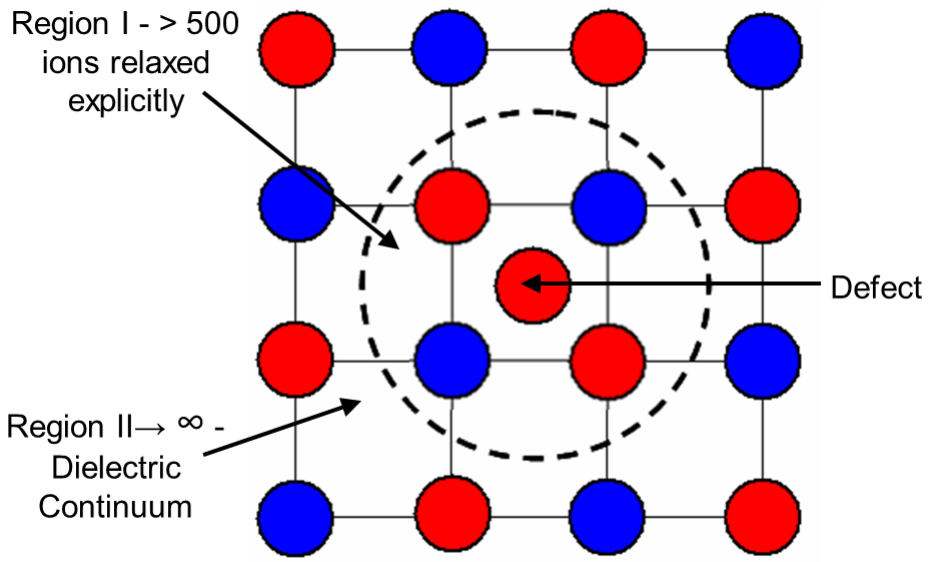

Figure 2.9: A schematic representation of the Mott-Littleton 'two-region' strategy for simulation of defects. The red sphere at the centre of region I represents the defect. It is important to note that region II extends to infinity. [165]

divided into two separate regions. In the spherical inner region (region I) the ions are surrounding the defect, hence the lattice relaxation effect within this region is very strong and all ions are relaxed explicitly. Consequently, it is vital that each ion is atomistically modelled by the appropriate interatomic potentials. In contrast, the effect of the lattice relaxation caused by the defect upon the ions in the more distant areas of the crystal can be described as negligible. The outer-region (region II), which extends to infinite distance, is further split into two regions, namely IIa and IIb. The ions in the outer-most region (IIb) are modelled by approximate quasi-continuum methods, hence the response to the defect is effectively dielectric (a change in polarisation of the ions but no displacement). [125, 166] In region IIa the ions are modelled explicity like those in region I. Whilst the relaxation in region IIa is technically a result of all the ions within region I, in reality an approximation is used which allows the relaxation in region IIa to be modelled as a result of only the charge of the defect. Therefore, region IIa can be described as an intermediate region between regions I and IIb, for which the modelling of the lattice relaxation is very different.

In order for this approach to be valid it is important that the defect energy has converged significantly with respect to the region IIb radius, so that the likelihood of lattice relaxation

occurring within region IIb is completely removed. To ensure the validity of the model it has been suggested that both the radius of region I, and the difference between region I and region IIb should exceed the value of the Buckingham potential cutoff radius. Due to the mainly long-range Coulombic effect of the defect, such an approach may still not provide a completely adequate model of the lattice relaxation. Therefore, for such calculations, it is always appropriate to check if increasing each of the region sizes gives rise to a noticeable change with regard to the values of the defect energies.

2.5.5 Ion Migration

Ion migration within inorganic crystal structures occurs through a variety of mechanisms involving defect species. As previously discussed, the mobility of the alkali ions (sodium and lithium) is an essential requirement for the successful operation of battery cells based on both lithium-ion and sodium-ion technology. Whilst ions can migrate through crystals via a number of different mechanisms, the most common are the vacancy hopping and interstitial-type mechanisms shown respectively in Figures 2.10 and 2.11.

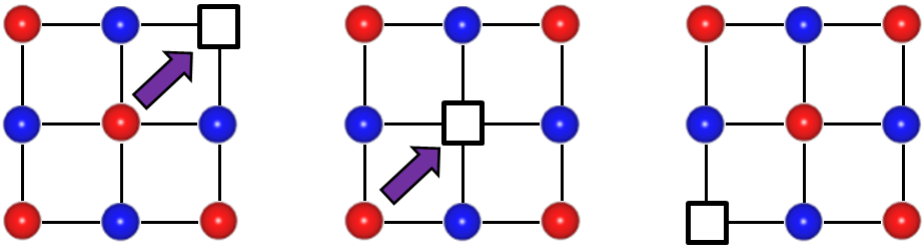

Figure 2.10: Schematic of a two-dimensional cross-section of a crystal lattice showing the vacancy hopping mechanism. The repeating exchange of a lattice ion with a neighbouring vacancy enables ion migration to occur.

The vacancy hopping mechanism (Figure 2.10) involves the exchange of an ion with a neighbouring vacancy, this results in net ion migration in the opposite direction to the vacancy. The interstitial-type mechanisms (Figure 2.11) involve interstitial-ion migration through the crystal lattice via either exchange with lattice ions or direct migration between neighbouring interstitial sites.

When using static lattice methods to model ion migration it is common practice for a series of calculations to be created, each of which provide a 'snapshot' of the movement of

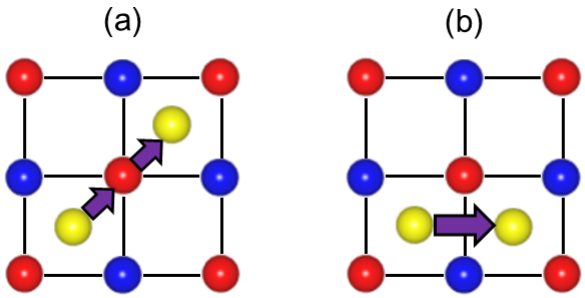

Figure 2.11: Schematic of a two-dimensional cross-section of a crystal lattice showing the interstitial-type hopping mechanism. (a) The interstitialcy mechanism: an interstitial ion moves onto the site occupied by a lattice ion, forcing that lattice ion off its site and into a nearby interstitial site. (b) Direct interstitial migration: the migration of an interstitial ion directly into a neighbouring interstitial site.

the migrating ions between the lattice sites. An energy profile of the migration mechanism is created using the energies of each respective snapshot; the highest point represents the first-order transition state, which corresponds to the activation energy of migration. Constrained minimisation and nudged elastic band (NEB) are the two types of transition state minimisation techniques (see Section 2.2.4) which have been employed within this thesis in order to find ion-migration barriers. It is also possible to use ion trajectory data from MD calculations to gain information regarding the mechanisms and energetics of ion migration, as detailed in Section 2.4.4.

2.6 Electronic Structure Techniques

Insights into various ground-state properties for a range of systems can be provided by electronic structure calculations; often calculations based on empirical methods will not allow for such structure-property insights. In essence the underlying advantage of electronic structure calculations is the enhanced level of knowledge and understanding that can be gained. Simulations based on both electronic structure and atomistic (potentials-based) methods enable the total energy of a system to be calculated. However, unlike electronic structure techniques, atomistic simulation will not allow for the investigation of certain system properties, such as: band structure, orbital occupancies, charge distribution and bonding.

For the work contained within chapters 4 and 5 of this thesis, electronic structure meth-

ods have been used to supplement results obtained via atomistic simulations. The primary structure-property relationship of interest for this work, that can be investigated using electronic structure methods, will be voltage calculations for the novel positive electrode materials studied. In order to provide such insight Density Functional Theory (DFT) will be employed as the electronic structure method.

2.6.1 Density Functional Theory

Density Functional Theory (DFT) is an *ab initio* electronic structure technique which is used to investigate and probe the structure-property relationships of many-electron systems. Compared to other electronic structure methods DFT is less expensive computationally, and as such it is a technique that is particularly popular with both condensed matter physicists and computational chemists.

Within the recent past, much of the development of DFT is attributed to Walter Kohn; the recipient of the 1998 Nobel Prize in Chemistry for the development of Density Functional Theory [167]. However, it should be noted that some of the more basic elements of modern DFT can be dated back to work from the 1920's and the Thomas-Fermi model [168, 169], to which Dirac [170] added a local approximation for exchange. Although due to the substantial approximations involved with this initial work it was regarded as too inaccurate for the calculation of electronic structure. Therefore, it is in the 1960's that many associate the first major breakthroughs in the development of modern DFT, via the Hohenberg-Kohn theorems [171] and the work of Kohn and Sham [172]. The culmination of which provided a practical framework for solving DFT problems.

The aim of all quantum mechanical and electronic structure method calculations is to find a solution to the Schrödinger equation [173]. The Schrödinger equation is therefore vitally important to such methods since, knowing the wave-function of the system will allow for all physical properties of that system to be calculated. All the information about the positions and spins of the particles that make up the system are contained within the wave-function (ψ). Whilst the time-independent Schrödinger equation may appear relatively simplistic (equation 2.43) it is anything but, and generating a solution is an extremely complex and involved process.

$$\mathscr{H}\psi = E_{Total}\psi \tag{2.43}$$

Within the Schrödinger equation the full Hamiltonian operator ($\mathscr{H}$) describes a set of mathematical operations, which when performed on the wave-function (ψ) will describe a system related property. For the example of the time-independent Schrödinger equation shown (equation 2.43), application of the full Hamiltonian on the wave-function will return a value for the total energy of the system (E_{Total}). The full Hamiltonian operator ($\mathscr{H}$) can be described as shown in equations 2.44 and 2.45.

$$\mathscr{H} = T + T_n + V_{int} + V_{nn} + V_{ext} \tag{2.44}$$

where the first two terms of equation 2.44 are the kinetic energy of the electrons (T) and nuclei (T_n) respectively. Whilst the remaining three terms (V_{int}, V_{nn} and V_{ext}) can be summed to give the potential energy. The potential energy from the inter-electron (electron-electron) repulsions is denoted V_{int}, that from the nuclear-nuclear repulsions is labeled V_{nn} and the external potential, equivalent to the electron-nuclear attraction, as seen by the electrons is given as V_{ext}. It is important to note the omission of the $\frac{1}{4\pi\epsilon_0}$ factor for reasons of simplicity, and that the summations are extended over all the electrons and nuclei of the system.

$$\mathscr{H} = -\frac{h^2}{2m_e}\sum_i \nabla_i^2 - \sum_I \frac{h^2}{2M_I}\nabla_I^2 + \frac{1}{2}\sum_{i\neq j}\frac{e^2}{|r_i - r_j|} + \frac{1}{2}\sum_{I\neq J}\frac{Z_I Z_J \cdot e^2}{|R_I - R_J|} - \sum_{i,I}\frac{Z_I \cdot e}{|r_I - R_I|} \tag{2.45}$$

where the mass and position of the electron (i) are denoted m_e and r_i respectively, and the mass and position of nucleus (I) with a charge (Z_I) are labeled as M_I and R_I respectively. Therefore, from the above equations (2.44 and 2.45) we can see that evaluating the full Hamiltonian for many-body systems will be a complex process, not least because of the large number of inter-dependencies that require consideration. In practice, the problem of solving these highly complex electronic structure calculations is made tractable by a series of approximations. The first of these is the Born-Oppenheimer approximation [174], which allows the nuclear and electron motions to be decoupled enabling the electrons to move about a fixed nuclear configuration. The justification for the Born-Oppenheimer approximation is that the

nuclear masses are in significant excess of the mass of an electron; consequently the speed with which a nucleus moves will be negligible compared to that of an electron. Therefore adopting the Born-Oppenheimer approximation; equations 2.44 and 2.45 can be rewritten in terms of the electronic Hamiltonian ($\mathscr{H}_{elec}$).

$$\mathscr{H}_{elec} = T + V_{int} + V_{ext} \tag{2.46}$$

$$\mathscr{H}_{elec} = -\frac{h^2}{2m_e}\sum_i \nabla_i^2 + \frac{1}{2}\sum_{i\neq j}\frac{e^2}{|r_i - r_j|} - \sum_{i,I}\frac{Z_I \cdot e}{|r_I - R_I|} \tag{2.47}$$

$$\mathscr{H}_{elec} = -\frac{h^2}{2m_e}\sum_i \nabla_i^2 + \frac{1}{2}\sum_{i\neq j}\frac{e^2}{|r_i - r_j|} + \sum_i V_{ext}(r_i) \tag{2.48}$$

Through the Born-Oppenheimer approximation, and consequential simplification of the full Hamiltonian ($\mathscr{H}$) to the electronic Hamiltonian ($\mathscr{H}_{elec}$), the complexity of solving the Schrödinger equation for many body systems is reduced to a tractable problem. The many-body wave-function (ψ) is now dependent only upon the spins and positions of the electrons within the system; the nuclear positions only figure as a component of the external potential (V_{ext}).

2.6.2 Hohenberg-Kohn Theorems

For a given system the density functional theory (DFT) approach to solving the Schrödinger equation, now simplified by the Born-Oppenheimer approximation, is to calculate the ground-state electron density for that system. Using the ground-state electron density it is then possible to find other ground-state energy properties for the system. The validity of this approach was provided by the two key theorems of Hohenberg and Kohn, which were formalised and proven within their landmark paper published in 1964 [171]. These theorems are:

1: The three dimensional electron density of a many electron system uniquely determines the ground state properties of that system.

2: The energy of a system can be defined as a functional of the electron density, with the minimum of the energy functional corresponding to the ground-state electron density.

Therefore, by defining the energy functional for the system and finding the minimum, the ground-state electron density of the system can be determined, from which it is possible to derive other ground-state properties. Within their seminal paper [171], the Hohenberg-Kohn Theorems define the energy functional according to equation 2.49.

$$E\left[\rho(r)\right] = \int V_{ext}(r)\rho(r)d(r) + F\left[\rho(r)\right] \tag{2.49}$$

where the first term of equation 2.49, describes the interaction of the electrons with the external potential (V_{ext}). Additionally, due to the use of the Born-Oppenheimer approximation, the interactions of the nuclei with the electrons of the system are also encapsulated within the V_{ext} term. Further to this the three dimensional electron density is denoted $\rho(r)$, with the summation of the kinetic energy of the electrons and the inter-electron interactions described by the $F\left[\rho(r)\right]$ term. However, given the unknown nature of the $F\left[\rho(r)\right]$ term, we still do not have all the information necessary to calculate the ground-state energy of a many electron system.

2.6.3 Kohn-Sham Equations

Whilst the Hohenberg-Kohn theorems laid the foundations for the development of modern DFT as we know it, their findings did not provide a means in order to actually solve the Schrödinger equation. However, subsequent work by Kohn and Sham, published in 1965 [172], did introduce a method for finding solutions to DFT problems via a series of equations that became known as the Kohn-Sham equations. Their approach assumed that for a given system consisting of a set of interacting electrons with electron density $\rho(r)$, a theoretically equivalent system with the same $\rho(r)$ could be created for a set of non-interacting electrons. Based on this assumption Kohn and Sham were able to separate the unknown energy functional term from the Hohenberg-Kohn theorem into a number of component terms according to equation 2.50.

$$F\left[\rho(r)\right] = E_{ke}\left[\rho(r)\right] + E_H\left[\rho(r)\right] + E_{xc}\left[\rho(r)\right] \tag{2.50}$$

where the kinetic energy of the electrons is denoted $E_{ke}\left[\rho(r)\right]$ and the Hartree term representing the Coulombic energy of the electron-electron interaction is given as $E_H\left[\rho(r)\right]$. The remaining $E_{xc}\left[\rho(r)\right]$ term, which symbolizes the component of the energy functional from the

exchange-correlation term, is of vital importance and approximations to represent this are discussed later. As the name suggests the $E_{xc}[\rho(r)]$ term accounts for the contributions, within the interacting system, caused by the exchange and correlation of electrons. However, in addition to this the exchange-correlation term also defines the energy difference between the real interacting system of electrons and the hypothetical non-interacting system. In many ways, the exchange-correlation term can be viewed as collecting all the unknowns of the problem into a single contribution for which an approximation is required.

It is crucial to remember that when referring to equation 2.50 the $E_{ke}[\rho(r)]$ term describes the energy of a set of non-interacting electrons, for which the electron density ($\rho(r)$) is the same as the system under study. Also it is important to note that the Hartree term (equation 2.51) does not account for the correlation of electron motions, and instead the interacting electrons are defined by the summation of classical pairwise interactions between charge densities.

$$E_H[\rho(r)] = \frac{1}{2}\int\int \frac{\rho(r_1)\rho(r_2)}{[r_1 - r_2]} dr_1 dr_2 \tag{2.51}$$

In order to find a stationary solution to the Schrödinger equation it is necessary to combine equations 2.49 and 2.50 before minimising with respect to $\rho(r)$, which results in the Schrödinger-like Kohn-Sham equation, as shown below:

$$\left[-\frac{h^2}{2m_e}\nabla^2 + V_{eff}(r)\right]\psi_i(r) = \epsilon_i\psi_i(r) \tag{2.52}$$

where the orbital energies are denoted ϵ_i, the Kohn-Sham orbitals containing the non-interacting electrons are given as $\psi_i(r)$ and the effective potential for the system is represented by the V_{eff} term. This final effective potential term (V_{eff}) can be further separated according to equation 2.53:

$$V_{eff}(r) = V_{ext}(r) + \int \frac{\rho(r')}{[r - r']} dr' + V_{xc}(r) \tag{2.53}$$

where the $V_{xc}(r)$ term is the exchange-corrleation potential, which can be related to exchange-correlation energy functional ($E_{xc}[\rho(r)]$) according to equation 2.54:

$$V_{xc}(r) = \left(\frac{\delta E_{xc}[\rho(r)]}{\delta\rho(r)}\right) \tag{2.54}$$

Using the combination of Hohenberg-Kohn Theorems and the Kohn-Sham equation allows DFT to provide a method for solving the Schrödinger equation for a given system. The iterative-process to finding a solution begins by making an initial 'best guess' of the electron density ($\rho(r)$), which is used within equation 2.53 in order to generate an effective potential (V_{eff}) term. By inputting this effective potential term into equation 2.52 a set of Kohn-Sham orbitals are generated for the system. This allows an improved estimate of the electron density ($\rho(r)$) to be calculated based on equation 2.55.

$$\rho(r) = \sum_{i}^{N} |\psi_i(r_i)|^2 \tag{2.55}$$

The process described above is then repeated using the improved estimate of the electron density ($\rho(r)$) with the iterative cycle continuing until convergence upon a single value for the electron density. The converged electron density, generated from the self-consistent field method described, corresponds to the ground-state electron density for the system according to the second Hohenberg-Kohn theorem [171].

2.6.4 Approximate Exchange-Correlation Functionals

Within the Kohn-Sham framework of DFT the major uncertainty is the exact nature of the exchange-correlation energy functional ($E_{xc}[\rho(r)]$) term which, for the vast majority of systems, is unknown. A value for this term has been calculated for a homogeneous electron gas, for which the exchange energy is known exactly and Monte Carlo methods are used to accurately calculate the correlation energy. However, for almost every other system the nature of exchange-correlation energy functional ($E_{xc}[\rho(r)]$) remains unknown, thus an approximation is required.

For current DFT calculations the approximation of this term is considered to be a significant source of error. Therefore, the accuracy of the whole DFT technique relies upon finding a good approximation of this quantity. A wide variety of approaches have been taken in order to overcome this problem, however opinion is still mixed regarding whether the best approximation for this term is achieved semi-empirically or purely theoretically. Most functional approximations for the $E_{xc}[\rho(r)]$ term are currently based on the Local Density Approximation (LDA) or the Generalised Gradient Approximation (GGA), which is an extension of the

LDA.

Local Density Approximation

First suggest by Kohn and Sham, the Local Density Approximation (LDA) is regarded as the simplest approximation for the exchange-correlation energy functional ($E_{xc}[\rho(r)]$) term, and as such it has proved a popular method. Using the LDA the exchange-correlation functional is represented as:

$$E_{xc}^{LDA}[\rho] = \int \rho(r)\varepsilon_{xc}^{hom}(\rho(r))dr \tag{2.56}$$

for which the assumption of the LDA is that the exchange-correlation energy per electron, located at point r, is equivalent to the homogeneous electron gas with density $\rho(r)$. Using the LDA the reproduction of properties such as bond lengths, crystal structure and phonon frequencies is generally found to be of high accuracy for a range of materials. Indeed even for those inhomogeneous systems, for which the electron density does not resemble that of a homogeneous electron gas, the LDA is found to work well. Despite consistently underestimating the correlation energy and overestimating the exchange energy, the success of the LDA can partly be attributed to the fact that some of these errors involved in the calculation of $E_{xc}^{LDA}[\rho]$ are systematically canceled. Although some of the errors within the calculation cancel each other out, there are several remaining problems with the LDA. Notable problems experienced with LDA calculations include; underestimating the band gaps of materials, overestimating binding energies and incorrect predictions for the structures of electronic ground-states.

Generalised Gradient Approximation

For real systems there are always some variations in the electron density with respect to the position. Therefore, the homogeneous electron gas concept used with the LDA can be considered to be somewhat flawed. There are some approximations for the exchange-correlation energy functional ($E_{xc}[\rho(r)]$) term that attempt to include the variation of the electron density with position. These semi-local functionals consider the local electron density ($\rho(r)$) at position r, however unlike the LDA such functionals also account for variations of $\rho(r)$ and are therefore known as gradient-correlated. The Generalised Gradient Approximation (GGA) functional

is regarded as the simplest gradient-correlated functional, and can be used to calculate the exchange-correlation energy functional term according to equation 2.57:

$$E_{xc}^{GGA}[\rho] = \int \rho(r)\varepsilon_{xc}^{GGA}(\rho(r), \nabla\rho(r))dr \tag{2.57}$$

Whilst within the LDA there is only one 'correct form' of ϵ_{xc} (i.e., ϵ_{xc}^{hom}), and as such the LDA can only take one form, within the GGA there are many potential alternative parameterisations of ϵ_{xc}. Therefore, many different types of GGA functional exist, however for the calculations within this thesis a functional based on the work of Perdew, Burke and Ernzerhof (PBE) [175] is incorporated. Further to this, some of the more well known alternatives to the PBE form of GGA are provided through the work of Perdew and Wang (PW91) [176] and Wu and Cohen (WC) [177].

In general for non-metallic systems, including inorganic oxides, GGA based calculations tend to reproduce the key properties of real systems, such as lattice parameters, with greater accuracy than equivalent LDA based calculations. The overestimated binding energies observed in the LDA are corrected for within the GGA. Additionally the GGA also reproduces band gaps of materials with improved accuracy compared to the LDA, although it still generally leads to an underestimation of band-gap energies.

Hubbard Coefficients: LDA+U (GGA+U)

Materials containing strongly correlated electron systems, such as those involving atoms with partially filled *d*- and *f*-orbitals, show enhanced sensitivity to the description of the exchange-correlation functional employed. This is of particular importance to the positive electrode materials considered within this thesis, since they all contain transition metal elements and will therefore have partially filled *d*-orbitals. Application of the LDA to compounds containing transition metals, renders such systems as partially filled *d*-bands with metallic-type electronic structures with itinerant *d* electrons. Such results compare unfavourably with transition-metal and rare-earth compounds observed experimentally, for which localized *d* and *f* electrons and distinct separate occupied and unoccupied *d* electron bands are found [178].

Within the LDA+U (and/or GGA+U) technique [179, 180] the strong on-site correlation of the *d* and *f* electrons is accounted for by altering the exchange correlation functional. The

standard LDA is used to treat the s and p electrons of the compound, whilst the d and f electrons are treated separately with their Coulombic interaction accounted for by a Hartree-Fock-type (mean-field) approximation [181, 182]. The U parameter (Hubbard Coefficient) controls the strength of the correction made to the exchange correlation functional, directly affecting the energy gap between the unoccupied and occupied bands.

2.6.5 Applying DFT to Solids

Finding a solution to the Schrödinger equation so that certain properties of a given material can be calculated could be a highly complex and onerous task; particularly where solid state systems are concerned. Since for such solid state systems we normally consider the given system to contain an infinite number of ions and electrons, which would require the wave-function to be determined for all electrons. Further to which given that the wave-function of each electron extends over the entire lattice, in order to describe it an infinite number of basis functions would be needed. Fortunately, the periodic nature of solid state systems means that the inherent symmetry (and more specifically periodic boundary conditions referred to in Section 2.3) reduces the requirement to consider such infinite quantities making the problem solvable.

The Reciprocal Lattice - k-space

Convention dictates that when considering a crystal lattice we normally think of how it is defined in real space, however the use of computational techniques may require the reciprocal lattice to be defined within k-space. Within k-space (also known as reciprocal space), the real space lattice vectors a, b and c are related to the k-space reciprocal lattice vectors a^*, b^* and c^* by the relationship shown in equation 2.58.

$$a^* = 2\pi \frac{b \times c}{a \cdot b \times c} \; ; \; b^* = 2\pi \frac{a \times c}{b \cdot a \times c} \; ; \; c^* = 2\pi \frac{a \times b}{c \cdot a \times b} \tag{2.58}$$

In just the same way as an infinite crystal lattice within real space can be developed by defining a unit cell, it is similarly possible for a primitive cell to be defined within k-space so that the infinite reciprocal lattice is reproduced. The Brillouin Zone is the name given to such a k-space primitive cell. The concept of Brillouin Zone is of vital importance for the description

of periodic systems because, within its volume, a complete description of the wave-function can be provided.

Blochl's Theorem

Blochl's theorem [183] states that the wave-function of an electron i within a periodic field may be written as the product of two separate components; a wave-like term and a term with the same periodicity as the unit cell. A description of the wave-like term is provided by equation 2.59:

$$\psi_i(r) = e^{ik\cdot r} f_i(r) \tag{2.59}$$

where the wave-vector in the Brillouin Zone is denoted k, which controls the frequency and direction of the wave-like term.

It is possible to construct the cell-periodicity term of the wave-function through combination of a basis set of discrete planewaves ($e^{iG\cdot r}$), with all translations to symmetrically identical lattice points represented by the wave-vectors (G).

$$f_i(r) = \sum_G c_{i,G} e^{iG\cdot r} \tag{2.60}$$

Following on from this, the wave-function of each electron (i) can subsequently be written as a summation of planewaves, according to equation 2.61:

$$\psi_i(r) = \sum_G c_{i,k+G} e^{i(k+G\cdot r)} \tag{2.61}$$

where the solution is defined by the coefficients $c_{i,k+G}$.

Planewaves

When a planewaves basis set is being utilised within a simulation it is possible to reduce the complexity of the calculation through the use of two approximations. First, planewaves with a larger $|G|$ contribute less to the wave-function since they have increased kinetic energy; therefore an energy cut-off can be imposed above which the planewaves are not evaluated. This is possible because, above this cut-off value, the contribution of the planewaves to the wave-

function is inconsequential. The second approximation relates to the sampling of reciprocal-space (k-space). Since ψ is a continuous function of k, small changes to k will have a muted effect on ψ, hence instead of providing a complete description of k-space by sampling infinite k-points, an adequate description will be provided via a finite set of k-points [184].

In order to correctly determine the band structure and density of states for a material it is crucial to choose an appropriate set of k-points. The Monkhorst and Pack selection scheme [185] samples the Brillouin Zone by defining an evenly spaced k-point mesh. The advantage of the Monkhorst-Pack approach is that many of the k-points within the grid are symmetry equivalent. Therefore, the use of excess computational expense can be avoided since it is only necessary to calculate the wave-function at symmetry-nonequivalent (unique) k-points.

For practical applications, it is necessary to test the convergence of both approximations. Given that it is not possible to converge the wave-function, the properties of interest for the material are used for convergence testing. By conducting calculations using a range of different values for the energy cut-off and the density of the k-point grid it is possible to test, and evaluate, the convergence of the properties of interest. The same levels of accuracy are not required for all properties of a material; for instance the total energy of a system tends to converge relatively quickly. Therefore, if such a property is the only property of interest it is reasonable to define coarser k-point grids and use lower cut-off values in order to reduce computational expense. However, often very precise calculations offering high levels of accuracy are required to achieve convergence for certain properties of materials, such as the positions of energy levels. Intuitively such calculations can be expected to be computationally expensive.

Pseudopotentials

Near the nuclei of an atom or an ion the potential, and hence the electron wave-function, varies significantly. Providing a representation of the fine spatial detail associated with the electron wave-function at small distances from the nuclei would require large numbers of planewaves. The large numbers of planewaves would be likely to both reduce the calculation speed and increase the computational cost. However, for a given system the core electrons are generally unaffected by changes in the atomic environment, and therefore they can be viewed

as effectively fixed. Using this behaviour, a common approximation involves the removal of the core electrons from the system, with a smooth function (pseudopotential) acting as the core potential. The pseudopotential can be reproduced via a reduced set of planewaves lowering the computational expense. However, for this approximation to be valid beyond a certain cut-off radius from the nuclei the pseudopotential must take the same form as the original core potential. The limitation of this approximation is that the generated wave-function only provides an adequate representation of the valence region of the system, therefore the core electrons can no longer be considered.

The 'softness' of a pseudopotential is used to describe both the size of the cut-off radius from the nucleus and the smoothness of the function. Smoother pseudopotentials can be described using less basis functions. However, it is necessary to avoid having very soft pseudopotentials as larger cut-off radii provide a less accurate description of the atom and result in a less transferable pseudopotential. An ideal pseudopotential is one that will accurately reproduce the valence properties for the atom in question. In general it has been found that the most effective pseudopotentials have been calculated using *ab initio* techniques rather than those defined empirically.

For the work in this thesis the Projector Augmented Wave (PAW) method [183] has been used. The PAW approach embodies a particularly smooth pseudopotential in combination with local auxiliary functions allowing it to represent the full all-electron wave-function.

2.7 Calculation Information

2.7.1 Equipment

In order to complete the calculations necessary for the work presented within this thesis several different computer systems were used. Each individual type of calculation will have different system requirements that are dependant upon the computational expense of the calculation. Since GULP is optimised for single core processing, calculations using this software package could be performed on a standard desktop system. Example desktop specification: Quad-Core i3 3.1 GHz and 4GB RAM.

However, in general for the majority of GULP based calculations servers employing a CONDOR high throughput computing system were utilised. Such a system enables a vast

number of calculations to be simultaneously submitted; in each case as soon as a single core becomes available it will be assigned to one of the submitted calculations. Example desktop specification: 2 x Quad-Core AMD Opteron 2360 SE 2.5 GHz and 32GB RAM.

For the more computationally expensive MD and DFT based calculations the calculation time has been reduced by use of parallelisation. For such calculations the overall task is separated into smaller component parts each of which is processed in parallel. In order to maximise efficiency benchmarking is essential since the performance gains for parallelisation are reduced significantly when the inter-process communications start to outweigh the computational load. MD and DFT calculations using the DL_POLY and VASP software packages respectively were performed using the UK's high performance computing service, HECToR (High-End Computing Terascale Resource). For such calculations an appropriate number of cores ranging between 128 and 312 were assigned.

2.7.2 Calculation Speed

For a standard geometry optimisation calculation the time taken for completion will vary depending upon a number of factors including: size of simulation cell, structural complexity and symmetry. For the crystal structures presented herein optimisation typically did not exceed 5 seconds. However, for NEB calculations using GULP (version 4.0) involving the use of larger (4×4×4) supercells optimisation could take anything between 25 minutes and an hour.

Defect calculations involving the Mott-Littleton methodology were found to be dependent on the respective sizes of both region I and region II in addition to the factors described above. Defect calculations deploying the standard 12 Å and 24 Å regions I and II sizes respectively were typically found to complete within a time-frame of between 15 and 45 minutes.

MD calculations using DL_POLY (version 2.2) to simulate 1 ns of atomic motion for the $Li_2Fe(SO_4)_2$ system consisting of 8×4×4 unit cells (3328 atoms), were completed on HECToR within the available 12 hour wall time.

Finally, each of the DFT calculations using VASP (version 5.4) to study the structural properties of both $Li_2M(SO_4)_2$ (24 atoms) and the $LiFeSO_4OH$ polymorphs (36 atoms) took between 2 and 3 hours to complete on HECToR utilising 10 nodes.

2.7.3 Calculation Error

For the atomistic simulation calculations it is necessary to note that the description of the forces, acting between the atoms within a system, are represented by interatomic potentials. Therefore, for the various defect, migration and surface properties examined calculations utilising such atomistic methods will not produce exact energies. However, providing a reliable potential model is used, the general trend of the results produced for each system should be correct. The reliability of the potential models used within our work are assessed by the accuracy with which it replicates experimental observables including the crystal structure. To this end, we have attempted to ensure that precise defect energy values are calculated by testing their convergence with increased Mott-Littleton region sizes.

Since *ab initio* techniques treat the electronic structure explicity they are ideal for modelling dynamic systems for which atomistic methods may fall short. However, it is worth noting that explicit relaxation of the large number of lattice ions around defect species is not easily treated by DFT-based computational methods. Therefore, such calculations are limited to smaller systems enabling valuable information on electronic structure and redox potentials to be determined. For, such techniques it is necessary for the basis set to be converged against the stress, since the stress is more sensitive to an under-converged basis set than the forces. In order to adequately converge the stress appropriate cutoff energies and k-point mesh densities were determined; for example, in the study of $Li_2Fe(SO_4)_2$ a cutoff energy of 750 eV with a k-point mesh density of at least 0.04 $Å^{-1}$ was needed to adequately converge the stress.

Chapter 3

Pyrophosphate Cathodes $Li_2FeP_2O_7$, $Na_2FeP_2O_7$ and $Na_2MnP_2O_7$: Structural and Ion Diffusion Properties

3.1 Background

Recent studies have highlighted the pyrophosphate, $Li_2FeP_2O_7$ [67–69] and related compounds [70–73] as materials that could provide an avenue for important electrode research. $Li_2FeP_2O_7$ shows ease of synthesis via a conventional solid-state reaction coupled with a high voltage of 3.5 V vs. Li/Li^+ without nano-sizing or carbon coating [67]. This voltage is the highest of the known Fe-based phosphate cathodes.

Li-ion batteries have dominated the portable energy storage market during the course of the past two decades [4, 6, 18, 43, 78–80] However, despite the widespread use of Li-ion cells, batteries based on alternative carrier ions, such as sodium ions, could be more suitable for large-scale energy storage systems as introduced in **Chapter 1**. The relative abundance and low cost associated with Na-ion batteries make them an attractive option for electricity grid storage. For applications in which gravimetric energy density is not a concern, Na-ion batteries are a highly favourable alternative [81, 82].

Motivated by the advantageous properties of Na-ion batteries and the promising peformance of $Li_2FeP_2O_7$, attempts were made to synthesise $Na_2FeP_2O_7$ [97–99]. Additionally, efforts were made to synthesise other Na-analogues using alternative transition-metal active redox species including a new polymorph of $Na_2MnP_2O_7$ (β-$Na_2MnP_2O_7$) [100, 101].

$Na_2FeP_2O_7$ was prepared by a conventional one-step solid-state synthesis by Yamada et al. [97]. Without further optimisation, the as-synthesised $Na_2FeP_2O_7$ cathode was found to be electrochemically active, delivering a reversible capacity of 82 mA h g^{-1} with an operating voltage around 3 V (vs. Na/Na^+). Due to its theoretical capacity of $\sim$100 mA h g^{-1} and good rate capability $Na_2FeP_2O_7$ is widely considered to be a highly promising new positive electrode material. In terms of crystal structure, the change of alkali ions from Li to Na gives rise to different crystal frameworks: while $Li_2FeP_2O_7$ adopts the monoclinic ($P2_1/c$) structure [67], $Na_2FeP_2O_7$ adopts the triclinic ($P\bar{1}$) structure [98].

Further to this, β-$Na_2MnP_2O_7$ [100] has also been considered as a potential pyrophosphate cathode material for sodium-ion batteries, and was found to show similar (if not slightly improved) electrochemical performance to $Na_2FeP_2O_7$. $Na_2MnP_2O_7$ displayed a discharge capacity close to 80 mA h g^{-1} (at 25 ^{o}C) with a voltage located at 3.6 V, the highest Mn^{3+}/Mn^{2+} redox potential amongst all Mn-based cathodes. The β-$Na_2MnP_2O_7$ polymorph crystallise in the triclinic ($P1$) space group [100], isostructural to the rose-polymorph of $Na_2CoP_2O_7$ [102].

However, the fundamental basis for the performance of these pyrophosphate materials is poorly understood, often preventing further optimisation. To understand the factors influencing the electrochemical behaviour of $Li_2FeP_2O_7$, $Na_2FeP_2O_7$ and $Na_2MnP_2O_7$ it is clear that greater knowledge of the crystal structures and underlying defect and transport properties is needed on the atomic scale. In particular, there has been little attempt so far to elucidate the diffusion pathways or activation energies that govern alkali-ion transport within these pyrophosphate structures, which are important factors for charge/discharge rates and high power.

The present study uses advanced simulation techniques to investigate these important issues for the complex crystal structures of these pyrophosphate matarials.

3.2 Results and Discussion

3.2.1 Crystal Structure and Potentials

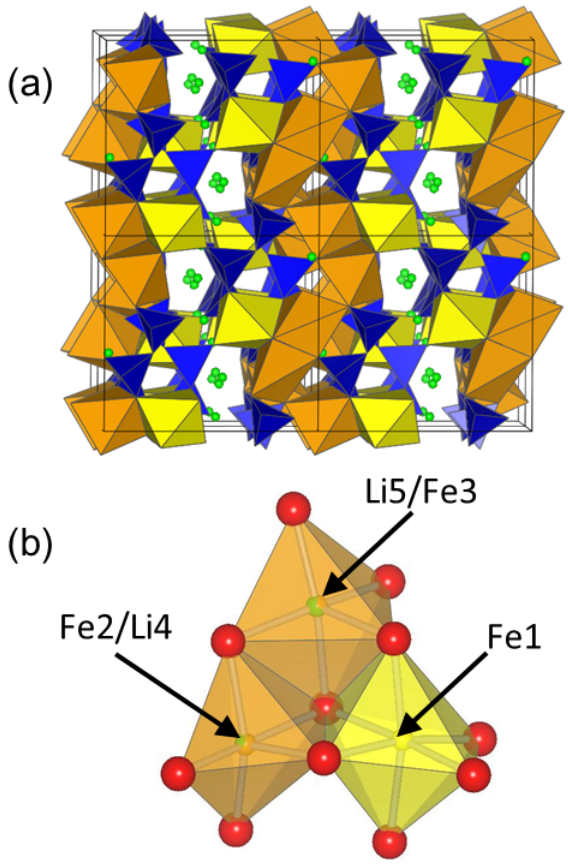

Figure 3.1: (a) Crystal structure of $Li_2FeP_2O_7$ showing Li ions (green), FeO_6 octahedra (yellow), mixed occupancy FeO_5/LiO_5 units (orange) and P_2O_7 pyrophosphate (blue). (b) Close-up view of edge sharing between an FeO_6 octahedron (fully occupied Fe1 site) and FeO_5/LiO_5 polyhedra (mixed occupied Fe2/Li4 and Li5/Fe3 sites).

The starting point of the study was to reproduce the experimentally observed crystal structures of the $Li_2FeP_2O_7$ (Figure 3.1) and $Na_2MP_2O_7$ (M = Fe, Mn) (Figure 3.2) materials. As with the structural study of a lithium deficient composition ($Li_{1.75}FeP_2O_7$) that used synchrotron x-ray diffraction, [67] the current neutron diffraction based refinement shows that $Li_2FeP_2O_7$ is essentially isostructural (space group $P2_1/c$) with $Li_2MnP_2O_7$ [77] comprised of $[P_2O_7]^{4-}$ anions which are corner shared dimers of PO_4 tetrahedra. Each of the polyhedral units share their corners or edges to form a three-dimensional framework structure (Figure

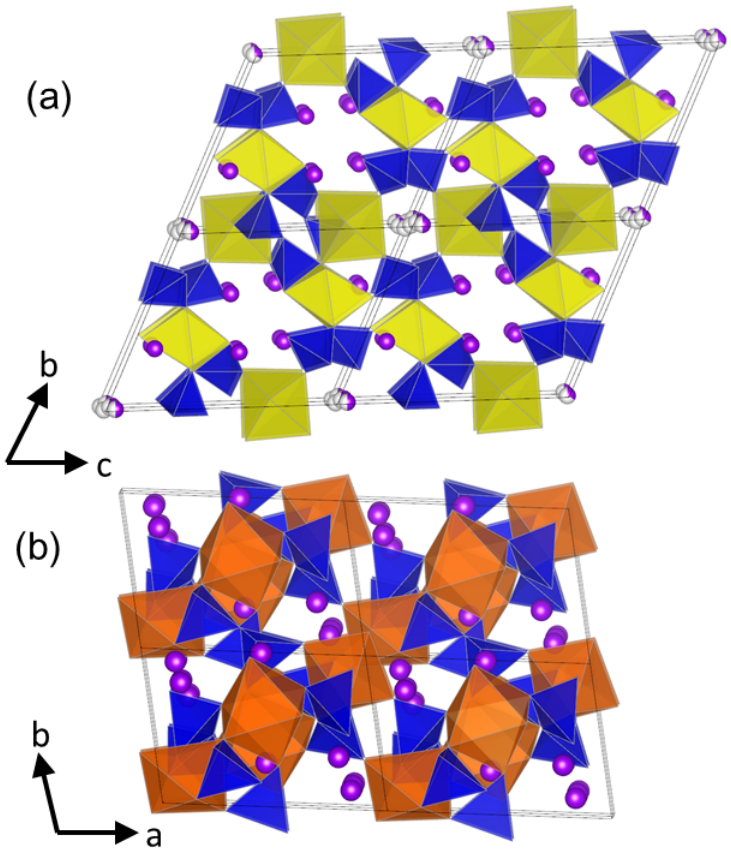

Figure 3.2: Crystal structures of $Na_2MP_2O_7$ (M = Fe, Mn). a.) $Na_2FeP_2O_7$ ($P\bar{1}$; a-axis view), b.) $Na_2MnP_2O_7$ ($P1$; c-axis view); Na ions (purple), FeO_6 octahedra (yellow), MnO_6 octahedra (orange) and P_2O_7 pyrophosphate (blue).

3.1a). The difference between the structures is the existence of significant static disordering among the Li and Fe sites. Li atoms occupy five crystallographic sites and form distorted LiO_4 tetrahedra or distorted LiO_5 trigonal-bi-pyramids. Fe atoms occupy three sites as FeO_6 octahedra or distorted FeO_5 trigonal-bi-pyramids. Two of the Li sites and two of the Fe sites are crystallographically identical giving rise to a structure with both Li and Fe mixed occupancies Li5/Fe3 (Figure 3.1b); these sites are labeled Li4/Fe2 and Li5/Fe3 and have occupancies of approximately $\frac{1}{3}$:$\frac{2}{3}$ and $\frac{2}{3}$:$\frac{1}{3}$ respectively. We stress that modelling such mixed occupancies with a supercell approach has been important in reproducing the experimental structure of stoichiometric $Li_2FeP_2O_7$.

The structure exhibited by $Na_2FeP_2O_7$ is triclinic ($P\bar{1}$) [98]. Comprised of corner-sharing FeO_6 octahedra creating Fe_2O_{11} dimers, which are interconnected by both corner-sharing and

Table 3.1: Interatomic potential and shell model parameters for $Li_2FeP_2O_7$ and $Na_2MP_2O_7$ (M = Fe, Mn).

(a) Buckingham			
Interaction	A / eV	ρ / Å	C / eV•Å^6
Li^+... O^{2-}	632.1018	0.2906	0.0
Na^+... O^{2-}	1497.830598	0.28743	0.0
Fe^{2+}... O^{2-}	1105.2409	0.3106	0.0
Mn^{2+}... O^{2-}	3248.3500	0.2690	0.0
P^{5+}... O^{2-}	1029.050	0.3470	0.0
O^{2-}... O^{2-}	22764.3	0.1490	44.53
(b) Shell model			
Species	Y / e	k / eV•Å^{-2}	
Fe^{2+}	2.997	19.26	
Mn^{2+}	3.42	95.00	
O^{2-}	-2.96	65.0	

edge-sharing with the P_2O_7 pyrophosphate groups. The FeO_6 octahedra and PO_4 tetrahedra are connected in a staggered fashion thus creating large tunnels along the [011] direction within which the Na atoms are present. The Na ions occupy six distinct crystallographic sites; three of which are fully occupied (Na1, Na2, Na3), whilst the other three adopt sites that are partially occupied (Na4, Na5, Na6).

The structure exhibited by $Na_2MnP_2O_7$ [100] consists of distorted MnO_6 octahedral and tetrahedral building blocks which are connected in a staggered manner thus creating tunnels along the [001] direction for potential Na^+ migration. The structures have corner-sharing isolated MnO_6-MnO_6 (Mn_2O_{11}) dimers, which are in turn connected by the PO_4-PO_4 (P_2O_7) diphosphate units by a mixed edge and corner-sharing fashion. The constituent Na atoms are located in eight nonequivalent crystallographic sites. It has been postulated that the complex nature of this triclinic ($P1$) structure may allow for multidimensional Na^+ diffusion [97].

The Li^+-O^{2-}, Fe^{2+}-O^{2-}, Mn^{2+}-$O^{2-}$and O^{2-}-O^{2-} interatomic potentials used to model these systems were transposed from our previous work on the $LiFePO_4$ phosphate material [44]. However, due to the irregular nature of the pyrophosphate groups it was necessary to refine the parameters for the P^{5+}-O^{2-} interaction, whilst the Na–O potential was taken from the recent study of the Na_2FePO_4F [92] cathode material. Due to the partial occupancies within

Table 3.2: Calculated and experimental structural parameters of $Li_2FeP_2O_7$ and $Na_2MP_2O_7$ (M = Fe, Mn).

Parameter	a (Å)	b (Å)	c (Å)	α (°)	β (°)	γ (°)
			$Li_2FeP_2O_7$ [152]			
calc.	11.01698	9.75416	9.80462	90.00	101.54	90.00
expt.	11.19981	9.71542	9.79088	90.00	102.85	90.00
Δ	0.183	-0.039	-0.014	0.00	1.31	0.00
			$Na_2FeP_2O_7$			
calc.	6.44903	9.48247	10.99310	64.847	86.240	73.133
expt. [98]	6.43285	9.45755	11.14316	65.156	85.486	73.493
Δ	-0.01618	-0.02492	0.14985	0.309	-0.754	0.360
			$Na_2MnP_2O_7$			
calc.	9.91736	11.16931	12.48931	148.768	121.264	69.003
expt. [100]	9.92230	11.08390	12.47260	148.387	121.945	68.423
Δ	0.00494	-0.08541	-0.01671	-0.381	0.681	-0.580

both $Li_2FeP_2O_7$ and $Na_2FeP_2O_7$ it was necessary to use a 3x1x1 supercell approach considering different cation ordering schemes as used in previous simulations [53,152,159]. The energetics of the different cation configurations were investigated by performing a series of geometry optimisations in $P1$ symmetry. We note that the lattice energy differences were found to be very small (< 20 meV), suggesting that the ordering of the Li4/Fe2 and Li5/Fe3 mixed sites within $Li_2FeP_2O_7$ and the Na4, Na5 and Na6 sites within $Na_2FeP_2O_7$ is not significant. Nevertheless, of the different cation ordering schemes investigated, the configurations that gave rise to the lowest energies were deployed as the structures for the potential models. We recognise that further structural work may be necessary to elucidate whether the ordering of the mixed/partially occupied sites may depend upon the route by which the materials are synthesised. The resulting potential parameters are listed in Table 3.1, with comparisons between the calculated unit cell parameters and those of the experimental crystal structures given in Table 3.2.

For all pyrophosphate systems, the calculated unit cell parameters deviate from experiment by at most 0.18 Å, and in most cases much less; the same is found for the individual bond lengths. The excellent reproduction of the complex low symmetry monoclinic ($Li_2FeP_2O_7$) and triclinic ($Na_2MP_2O_7$) crystal structures gives us confidence that the interatomic potential

models can be used reliably in subsequent defect and migration calculations. This work extends our previous simulation studies of the $LiMPO_4$ (M = Mn, Fe, Co, Ni) materials [44, 45] and other lithium battery electrodes (such as Li_2MSiO_4 (M = Mn, Fe), Li_2FeSO_4F and $LiVO_2$) [159, 186–188].

3.2.2 Intrinsic Atomic Defects

Insights into the defect properties of cathode materials is crucial to the full understanding of their electrochemical behaviour especially the possibility of "blocking" anti-site defects in structures showing 1D ion conduction. A series of isolated point defect (vacancy and interstitial) energies were calculated for both $Li_2FeP_2O_7$ and $Na_2MP_2O_7$(M = Fe, Mn). By combining these energies, the relative energies of formation of Frenkel and Schottky-type defects were determined. These take the following general forms (using Kröger-Vink notation and where A = Li, Na):

A Frenkel:

$$A_A^{\mathrm{x}} \longrightarrow A_{\mathrm{i}}^{\bullet} + \mathrm{V}'_A \tag{3.1}$$

M Frenkel:

$$M_M^{\mathrm{x}} \longrightarrow M_{\mathrm{i}}^{\bullet\bullet} + \mathrm{V}''_M \tag{3.2}$$

O Frenkel:

$$\mathrm{O}_{\mathrm{O}}^{\mathrm{x}} \longrightarrow \mathrm{O}''_{\mathrm{i}} + \mathrm{V}_{\mathrm{O}}^{\bullet\bullet} \tag{3.3}$$

Full Schottky:

$$2A_A^{\mathrm{x}} + M_M^{\mathrm{x}} + 2\mathrm{P}_{\mathrm{P}}^{\mathrm{x}} + 7\mathrm{O}_{\mathrm{O}}^{\mathrm{x}} \longrightarrow 2\mathrm{V}'_A + \mathrm{V}''_M + 2\mathrm{V}_{\mathrm{P}}^{''''} + 7\mathrm{V}_{\mathrm{O}}^{\bullet\bullet} + A_2MP_2O_7 \tag{3.4}$$

We also examined the A/M "anti-site" pair defect, which involves the exchange of an A^+ ion (Li^+ radius 0.74 Å, Na^+ radius 1.02 Å) with an M^{2+} ion (Fe^{2+} radius 0.78 Å and Mn^{2+} radius 0.83 Å), according to:

A/M anti-site:

$$A_A^{\mathrm{x}} + M_M^{\mathrm{x}} \longrightarrow A'_M + M_A^{\bullet} \tag{3.5}$$

This type of defect is worth investigating since anti-site or cation exchange effects have been

observed in other poly-anionic systems including $LiFePO_4$ [44, 45] and Li_2MnSiO_4. [186] It should be noted that two types of Li/Fe anti-site pair defect were considered for $Li_2FeP_2O_7$; one involving the exchange of Li and Fe ions between fully occupied sites (Li1, Li2, Li3, Fe1), and the other involving exchange of ions between mixed occupied sites (Li4/Fe2 and Li5/Fe3).

Off-stoichiometry defects (lithium deficiency or transition metal excess) were also considered for $Li_2FeP_2O_7$ according to:

$$2\mathrm{Li}_{\mathrm{Li}}^{\mathrm{x}} + \frac{1}{2}\mathrm{O}_2 \longrightarrow 2\mathrm{V}'_{\mathrm{Li}} + 2h^{\bullet} + \mathrm{Li}_2\mathrm{O} \tag{3.6}$$

$$M\mathrm{O} + 2\mathrm{Li}_{\mathrm{Li}}^{\mathrm{x}} + \frac{1}{2}\mathrm{O}_2 \longrightarrow M_{\mathrm{Li}}^{\bullet} + \mathrm{V}'_{\mathrm{Li}} + \mathrm{Li}_2\mathrm{O} \tag{3.7}$$

Our approach to electronic defects follows that used for other cathode materials (e.g., $LiFePO_4$ [41, 44]) in which we model the localized hole ($h^{\bullet}$) species (small polaron) on the divalent Fe ion as Fe^{3+}. Combining the calculated energies of isolated point defects and lattice energies, we can derive the energies for these intrinsic defect processes (equations 3.1-3.7).

Examination of the resulting defect energies listed in Table 3.3 reveals three main points. First, the magnitude of the energies suggests that formation of M Frenkel, O Frenkel and Schottky defects is unfavourable. In particular, O^{2-} vacancies and interstitials are highly unfavourable, and unlikely to occur in any significant concentration in the undoped materials, confirming the structural stability of the pyrophosphate framework in accord with thermal stability experiments [98].

Second, the most favourable type of intrinsic defect for all pyrophosphate materials is found to be the A/M anti-site pair as was predicted for the Li/Fe anti-site pair in an earlier study of $LiFePO_4$ [44, 45]. Confirmation of this prediction of anti-site defects in $LiFePO_4$ was verified by structural analysis of hydro-thermally synthesised $LiFePO_4$, [46, 189] and scanning transmission electron microscopy (STEM) studies. [46] The results for $Li_2FeP_2O_7$ suggest that presence of anti-site disorder on mixed occupied sites is likely to be much more prevalent than on fully occupied sites.

For Li/Fe anti-site defects it is possible to rationalise the cation exchange in terms of the similar volumes and coordination environments of the two cation sites. However, for the Na ion which is significantly larger the formation energy for the Na/M anti-site within the respective

Table 3.3: Energies of intrinsic atomic defects in (a) $Li_2FeP_2O_7$ and (b) $Na_2MP_2O_7$ (M = Fe, Mn).

(a) $Li_2FeP_2O_7$

Disorder type	equation	Energy /eV
Li Frenkel	3.1	1.21
Fe Frenkel	3.2	3.39
O Frenkel	3.3	3.99
Full Schottky	3.4	32.42
Li/Fe anti-site (Li1, Li2, Li3, Fe1)	3.5	0.91
Li/Fe anti-site (Li4/Fe2, Li5/Fe3)	3.5	0.22
Li^+ deficiency	3.6	5.42
Fe^{2+} excess	3.7	3.43

(b) $Na_2MP_2O_7$ (M = Fe, Mn)

		Energy /eV	
Disorder type	equation	$Na_2FeP_2O_7$	$Na_2MnP_2O_7$
A Frenkel	3.1	1.14	1.34
M Frenkel	3.2	3.52	2.93
O Frenkel	3.3	3.53	3.92
Full Schottky	3.4	33.03	38.62
A/M anti-site	3.5	0.89	0.80

$Na_2MP_2O_7$ materials is of much greater magnitude, thus suggesting lower concentrations of anti-site defects within $Na_2MP_2O_7$. Whilst the anti-site energy found within the $Na_2MP_2O_7$ materials is higher than that of $Li_2FeP_2O_7$ the formation energies for these anti-site defects are still sufficiently low to suggest that even at low temperatures there will be a small percentage of Na ions on M sites, and M ions on Na sites. The concentration of anti-site disorder would be temperature dependent and hence sensitive to experimental synthesis conditions.

Lastly, the second lowest energies for the pyrophosphate cathode materials are found for the Li or Na Frenkel defect (Table 3.3). This suggests that a very minor population of such Li or Na vacancy and interstitial defects could be present at high temperatures. In the context of ion diffusion, the anti-site defects bare more significance in the case of olivine materials as their presence blocks the only available 1D channel for alkali ion migration. Therefore, anti-site defects demand that diffusion occurs via higher energy pathways, ultimately raising the energy barrier for Na/Li ion migration [44, 92]. However, for completeness we investigate

the $Fe^{\bullet}_{Li}$ anti-site cation migration energy for $Li_2FeP_2O_7$ (see Section 3.2.4). We note that intrinsic redox processes such as oxidation and reduction were also considered. In general, the high energies ($>$ 3.2 eV) suggest that oxidation (with Fe^{3+} formation) and reduction (with Fe^{+} formation) is unlikely to be significant, and are consistent with $Li_2FeP_2O_7$ not exhibiting high intrinsic electronic conduction.

3.2.3 Alkali-Ion Migration

(i) Li-Ion Migration in $Li_2FeP_2O_7$

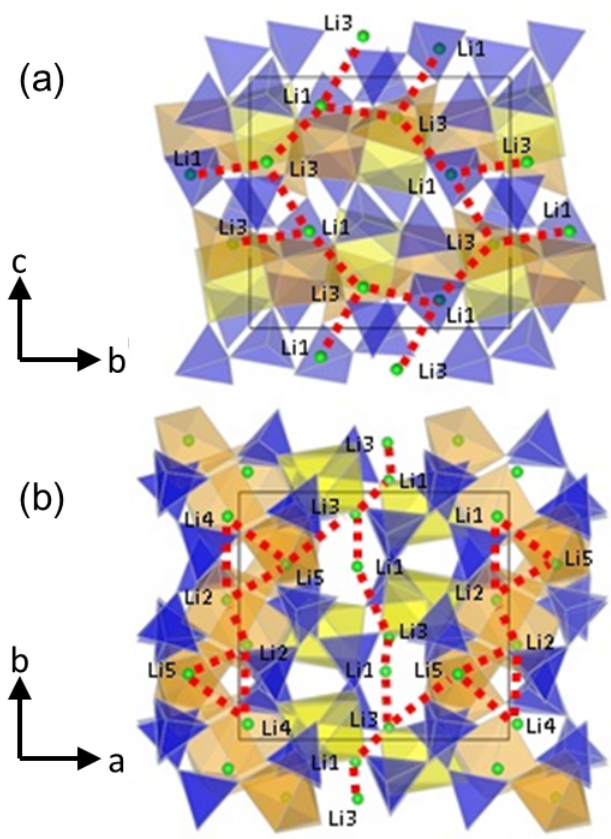

Figure 3.3: Li^{+} migration in $Li_2FeP_2O_7$ with dashed lines showing the diffusion paths considered (a) Li-Li connections in b-axis and c-axis directions; (b) Li-Li connections in a-axis and b-axis directions.

Examination of the Li ion mobility and pathways in $Li_2FeP_2O_7$ are of vital importance when considering its charge/discharge rates. However obtaining such insight for these types of complex polyhedral structures is far from straightforward. Simulation methods can greatly

Table 3.4: Calculated Li^+ migration energies and Li-Li distances within $Li_2FeP_2O_7$ (for paths shown in Figure 3.3).

Net Diffusion Direction	Li Ions Involved	Smallest Separation (Å)	Largest Separation (Å)	E_{mig} (eV)
a-axis	Li1,Li2,Li3,Li4,Li5	2.96	3.82	0.73
b-axis	Li1,Li3	2.96	3.19	0.40
c-axis	Li1,Li3	2.96	3.19	0.40

enhance our understanding of the defect process or migration pathway by evaluating the activation energies for various possible mechanisms at the atomic level.

Figure 3.3 shows that the Li diffusion pathways considered involve conventional vacancy hopping between all neighbouring Li positions along each of the three principal axes. Energy profiles for Li migration along each of these paths can be mapped out. In this way the position of highest potential energy (i.e., the 'saddle-point' configuration) can be identified from which the migration energy is derived; such an approach has been used in numerous studies on oxide ion and cation migration in complex oxides [44, 45, 128]. The resulting lowest migration energies for Li diffusion along the three main directions are reported in Table 3.4.

The lowest energy pathways are found to involve Li diffusion in the b-axis and c-axis directions with energy barriers of 0.40 eV. The final calculated paths for long-range Li^+ diffusion are shown in Figure 3.4. These paths involve Li1 and Li3 ions which have small separations (2.96 Å - 3.19 Å) but, more importantly, the channel that exists in the bc-plane is relatively unhindered (Figure 3.4b). A higher activation energy barrier of 0.73 eV is calculated for migration in the a-axis direction, which involves larger Li-Li separations of up to 3.82 Å and a path that is significantly more hindered by Fe/O and P/O polyhedra. These results indicate high Li ion mobility within the b-axis and c-axis channels, and as such $Li_2FeP_2O_7$ shows quasi-two-dimensional (2D) Li migration in the bc-plane.

Our calculated defect energies (Table 3.3a) suggest that Li/Fe anti-site defects are intrinsic to $Li_2FeP_2O_7$. Given the experimental observation of a low concentration (< 3 %) of Fe on Li sites for similarly low defect energies calculated for $LiFePO_4$ [44] it may therefore be difficult to avoid Fe cations on Li sites blocking the diffusion pathways along all of the possible migration channels, unless the anti-site defect itself is mobile. Either scenario would likely reduce the electrochemical capacity.

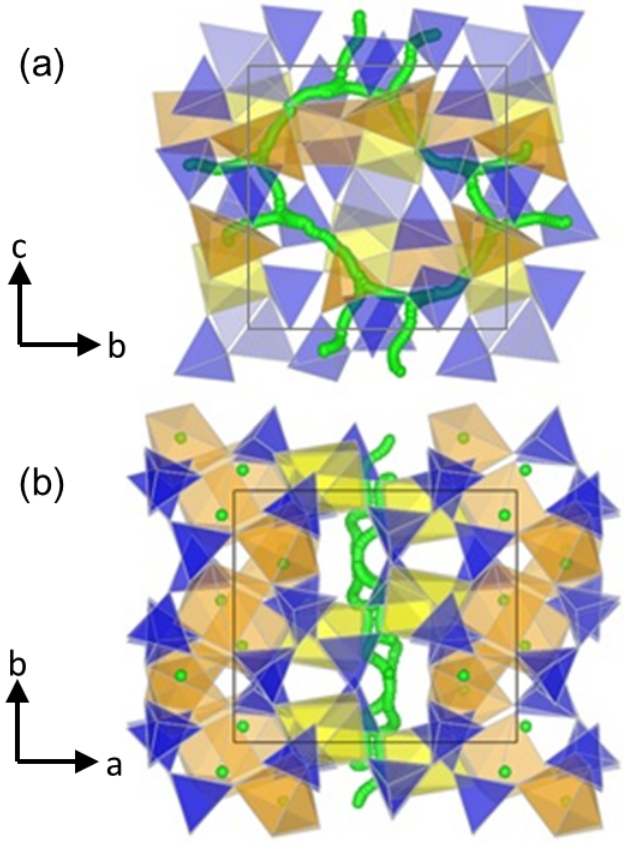

Figure 3.4: Calculated paths for long-range Li^+ migration involving Li1 and Li3 sites within b-axis and c- axis directions with activation energies of 0.40 eV; simulations indicate quasi-2D transport and non-linear pathways. (a) view of bc-plane; (b) view of ab-plane.

In order to examine whether anti-site defects affect long-range Li diffusion, the energy of migration of the divalent cation between lithium sites was calculated. This process can be viewed as an exchange of an anti-site cation ($Fe^{\bullet}_{Li}$) with a lithium vacancy (V'_{Li}) , as illustrated in Figure 3.5; the lithium vacancy would then continue to migrate in the opposite direction along the Li migration pathway. A similar simulation procedure to that for Li migration was used, which allowed the lowest energy migration path to be determined.

The calculated migration energies in Table 3.5 are 0.15∼0.52 eV greater than the corresponding Li migration values, indicating lower anti-site cation mobility compared to pure lithium diffusion. This suggests that anti-site defects ($Fe^{\bullet}_{Li}$) would impede Li diffusion to varying degrees down along the Li migration pathways. However it is also worth noting that our defect calculations suggest that the Li/Fe antisite will be more prevalent for the partially occu-

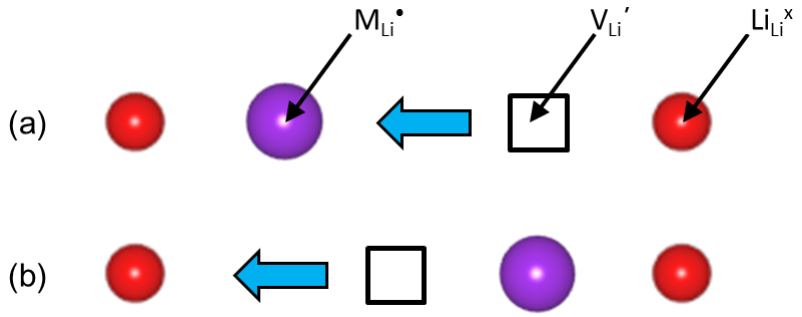

Figure 3.5: Schematic of two stages in migration of a Li vacancy (V'_{Li}) down a migration pathway of $Li_2FeP_2O_7$ near an anti-site Fe cation ($Fe^{\bullet}_{Li}$). (a) Exchange of V'_{Li} and $Fe^{\bullet}_{Li}$; (b) exchange of V'_{Li} and a lithium ion (Li^{x}_{Li}).

Table 3.5: Calculated anti-site cation ($Fe^{\bullet}_{Li}$) migration energies within $Li_2FeP_2O_7$ (for paths shown in Figure 3.3).

Net Diffusion	E_{mig} (eV)
a-axis	1.25
b-axis	0.59
c-axis	0.59

pied sites and so will have a greater affect upon lithium migration within the a-axis direction which involves the partially occupied Li4 and Li5 sites. Also, the 2D Li^+diffusion properties of $Li_2FeP_2O_7$ would be less affected by antisite defects than 1D conductors.

ii.) Na-Ion Migration in $Na_2MP_2O_7$

Table 3.6: Calculated Na^+ migration energies for the most favourable paths within $Na_2MP_2O_7$ (M = Fe, Mn)

	Migration Energies (eV)	
Net Diffusion Direction	$Na_2FeP_2O_7$	$Na_2MnP_2O_7$
a-axis	0.33	0.58
b-axis	0.42	0.58
c-axis	0.49	0.58

Na-diffusion pathways were considered between all neighbouring Na positions within the $Na_2MP_2O_7$ (M = Fe, Mn) materials along each of the three principal axes via conventional vacancy hopping, as used in the study of Li-diffusion in $Li_2FeP_2O_7$ [152]. The resulting lowest

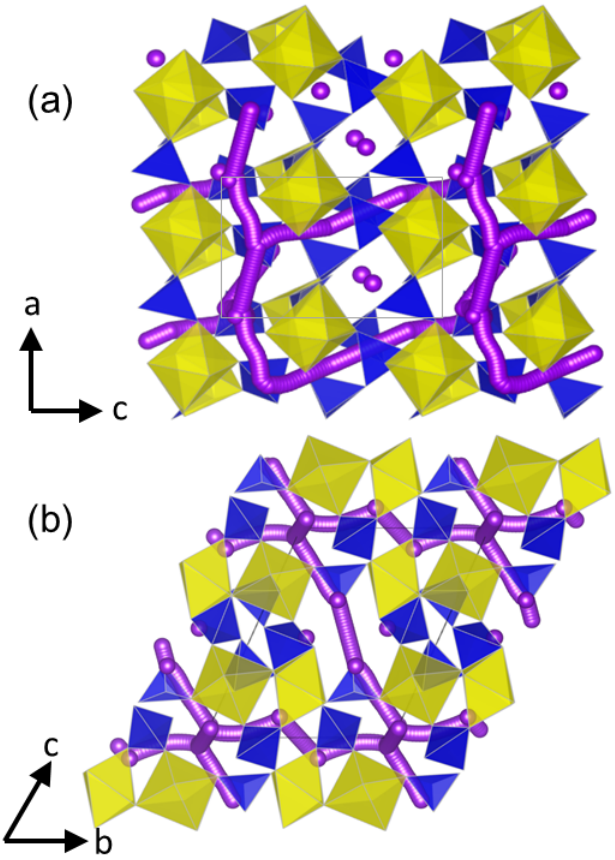

Figure 3.6: Calculated paths for long-range Na^+ migration within $Na_2FeP_2O_7$ along the a-axis, b-axis and c-axis directions with activation energies ≤ 0.49 eV; simulations indicate quasi-3D transport and non-linear pathways; a) view of the ac-plane; b) view of the bc-plane.

migration energies for Na diffusion along the three principal axes of the $Na_2MP_2O_7$ materials are reported in Table 3.6.

From the results presented in Table 3.6, it would appear that that all $Na_2MP_2O_7$ structures support quasi-three dimensional (3D) Na^+ diffusion with activation energies of 0.49 eV and 0.58 eV for $Na_2FeP_2O_7$, and $Na_2MnP_2O_7$ respectively. The final calculated paths for long-range Na^+ diffusion are shown in Figures 3.6 and 3.7. We note that in recent theoretical studies of a different $Na_2FeP_2O_7$ (triclinic, $P1$) polymorph by Choi et al. [99, 101] Na^+ diffusion was deemed to be 2D with migration barriers of ~0.54 eV. Therefore in all cases the pyrophosphate framework appears to show high alkali-ion ($Na^+$and Li^+) mobility. This behaviour contrasts with that in olivine $LiFePO_4$ and $NaFePO_4$ which only allows $Li^+$and Na^+ migration along 1D channels parallel to the b-axis [44,92]. Most importantly, ion blocking by anti-site defects

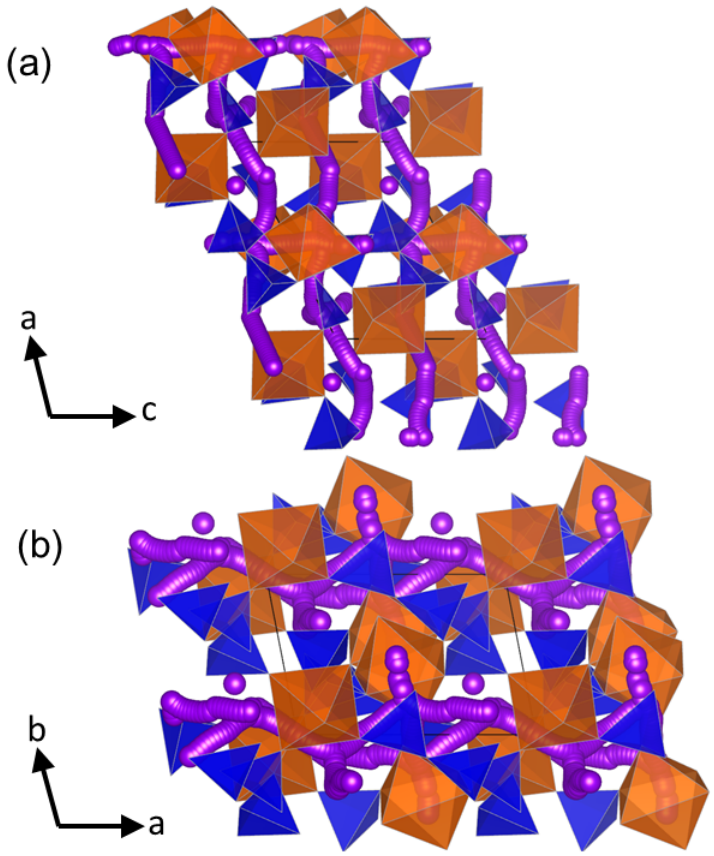

Figure 3.7: Calculated paths for long-range Na^+ migration within $Na_2MnP_2O_7$ along the a-axis, b-axis and c-axis directions with activation energies $\leq$ 0.58 eV; simulations indicate quasi-3D transport and non-linear pathways; a) view of the ac-plane; b) view of the ab-plane.

is much less likely to make a significant difference to the alkali (Na/Li) ion migration in these pyrophosphate materials than it does in the olivine materials exhibiting 1D diffusion. Hence, explicit anti-site migration was not considered here for the $Na_2MP_2O_7$ (M = Fe, Mn) materials.

It is often assumed that the migrating ion takes the shortest path between adjacent sites, i.e. a direct linear jump. However, our simulations also reveal curved paths between adjacent Na or Li sites within each of the pyrophosphate materials studied (Figures 3.6 and 3.7), which produces "wavelike" trajectories for long-range migration. It is worth noting that analogous, curved Li^+ migration paths were first predicted from atomistic simulation [44] of $LiFePO_4$, which were subsequently confirmed by neutron diffraction maximum entropy method (MEM) analysis [42]. Indeed, one of the aims of the present study is to stimulate similar experimen-

tal work on the $Li_2FeP_2O_7$ and $Na_2MP_2O_7$ pyrophosphates to probe actual Li^+ and Na^+ migration pathways. Although there are no Li^+ and Na^+ conductivity data for direct comparison, our calculated values for alkali-ion migration values are consistent with experimental activation energies for Li and Na ion conductivity in other framework-structured phosphate materials [64, 190, 191].

iii.) Volume Change and the Effect on Electrochemical Performance

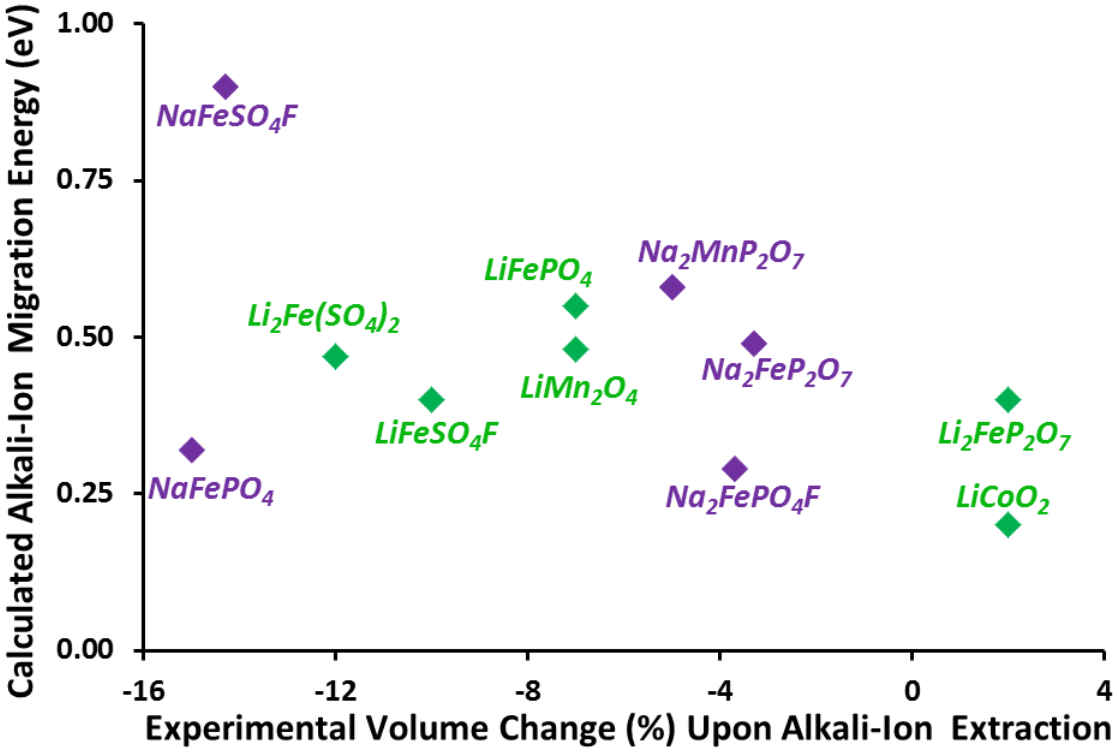

Figure 3.8: Comparison of the experimental volume change upon Li-ion or Na-ion extraction [192] against the calculated ion migration activation energy for a representative range of polyanion-type cathode materials [44, 92, 152, 159, 193]; the volume change relates to one alkali-ion per formula unit with a negative value indicating volume contraction.

There has been recent debate about the volume difference between the reduced and oxidised phases as a significant factor in determining electrochemical performance of cathode materials [92,192,194]. For two-phase processes, a phase boundary between oxidised and reduced phases is formed during charge/discharge. Electrochemical performance is affected by the amount of strain generated in this phase boundary, as well as by the activation energy barrier for Li-

ion or Na-ion transport. As a tool for useful comparison, we have plotted in Figure 3.8 the experimental volume change upon Li-ion or Na-ion extraction against the calculated ion migration activation energy for a representative range of polyanion-type cathode materials that includes olivine-phosphates, pyrophosphates and sulphates.

Strain generated in the phase boundary is proportional to the difference in the unit cell volume (ΔV) of the oxidised and reduced phases which is only ~3.3 % for $Na_2FeP_2O_7$, but > 15 % for $NaFePO_4$ and $NaFeSO_4F$. The strain contributes significantly to the overall energy for redox phase transformation. We note that while the majority of the compounds undergo volume contraction on Li/Na extraction, $Li_2FeP_2O_7$ shows a small volume expansion, although de(lithiation) has been found to be via a solid-solution mechanism in this pyrophosphate [192]. Although the interplay of all factors is still under investigation, materials with a large volume difference between the end member phases could lead to poor rate capability and also faster capacity fade as discussed by Tripathi et al [92]. Where this is coupled with a relatively high activation energy for Na-ion transport (e.g. > 0.7 eV) poor electrochemical properties can be predicted; an example being $NaFeSO_4F$ which exhibits limited intercalation capacity. In contrast, promising electrochemical properties can be anticipated for Na-based cathode materials with low volume change on cycling (e.g. < 7 %) and low ion migration activation barriers (e.g. < 0.5 eV) as in the case of $Na_2FeP_2O_7$ and Na_2FePO_4F.

3.2.4 Cation Doping in $Li_2FeP_2O_7$

Given that the current operating voltage for $Li_2FeP_2O_7$ of 3.5 V vs. Li/Li^+ was recorded without any technical effort such as nano-sizing or carbon coating it is of interest to investigate the effect of cation doping in order to gauge if it is likely to result in improved electronic conductivity. Our simulation methods, as used previously to investigate dopant substitution energetics within $LiMPO_4$ (M = Mn, Fe, Co, Ni) [44,45] can probe these issues for $Li_2FeP_2O_7$ by generating relative energies of dopant substitution. This approach can provide a useful systematic guide to the site-selectivity for different dopant species and to trends in dopant solubility. In this study we have examined a wider range of dopants in $Li_2FeP_2O_7$ than experimental reports, from monovalent to pentavalent.

For isovalent dopants (such as Na^+ on Li^+ or Mg^{2+} on Fe^{2+}), no charge-compensating

defect is required. However, for aliovalent dopants (whether donor ions such as Mg^{2+} on Li^+ or Al^{3+} on Fe^{2+}, or acceptor ions such as Na^+ on Fe^{2+}), the type of charge-compensating mechanism has not been clearly established from experiment, and could consist of either Li vacancies, Fe vacancies, O vacancies or electronic species (e.g., Fe^+, Fe^{3+}). Using Na^+ and Zr^{4+} as example dopant species on both Li and Fe sites incorporation mechanisms of the following types (normalised to a single dopant ion) were considered, as shown by equations 3.8-3.15:

Li site

No compensation:

$$\frac{1}{2}Na_2O + Li_{Li}^{x} \longrightarrow Na_{Li}^{x} + \frac{1}{2}Li_2O \tag{3.8}$$

Li^+ vacancy:

$$ZrO_2 + 4Li_{Li}^{x} \longrightarrow Zr_{Li}^{\bullet\bullet\bullet} + 3V_{Li}' + 2Li_2O \tag{3.9}$$

Fe^{2+} vacancy:

$$ZrO_2 + Li_{Li}^{x} + \frac{3}{2}Fe_{Fe}^{x} \longrightarrow Zr_{Li}^{\bullet\bullet\bullet} + \frac{3}{2}V_{Fe}'' + \frac{1}{2}Li_2O + \frac{3}{2}FeO \tag{3.10}$$

Fe^+ (electron) formation:

$$ZrO_2 + Li_{Li}^{x} + 3Fe_{Fe}^{x} \longrightarrow Zr_{Li}^{\bullet\bullet\bullet} + 3Fe_{Fe}' + \frac{1}{2}Li_2O + \frac{3}{4}O_2 \tag{3.11}$$

Fe site

Fe^{3+} (hole) formation:

$$\frac{1}{2}Na_2O + Fe_{Fe}^{x} + \frac{1}{4}O_2 \longrightarrow Na_{Fe}' + h^{\bullet} + FeO \tag{3.12}$$

Li^+ vacancy:

$$ZrO_2 + 2Li_{Li}^{x} + Fe_{Fe}^{x} \longrightarrow Zr_{Fe}^{\bullet\bullet} + 2V_{Li}' + Li_2O + FeO \tag{3.13}$$

Fe^{2+} vacancy:

$$ZrO_2 + 2Fe^{x}_{Fe} \longrightarrow Zr^{\bullet\bullet}_{Fe} + V''_{Fe} + 2FeO \tag{3.14}$$

Fe^{+} (electron) formation:

$$ZrO_2 + 3Fe^{x}_{Fe} \longrightarrow Zr^{\bullet\bullet}_{Fe} + 2e' + FeO + \frac{1}{2}O_2 \tag{3.15}$$

Table 3.7: Interatomic potential and shell-model parameters for dopant species in $Li_2FeP_2O_7$.

Short range Buckingham potentials					
Interaction	A / eV	ρ / Å	C / eV•Å^6	Y / e	k / eV•Å^{-2}
[a] Na^{+}... O^{2-}	1677.830	0.2934	0.0	1.0	9999.9
[a] K^{+}... O^{2-}	958.210	0.3606	0.0	1.0	9999.9
[a] Rb^{+}... O^{2-}	3400.57	0.3167	0.0	1.0	9999.9
[a] Ba^{2+}... O^{2-}	931.7	0.3949	0.0	1.46	14.78
[a] Ca^{2+}... O^{2-}	1228.9	0.3372	0.0	1.26	34.00
[a] Co^{2+}... O^{2-}	1670.2416	0.2859	0.0	3.503	110.5
[b] Cu^{2+}... O^{2-}	3799.3	0.2427	0.0	2.0	9999.9
[a] Mg^{2+}... O^{2-}	821.6	0.3242	0.0	2.0	9999.9
[a] Mn^{2+}... O^{2-}	2601.394	0.278	0.0	3.42	95.0
[a] Ni^{2+}... O^{2-}	1760.0	0.28	0.0	2.0	93.7
[a] Sr^{2+}... O^{2-}	1400.0	0.3500	0.0	1.33	21.53
[a] La^{3+}... O^{2-}	1545.21	0.3590	0.0	-0.25	145.0
[a] Sc^{3+}... O^{2-}	1299.4	0.3312	0.0	3.0	9999.9
[a] Y^{3+}... O^{2-}	1345.1	0.3491	0.0	3.0	9999.9
[c] Ce^{4+}... O^{2-}	1986.83	0.3511	20.40	7.7	291.75
[d] Sn^{4+}... O^{2-}	1056.8	0.3683	0.0	1.58	2037.8
[e] Ti^{4+}... O^{2-}	511.7	0.2625	0.0	-0.1	314.0
[f] V^{4+}... O^{2-}	1290.56	0.34039	0.0	4.0	9999.9
[g] Nb^{5+}... O^{2-}	1286.9583	0.371525	0.0	-4.596	5916.77
[f] V^{5+}... O^{2-}	2549.73	0.34115	0.0	5.0	9999.9

a [45]; *b* [195]; *c* [196]; *d* [197]; *e* [198]; *f* [199]; *g* [200].

We therefore calculated the overall substitution energy for a variety of different compensation mechanisms, as described above. The energies of these dopant substitution or 'solution' reactions were calculated by combining the appropriate defect and lattice energy terms for

Table 3.8: Calculated dopant solution energies and ionic radii for a range of dopants in $Li_2FeP_2O_7$.

		Solution Energy (eV/dopant)	
Dopant	Ionic Radius (Å)	Li Site	Fe Site
Na^+	1.02	-0.80	1.51
K^+	1.38	0.97	2.77
Rb^+	1.52	0.49	2.59
Ba^{2+}	1.35	4.85	1.71
Ca^{2+}	1.00	1.73	-0.86
Co^{2+}	0.75	1.86	-0.30
Cu^{2+}	0.73	2.51	0.36
Mg^{2+}	0.72	3.35	1.19
Mn^{2+}	0.83	0.77	-1.46
Ni^{2+}	0.69	2.11	-0.08
Sr^{2+}	1.18	1.54	-1.41
La^{3+}	1.03	5.21	1.83
Sc^{3+}	0.75	5.01	2.30
Y^{3+}	0.90	4.47	1.48
Ce^{4+}	0.87	8.94	5.54
Sn^{4+}	0.69	8.20	5.27
Ti^{4+}	0.61	8.36	5.06
V^{4+}	0.58	9.86	6.95
Nb^{5+}	0.64	NC[a]	8.76
V^{5+}	0.56	10.9	9.06

[a]NC = non-convergence of calculation

each equation. Interatomic potentials used to model the corresponding binary oxides of the dopant cations were used in each case (Table 3.7). For transition metal substitution (e.g. Cu^{2+} on Fe^{2+}), d-orbital electronic effects are included implicitly in the effective potentials through empirical derivation. This systematic approach has been applied successfully to other oxide and silicate systems in addition to the $LiMPO_4$ (M = Mn, Fe, Co, Ni) phosphates as mentioned previously [44,45]. The dopant calculations were also carried out at the dilute limit, as is appropriate for examining low dopant concentrations.

Dopant incorporation ('solution') energies for a range of cation dopants are provided in Table 3.8, with the most favourable energies for the Li or Fe sites plotted as a function of ionic

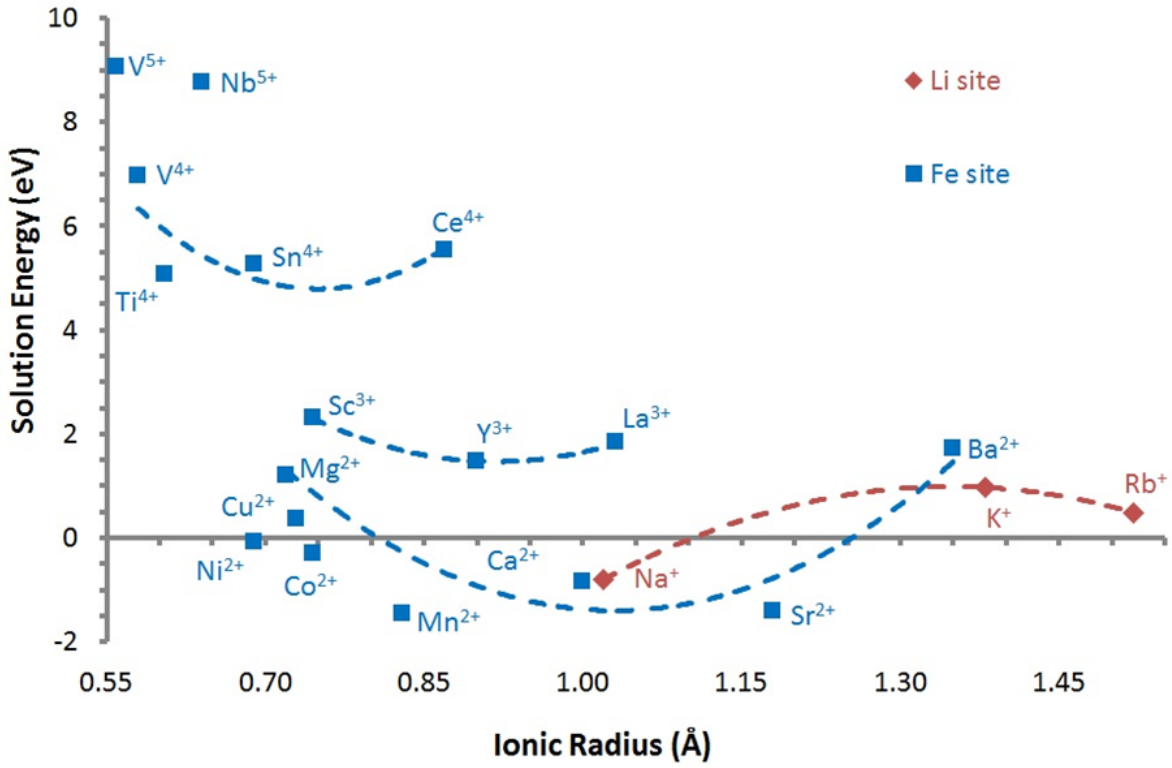

Figure 3.9: Calculated dopant solution energies versus dopant ionic radius for $Li_2FeP_2O_7$. Only the most favourable energies for the Li and Fe sites are shown. Lines for M^+, M^{2+} (alkaline-earth), M^{3+} and M^{4+} dopants are guides for the eye.

radius in Figure 3.9. These results indicate two main features. First, the lowest energies were found for isovalent substitution; in particular, Na^+ doping for Li^+ and divalent doping (e.g. Mn^{2+}, Ni^{2+} and Sr^{2+}) for Fe^{2+} were found to be favourable. In general, the less favourable dopant sites were more than 2 eV higher in energy. However, isovalent substitution does not require charge compensation and hence would not lead to an increase in the number of electronic charge carriers.

Partial substitution of Fe by other divalent transition metal ions may be used to tune (or increase) the Fe^{2+}/Fe^{3+} redox potential through the inductive effect [6]. Interestingly, our results suggest that the most favourable dopant for Fe^{2+} is Mn^{2+}; indeed, Furuta et al [70] have recently investigated the $Li_{2-x}(Fe_{1-y}Mn_y)P_2O_7$ solid solution and found evidence of enhanced redox potentials approaching 4.0 V.

Second, a key result is that supervalent doping (especially of Nb^{5+} and V^{5+}) is unfavourable. This result suggests that these ions are unlikely to be incorporated beyond very

low concentrations (< 3 %). The compensation mechanism for such supervalent dopants was found to be Fe^{2+} vacancies, whereas compensation by a change in Fe^{2+} charge state (i.e., to give an Fe^{+} small polaron species) was much higher in energy. These results suggest that such donor dopants will not lead to changes in Fe oxidation state or to an enhanced electronic conductivity. The overall trends reveal that the greater the difference between the charges of the dopant and host ion, the higher the dopant incorporation energy (e.g., for the Fe site, solution energies increase as $Co^{2+} < Sc^{3+} < Sn^{4+} < Nb^{5+}$). This trend suggests that electrostatic interactions dominate the energetics of dopant incorporation in $Li_2FeP_2O_7$. Future work will include similar calculations on cation doping within the sodium-based ($Na_2MP_2O_7$) pyrophosphates.

3.3 Chapter Summary

In conclusion, this systematic survey of the $Li_2FeP_2O_7$ and $Na_2MP_2O_7$ (M = Fe, Mn) pyrophosphate cathodes used atomistic simulation techniques to provide insights into their defect chemistry and alkali-ion (Li^+/Na^+) migration pathways. The main results can be summarised as follows:

1. First, the atomistic simulations show good reproduction of the observed complex structures of these pyrophosphate materials. Second, the defect calculations indicate the stability of the pyrophosphate framework towards oxygen evolution, which is important for operational safety. The most favourable intrinsic defect type is the Li/Fe and Na/M antisite, with the relative energies suggesting greater Li/Fe disorder in the $Li_2FeP_2O_7$ material as observed. This is especially true for the mixed occupied sites (Li4/Fe2 and Li5/Fe3) of $Li_2FeP_2O_7$, which would be sensitive to synthesis conditions. Our simulations also show the second lowest energy defect to be the Li or Na Frenkel, suggesting a very minor population of such Li or Na vacancy and interstitial defects could be present at high temperatures.

2. Lithium diffusion within $Li_2FeP_2O_7$ will follow non-linear, curved paths in the b-axis and c-axis directions via Li1/Li3 sites, which show low migration energies (0.40 eV). In comparison, both $Na_2FeP_2O_7$ and $Na_2MnP_2O_7$ are predicted to exhibit curved diffusion

pathways parallel to the a-, b- and c-axes with low migration energies (∼0.50 eV). Hence, in contrast to 1D diffusion in $LiFePO_4$, the pyrophosphate framework appears to support 2D Li^+ diffusion in $Li_2FeP_2O_7$ and 3D Na^+ diffusion in $Na_2MP_2O_7$, which is important for good rate capability and for the function of particles without nano-sizing. These results and the relatively low volume change on Na-ion extraction (< 5 %) are consistent with the high rate kinetics observed for $Na_2FeP_2O_7$. For the $Li_2FeP_2O_7$ the lowest anti-site migration energies (0.59 eV) were found for net diffusion within the a-axis and b-axis channels, suggesting that the presence of any anti-site defects along these channel would have the smallest effect on lithium diffusion kinetics.

3. Within $Li_2FeP_2O_7$ favourable doping is found for Na^+ on the Li^+ site, and isovalent dopants (e.g., Mn^{2+}, Co^{2+}, Cu^{2+}) on the Fe^{2+} site; the latter could be used in attempts to increase the Fe^{2+}/Fe^{3+} redox potential towards 4V. In contrast, supervalent doping (especially V^{5+} and Nb^{5+}) appears unfavourable on both $Li^+$and Fe^{2+} sites; the charge-compensation mechanism found for such doping does not alter the Fe^{2+} valence state and hence is unlikely to enhance electronic conductivity.

In general, the results presented here provide a valuable framework for the future optimisation of high voltage pyrophosphate materials for next-generation lithium and sodium batteries.

Chapter 4

$Li_2M(SO_4)_2$ (M = Fe, Mn, Co) Sulphates: Voltage Trends, Lithium Diffusion and Surfaces

4.1 Background

Newly synthesised lithium iron sulphate, with composition $Li_2Fe(SO_4)_2$, has been shown to display a theoretical capacity of 102 mA h g^{-1} and a high potential of 3.83 V vs. Li/Li^+ for the Fe^{2+}/Fe^{3+} redox couple. Therefore this material offers the highest reported voltage for a fluorine-free iron-based compound [103]. Further studies of the structural and transport properties will provide useful insights into this significant iron-sulphate system and may subsequently provide a new platform for related lithium battery electrode research. There is also interest in both the previously reported $Li_2Co(SO_4)_2$ phase [103] and the recently synthesised $Li_2Mn(SO_4)_2$ phase [104].

The $Li_2M(SO_4)_2$ (M = Co, Mn, Fe) marinite family of sulphate compounds are isostructural comprising isolated MO_6 octahedra linked through shared oxygen vertices with the surrounding SO_4 tetrahedra, as shown in Figure 4.1. Whilst each MO_6 octahedra is linked to six SO_4 tetrahedra, forming a star or pinwheel pattern when viewed along the b-axis, each SO_4 is only bound to three MO_6 octahedra and the fourth unshared corner of the SO_4 tetrahedron points into an open channel where the lithium resides [103,104].

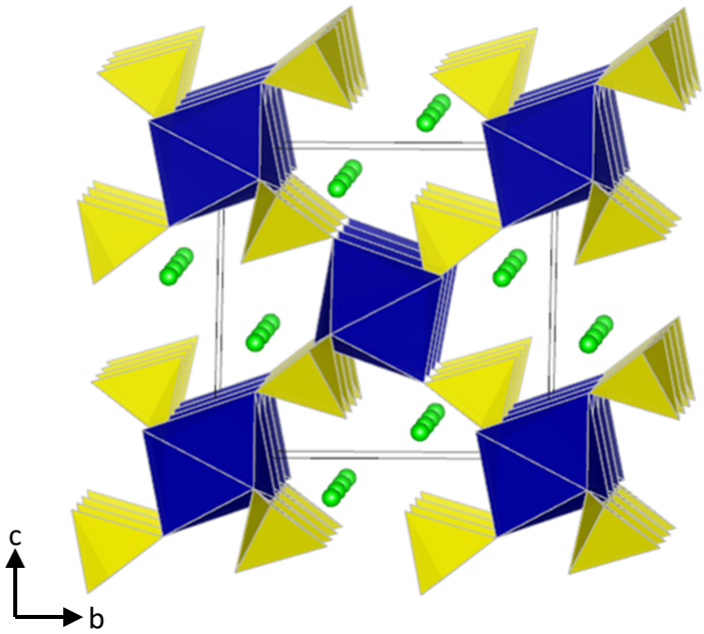

Figure 4.1: $Li_2M(SO_4)_2$ (M = Fe, Mn, Co) crystal structure showing MO_6 octahedra (blue), SO_4 tetrahedra (yellow) and chains of Li ions (green) running parallel to the a-axis.

Despite the isostructural nature of the materials, only $Li_2Fe(SO_4)_2$ is found to show electrochemical activity [103, 104]. Upon cycling, the $Li_2Fe(SO_4)_2$ material transforms to the delithiated phase $LiFe(SO_4)_2$ through a biphasic mechanism, as suggested by the plateau observed at 3.83 V vs. Li/Li^+ on the electrochemical curve and further confirmed by in-situ XRD measurements [103]. The delithiated phase is found to maintain the general 3D framework of $Li_2Fe(SO_4)_2$ [104], however the FeO_6 octahedra and SO_4 tetrahedra undergo slight rotations upon lithium removal. Therefore, each octahedron is still linked to six SO_4 tetrahedra with the fourth unshared corner of the SO_4 tetrahedra pointing at the open channels where the lithium resides. However, in contrast to the lithiated phase, the lithium ions of the oxidised $LiFe(SO_4)_2$ were localized at the centre of the channels, in a half-occupied general position in the vicinity of the $(\frac{1}{2}\ 0\ \frac{1}{2})$ site [104]. Figure 4.2 shows the resulting crystal structure. The present study uses density functional theory (DFT) and atomistic simulation methods to investigate important issues for the $Li_2M(SO_4)_2$ (M = Co, Mn, Fe) family of cathodes related to their voltage trends, lithium diffusion and surface structures.

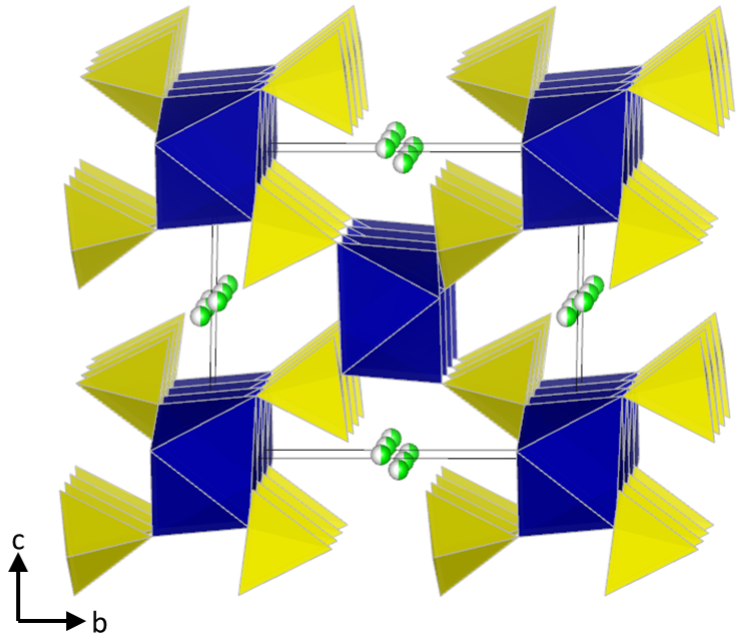

Figure 4.2: Crystal structure of the delithiated phase $LiFe(SO_4)_2$ showing FeO_6 octahedra (blue), SO_4 tetrahedra (yellow) and Li ions (green) running parallel to the a-axis.

4.2 Results and Discussion

4.2.1 Structure and Voltage Trends: Electronic Structure Calculations

DFT calculations were performed using the plane wave code VASP [201]. Since we required optimised lattice parameters, the basis set was converged against the stress which is more sensitive to an under-converged basis set than the forces. A cutoff energy of 750 eV with a k-point mesh density of at least 0.04 $Å^{-1}$ was needed to adequately converge the stress (6×4×4 grid). PAW potentials [183, 202] and the PBE exchange and correlation functional [175] were used. An anti-ferromagnetic ordering of the moments on all transition metal (Fe, Mn and Co) atoms was found to be lower in energy than a ferromagnetic ordering, in line with magnetic measurements (T_N < 8 K for $Li_2M^{II}(SO_4)_2$ with M = Co, Mn, Fe, and TN = 35 K for $LiFe^{III}(SO_4)_2$) and with the magnetic structures deduced at 2 K from neutron powder diffraction. [104] DFT + U was used with effective Hubbard U_{eff} = U – J = 4.0, 3.9 and 5.7 eV (J = 1.0 eV) for Fe, Mn and Co respectively; these values are in agreement with the U values calculated self-consistently for Fe-, Mn- and Co- based cathodes [203].

Previous DFT studies on a variety of oxide electrode materials [204–206] have shown

that such methods are well suited to probing lithium insertion/extraction properties and to predicting precise trends in cell voltages. Using the diffraction refined structural data for the lithiated ($Li_2M(SO_4)_2$ materials) and delithiated ($LiFe(SO_4)_2$) structures we have calculated the open circuit voltages using equation 4.1:

$$V = \frac{\epsilon\{Li_2M\,(SO_4)_2\} - \epsilon\{Li_xM\,(SO_4)_2\} - \{2-x\}\mu\{Li\}}{2-x} \tag{4.1}$$

Where $\varepsilon\{Y\}$ is the total energy of Y and x is the number of lithium atoms per formula unit removed. In practice we have removed one lithium atom per formula unit to produce the end member $LiM(SO_4)_2$ (M = Fe, Mn, Co). Metallic lithium was used to calculate the chemical potential of a single lithium atom $\mu\{Li\}$, which is standard practice for cell voltage calculations.

Table 4.1: Comparison of the calculated (DFT) and experimental structural parameters of $Li_2M(SO_4)_2$ (M = Fe, Mn, Co) and $LiFe(SO_4)_2$.

Parameter	a (Å)	b (Å)	c (Å)	β (°)
$Li_2Fe(SO_4)_2$				
calc. (GGA+U)	5.0453	8.2894	8.9848	121.80
expt. [104]	4.9886	8.2062	8.8293	121.75
Δ	0.0567	0.0832	0.1555	0.05
$Li_2Mn(SO_4)_2$				
calc. (GGA+U)	5.0537	8.4295	9.0098	120.95
expt. [104]	4.9920	8.3396	8.8614	121.23
Δ	0.0617	0.0899	0.1484	-0.28
$Li_2Co(SO_4)_2$				
calc. (GGA+U)	5.0248	8.1970	8.9149	121.30
expt. [104]	4.9787	8.1113	8.7831	121.81
Δ	0.0461	0.0857	0.1318	-0.51
$LiFe(SO_4)_2$				
calc. (GGA+U)	4.8913	8.4477	8.0559	121.30
expt. [104]	4.7974	8.3815	7.8956	121.83
Δ	0.0939	0.0662	0.1603	-0.53

The DFT simulations have reproduced the $Li_2M(SO_4)_2$ (M = Fe, Mn, Co) experimental structures and also the delithiated $LiFe(SO_4)_2$ observed structure with a high level of accuracy

Table 4.2: Calculated cell voltages (vs. Li/Li^+) in $Li_2M(SO_4)_2$ (M = Fe, Mn, Co).

Process	expt. (V) [103]	calc. (V)
$Li_2Fe(SO_4)_2 \leftrightarrow LiFe(SO_4)_2$	3.83	3.91
$Li_2Mn(SO_4)_2 \leftrightarrow LiMn(SO_4)_2$	-	4.54
$Li_2Co(SO_4)_2 \leftrightarrow LiCo(SO_4)_2$	-	5.20

(Table 4.1). The computed cell voltage relies on a knowledge of the structure of the delithiated end member $LiFe(SO_4)_2$. Typically for cell voltage calculations the relevant lithium atoms are removed directly from the lithiated structure, which is then energy minimised to form the delithiated structure. Numerous configurations of differing lithium ordering schemes were considered, and in our calculations we used the lowest energy structure. However, this energy minimisation may only find the local energy minimum and it is entirely possible that a phase change can occur on lithium extraction.

The cell voltage computed directly in this way for $Li_2Fe(SO_4)_2$ is 3.99 V which is in reasonable agreement with the measured voltage of 3.83 V [103]. However, using the joint Synchrotron XRD/neutron refined $LiFe(SO_4)_2$ structure [104], it is clear that the main difference between the lithiated and delithiated materials is that in the $Li_2Fe(SO_4)_2$ structure (Figure 4.1) there are two rows of lithium in a zig-zag arrangement whereas in the $LiFe(SO_4)_2$ structure (Figure 4.2) there is a single row in the centre of the channel. This subtle change in the structure results in a computed cell voltage of 3.91 V, which is in better agreement with that measured experimentally (Table 4.2). This result highlights the effect of structural changes on lithium removal and their importance in cell voltage computations.

Having isolated the delithiated ($LiFe(SO_4)_2$) structure we have subsequently calculated voltages for the Mn- and Co-based sulphates by setting both $LiMn(SO_4)_2$ and $LiCo(SO_4)_2$ initial structures equivalent to $LiFe(SO_4)_2$ prior to structural relaxation. The voltages calculated for $Li_2M(SO_4)_2$ (M = Fe, Mn, Co) are presented in Table 4.2.

Our calculations suggest that both $Li_2Mn(SO_4)_2$ and $Li_2Co(SO_4)_2$ have higher cell voltages than that of $Li_2Fe(SO_4)_2$ as typically observed for polyanion cathodes. The value for the Co-based sulphate is above the electrolyte stability window. Such a significant shift upwards in voltage is found for other Co-polyanion compounds, such as $LiCoPO_4$ for which a voltage of 4.8 V vs. Li/Li^+ has been experimentally observed [66] in comparison to 3.4 V for $LiFePO_4$.

The Mn-based sulphate is known to be electrochemically inactive. As the system is delithiated, Mn^{3+} (d^4) forms which is a Jahn-Teller active valence state. It has been debated whether Jahn-Teller distortion of the MnO_6 octahedra could lead to non-uniform structural distortions which will render the delithiated phase unstable and thus unable to form. Such effects are well known in other Mn-based battery materials [38, 207]. GGA +U calculations provide a useful probe of local structural distortions that are not affected by thermal motion and statistical averaging over many unit cells. To check for Jahn-Teller effects we have examined the MO_6 distortion in the Fe, Co and Mn based sulphates which is presented in Table 4.3. For this we have used the Baur [208] distortion coefficient, D, which is defined by equation 4.2:

$$D = \frac{1}{n}\sum_{i=1}^{n}\frac{\mid l_i - l_{av} \mid}{l_{av}} \tag{4.2}$$

where l_i is the distance from the central atom to the ith coordinating atom, and l_{av} is the average bond length to n coordinating atoms.

Table 4.3: Calculated M-O bond lengths and MO_6 octahedral distortion in $Li_2M(SO_4)_2$ and delithiated $LiM(SO_4)_2$ (where M = Fe, Mn, Co).

Material	Mean M-O bond length (Å)	MO_6 Distortion Coefficient (x10^{-2})
$Li_2Fe(SO_4)_2$	2.15	1.8
$LiFe(SO_4)_2$	2.01	1.4
$Li_2Mn(SO_4)_2$	2.21	2.0
$LiMn(SO_4)_2$	2.08	7.2
$Li_2Co(SO_4)_2$	2.12	1.6
$LiCo(SO_4)_2$	2.01	2.0

The data in Table 4.3 indicate that all the lithiated structures $Li_2Fe(SO_4)_2$, $Li_2Mn(SO_4)_2$ and $Li_2Co(SO_4)_2$ possess a similar degree of distortion. Upon delithiation there is a large increase in the MnO_6 distortion with a coefficient of 7.2 x10^{-2} (compared to 1.4 x10^{-2} and 2.0 x10^{-2} for FeO_6 and CoO_6 respectively). Since the Mn-based sulphate is electrochemically inactive, the calculated voltage presented in Table 4.2 assumes the same delithiated starting structure as the Co and Fe based sulphates but contains cooperative Jahn-Teller distortion after structure relaxation.

A possible source of the different cell voltages for $Li_2M(SO_4)_2$ (M = Fe, Mn, Co) is in the

relative strength of the corresponding Fe^{2+}/Fe^{3+}, Mn^{2+}/Mn^{3+} and Co^{2+}/Co^{3+} redox couples. As with other systems involving M^{2+}/M^{3+} redox couples we would expect the respective M-O bond lengths to shorten upon Li removal (oxidation) within these sulphate systems. This is indeed found with the Fe-O bond lengths contracting by ∼6.5 % (from 2.15 Å to 2.01 Å), the Mn-O bond lengths contracting by ∼6 % (from 2.21 Å to 2.08 Å) and the Co-O bond lengths contracting by ∼5 % (from 2.12 Å to 2.01 Å).

However, distinguishing among the most reliable parameters to account for voltage variation is not an easy task. The voltage also depends upon many factors such as: inductive effects of SO_4, PO_4 and SiO_4 [6]; the degree of ionic or covalent character of the cation-anion bonds; and the Madelung energy of the ionic component of the bonding. Another possibility relates to the inductive effect played by lithium, which has been used [6] to account for the large voltage shift displayed by the Mn^{4+}/Mn^{3+} redox couple in $LiMn_2O_4$ when Li ions are shifting from octahedral to tetrahedral sites. There are obviously hidden issues which remain to be unravelled, and are part of on-going studies.

4.2.2 Intrinsic Atomic Defects

The starting point of the potentials-based simulation study was to reproduce the experimentally observed crystal structures exhibited by the $Li_2M(SO_4)_2$ (M = Fe, Mn, Co) electrode materials. The Li-O, Fe-O and O-O interatomic potentials were taken directly from the recent study of the related tavorite $LiFeSO_4F$ material [159], whilst the Mn-O and Co-O potentials were refined from those used for the study of $LiMnPO_4$ and $LiCoPO_4$ [45]. For the more covalent sulphate (SO_4^{2-}) component, the interatomic potential model successfully formulated to simulate M_2SO_4 (M = Na, K, Rb and Cs) and XSO_4 (X = Sr, Ca, Ba) was used [153–156]. An additional three-body term was used for the SO_4^{2-} units as previously used for sulphates [153–156], silicates [187] and phosphates [44, 45, 53]. Table 4.4 lists the interatomic potential parameters used in this study.

A direct comparison of their calculated and experimental structures is given in Table 4.5, which shows that the unit cell parameters calculated by interatomic potentials deviate from the experiment by at most 0.1 Å, and in most cases by much less; the same is found for the individual bond lengths with mean deviations less than 0.03 Å. The successful reproduction of

Table 4.4: Interatomic potential and shell model parameters for $Li_2M(SO_4)_2$ (M = Fe, Mn, Co).

(a) Buckingham			
Interaction	A / eV	ρ / Å	C / eV•Å^6
Li^{+}... $O^{0.84-}$	4787.6	0.19998	0.0
Fe^{2+}... $O^{0.84-}$	6448.5	0.22	0.0
Mn^{2+}... $O^{0.84-}$	1210.85	0.2825	0.0
Co^{2+}... $O^{0.84-}$	1163.5	0.27	0.0
$O^{0.84-}$... $O^{0.84-}$	103585.030	0.20	25.93
(b) Morse			
	D_e (eV)	a (Å^{-1})	r_0 (Å)
$O^{0.84-}$... $S^{1.36+}$	5.0	1.20	1.505
(c) Three-body			
	k / eV•rad^{-2}	ϑ_0 / °	
$O^{0.84-}$... $S^{1.36+}$... $O^{0.84-}$	15.0	109.47	
(d) Shell model			
Species	Y / e	k / eV•Å^{-2}	
Fe^{2+}	2.997	19.26	
Mn^{2+}	3.42	95.00	
Co^{2+}	3.503	110.50	

these complex sulphate structures gives us confidence that the potential models can be used reliably for subsequent defect, diffusion and surface calculations.

As noted, insight into the defect properties of cathode materials is crucial to the full understanding of their electrochemical behaviour. Isolated point defect (vacancy and interstitial) energies were calculated for these sulphate systems, which were combined to determine the formation energies for Frenkel- and Schottky-type intrinsic defects. As in **Chapter 3**, the following equations represent the reactions involving these defects (using Kröger-Vink notation and where M = Fe, Mn or Co):

Li Frenkel:

$$\mathrm{Li}_{\mathrm{Li}}^{\mathrm{x}} \longrightarrow \mathrm{Li}_{\mathrm{i}}^{\bullet} + \mathrm{V}_{\mathrm{Li}}^{\prime} \tag{4.3}$$

M Frenkel:

$$M_M^{\mathrm{x}} \longrightarrow M_{\mathrm{i}}^{\bullet\bullet} + \mathrm{V}_M^{\prime\prime} \tag{4.4}$$

Table 4.5: Comparison of the calculated (interatomic potentials) and experimental structural parameters of $Li_2M(SO_4)_2$ (M = Fe, Mn, Co).

Parameter	a (Å)	b (Å)	c (Å)	β (°)
$Li_2Fe(SO_4)_2$				
calc.	4.9518	8.2212	8.9293	121.86
expt. [104]	4.9886	8.2062	8.8293	121.75
Δ	-0.0368	0.0150	0.1000	0.11
$Li_2Mn(SO_4)_2$				
calc.	4.9478	8.2930	8.9456	121.58
expt. [104]	4.9920	8.3396	8.8614	121.23
Δ	-0.0442	-0.0466	0.0842	0.35
$Li_2Co(SO_4)_2$				
calc.	4.9596	8.0875	8.8142	121.37
expt. [104]	4.9787	8.1113	8.7831	121.81
Δ	0.0191	0.0238	0.0311	-0.44

Full Schottky:

$$2Li_{Li}^{x} + M_{M}^{x} + 2S_{S}^{x} + 8O_{O}^{x} \longrightarrow 2V_{Li}^{\prime} + 2V_{M}^{\prime\prime} + 2V_{S}^{\prime\prime\prime\prime\prime\prime} + 8V_{O}^{\bullet\bullet} + Li_2M(SO_4)_2 \tag{4.5}$$

We also investigated the Li/M "anti-site" pair defect, which involves the exchange of an Li^+ ions (ionic radius of 0.74 Å) with an M^{2+} ion (Fe^{2+} radius 0.78 Å, Mn^{2+} radius 0.83 Å and Co^{2+} radius 0.75 Å) according to equation 4.6:

Li/M anti-site:

$$Li_{Li}^{x} + M_{M}^{x} \longrightarrow Li_{M}^{\prime} + M_{Li}^{\bullet} \tag{4.6}$$

This type of defect is worth investigating since Li/M anti-site or cation exchange effects have been observed in other poly-anionic systems including $LiMPO_4$ (M = Mn, Fe, Co, Ni) [44,45] and $Li_2FeP_2O_7$ [152].

Examination of the resulting defect energies listed in Table 4.6 reveals two main predictions. First, the formation of all Frenkel and Schottky defects is unfavourable in all $Li_2M(SO_4)_2$ structures. This suggests that the creation of vacancies (especially oxygen vacancies) and interstitial defects are unfavourable on energetic grounds. Second, the anti-site energies are also relatively high, which suggests that there would be no significant concentration of M on

Table 4.6: Energies of intrinsic atomic defect processes in $Li_2M(SO_4)_2$ (M = Fe, Mn, Co).

		Energy /eV		
Disorder type	equation	$Li_2Fe(SO_4)_2$	$Li_2Mn(SO_4)_2$	$Li_2Co(SO_4)_2$
Li Frenkel	4.3	3.77	3.54	3.51
M Frenkel	4.4	9.88	10.14	9.26
Schottky	4.5	20.96	19.92	19.51
Li/M anti-site	4.6	3.92	3.65	3.50

Li sites at operating temperatures in these fluorine-free sulphate materials, and is consistent with the experimental data. This result contrasts with the $LiMPO_4$ (M = Mn, Fe, Co and Ni) materials, [44, 189, 209] which exhibit cation exchange behaviour between M and Li sites. The contrast may be related to differences in structure and in the bonding of the polyanion groups. Therefore these results suggest that conduction "blocking" effects involving Fe, Mn or Co on Li sites are much less likely in the $Li_2M(SO_4)_2$ cathode materials.

4.2.3 Li-Ion Diffusion

Table 4.7: Activation energies for Li migration paths (illustrated in Fig. 4.3) for $Li_2M(SO_4)_2$ (M = Fe, Mn, Co).

	$Li_2Fe(SO_4)_2$		$Li_2Mn(SO_4)_2$		$Li_2Co(SO_4)_2$	
Path	Distance (Å)	E_{mig} (eV)	Distance (Å)	E_{mig} (eV)	Distance (Å)	E_{mig} (eV)
L1	2.79	0.33	2.89	0.39	2,87	0.32
L2	4.82	1.61	4.82	1.58	4.75	1.20
L3	4.88	1.72	4.95	1.93	4.81	1.77
L4	4.96	0.47	5.10	0.54	4.87	0.42
L5	4.99	1.79	4.99	1.74	4.96	1.98

To fully understand charge/discharge rates of potential cathodes, it is important to examine the energy barriers and dimensionality of lithium migration. Using atomistic simulation techniques, it is possible to examine various possible Li^+ transport paths, which are often difficult to probe on the atomic scale by experiment alone. Five possible migration paths in the sulphate structures were examined, including all possible jumps between adjacent lithium sites, which are symmetry equivalent; these paths are labeled L1–L5 in Figure 4.3. Activation energies for these migration paths can be derived by calculating the energy of the migrating

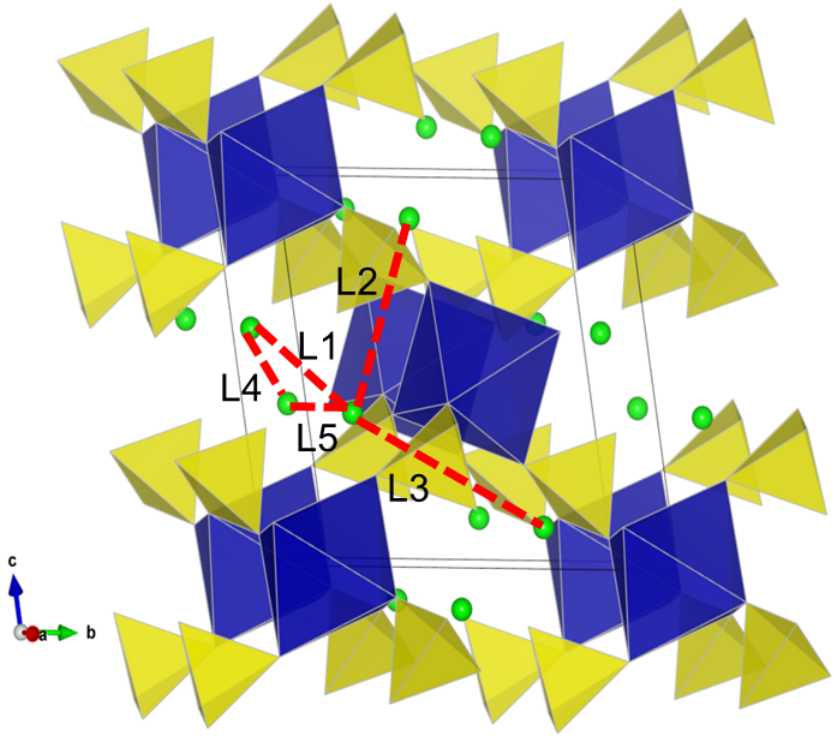

Figure 4.3: Lithium ion migration paths in $Li_2M(SO_4)_2$ (M = Fe, Mn, Co) between adjacent Li sites. Li-Li jumps considered are labeled L1-L5.

ion along the diffusion path, and are listed in Table 4.7.

The calculated activation energies reveal two main points. First, for all sulphates, the paths with lowest migration energies are found to be the L1 and L4 jumps. The results indicate that combinations of the L1 and L4 pathways consists of continuous diagonal or zigzag jumps enabling long-range diffusion along the [100] direction, i.e. along the a-axis channels (Figure 4.4), with net diffusion barriers of 0.47 eV, 0.54 eV and 0.42 eV for $Li_2Fe(SO_4)_2$, $Li_2Mn(SO_4)_2$, and $Li_2Co(SO_4)_2$ respectively.

Secondly, we note that the remaining Li migration paths considered (L2, L3 and L5) were found to have high and unfavourable activation energies ($\geq$ 1.2 eV); this is probably due to the migrating Li ion coming into close proximity of the MO_6 octahedra. Hence it would appear that the $Li_2Mn(SO_4)_2$ materials facilitates effective 1D transport of Li ions.

Thirdly, we acknowledge that Tarascon and co workers have experimentally determined the conduction activation energy in $Li_2Fe(SO_4)_2$ by AC-conductivity performed on a sintered pellet using blocking electrodes within the 200-350°C temperature range and found from linear

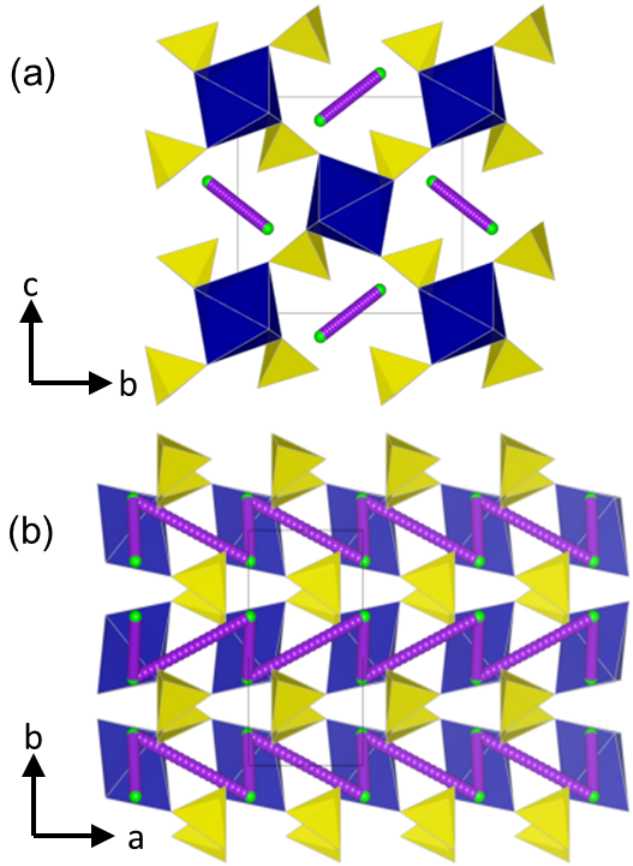

Figure 4.4: Low energy long-range Li migration pathways within [100] channel of $Li_2M(SO_4)_2$ (M = Fe, Mn, Co) combining L1 and L4 jumps. (a) view of bc-plane; (b) view of ab-plane.

extrapolation a value of ∼1.1 eV. Although this value corresponds to the total conductivity of pristine stoichiometric $Li_2Fe(SO_4)_2$ and will comprise both ionic and electronic conductivity terms. Hence, direct comparison between this measured conductivity value and the calculated migration energies for Li ion conduction (using Li vacancy sites) is not straightforward. Despite the difference, our simulations have elucidated the pathways and dimensionality of Li-ion diffusion, which are the main aims of this study.

To complement the energy minimisation calculations, molecular dynamics (MD) simulations were performed to examine the Li-ion diffusion mechanism and dimensionality within the sulphate structures. The use of such techniques have been shown to be well suited to directly probing ion transport mechanisms [210–213], and can therefore supplement the information derived from static lattice simulations. However it should be noted that the large supercells and long time-scales required are currently not accessible by *ab initio* methods.

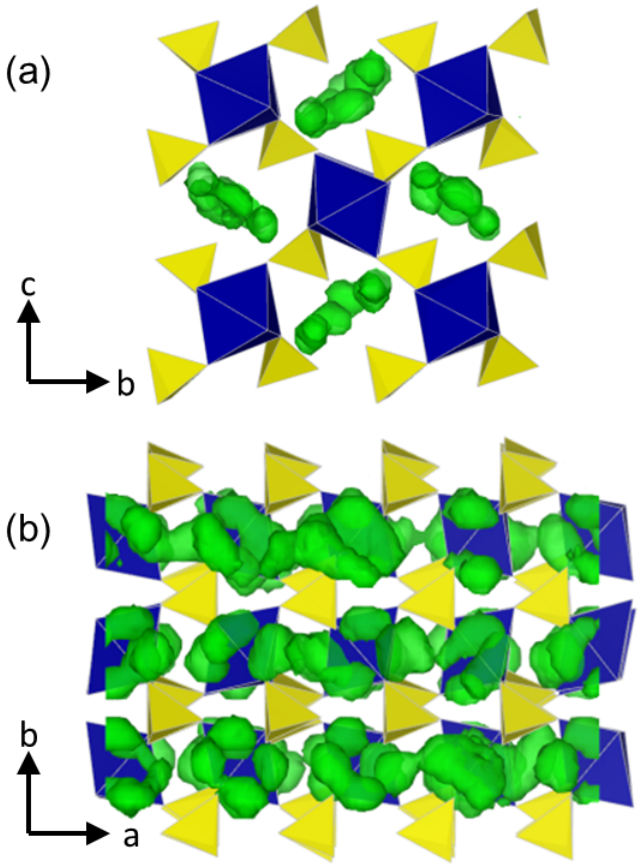

Figure 4.5: Li density plot of $Li_2M(SO_4)_2$ (M = Fe, Mn, Co) calculated using MD at 473 K, confirming low energy Li diffusion within [100] channel. (a) view of bc-plane; (b) view of ab-plane

Molecular dynamics (MD) simulations were performed with the DL_POLY code [132] using the same interatomic potentials (Table 4.4) and a P1 supercell consisting of 8 x 4 x 4 unit cells (3328 atoms) with 10% delithiation (Li vacancies were randomly distributed) to promote Li diffusion. The systems were initially equilibrated at 0 K for at least 100 thousand steps (with a time step of 0.5 fs). Using the resulting relaxed system the main simulation runs of 2 million steps were performed with an NPT ensemble, which allows for a long simulation time of 1 ns and thermal expansion of the system. Final production simulations were run according to this set-up at 50 K increments ranging between T = 323 K and 673 K with all the statistics extracted from these final production runs.

Time-averaged density plots taken from MD ion-trajectory data enable the migration paths and the regions of the structure most frequently traversed by the Li-ion to be visualised.

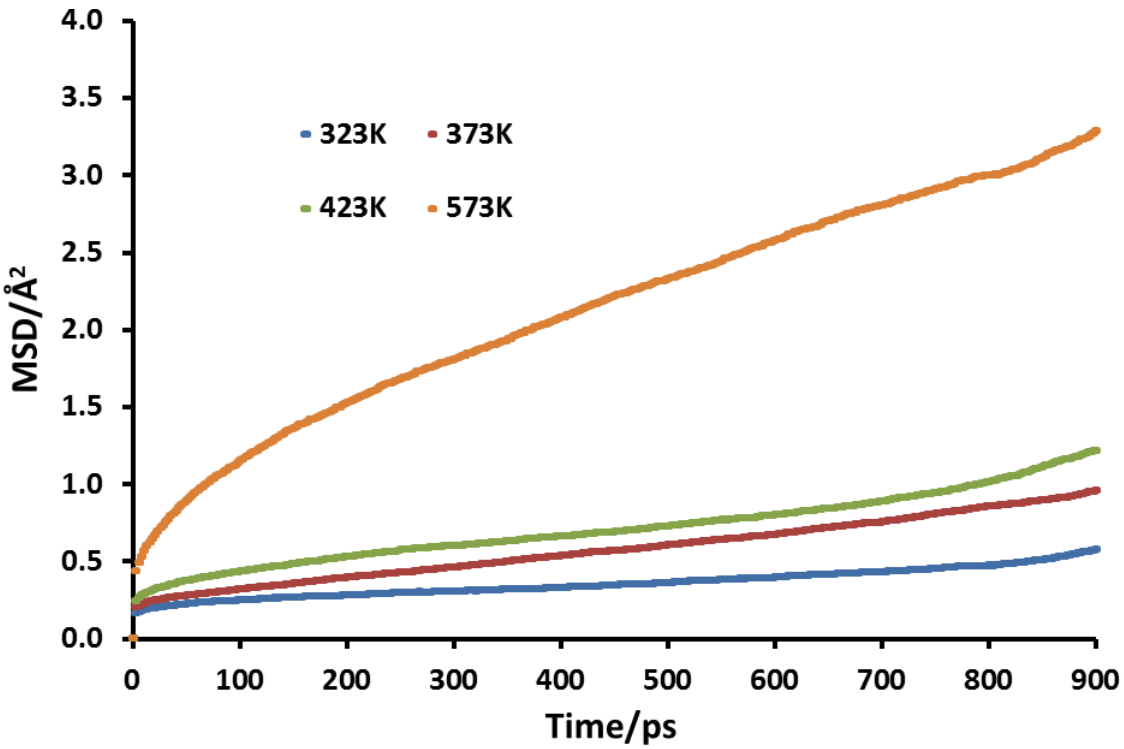

Figure 4.6: A combined mean square displacement (MSD) plot showing the diffusivity of lithium within $Li_2Fe(SO_4)_2$ at a range of temperatures.

Figure 4.5 shows the location of the Li density found from the simulation runs; this confirms the prediction of our static lattice calculations that Li diffusion will occur via combination of the L1 and L4 jumps and thus allow long-range 1D diffusion along the [100] direction. As noted, Li/M anti-site disorder is energetically unfavourable in these sulphates, and hence the 1D Li^+ diffusion is much less likely to be hindered by such defects. The MD simulations also confirm that Li diffusion involves conventional hopping between Li sites with no evidence of cooperative 'knock-on' mechanisms.

In addition, plots of the mean square displacements (MSDs), $\langle r_i^2 \rangle$, can be used to provide a valuable quantitative insight into Li diffusion. In Figure 4.6 the MSD data for the Li ion within $Li_2Fe(SO_4)_2$ is plotted as a function of time for a range of temperatures. After an initial equilibriation period, at all temperatures the MSDs increase with time indicating appreciable Li diffusivity. Diffusion coeficients (D) can be extracted from the slopes of the respective MSDs at all temperatures using the Einstein relationship for three-dimensional systems, according to the following equation:

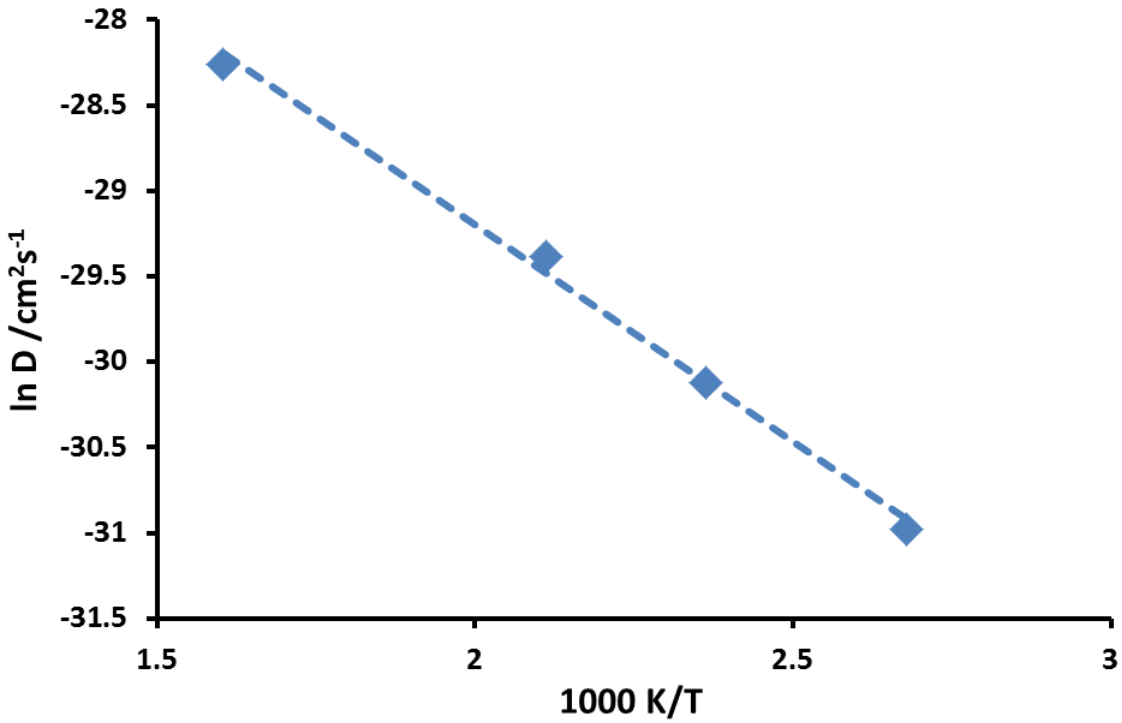

Figure 4.7: Arrhenius plot ($\ln D$ vs. $1/T$) for $Li_2Fe(SO_4)_2$.

$$\langle r_i^2 \rangle = 6Dt + B \tag{4.7}$$

where B represents a small thermal factor that arises due to atomic vibrations.

For the range of temperatures considered, our calculated diffusion coefficients, D_{Li}, are of the order of $\sim 10^{-8}$- 10^{-7} cm^2 s^{-1}. These values are consistent with those found for the related $LiFeSO_4F$ [159] and the conventional cathode $LiCoO_2$ [214–220], suggesting that these materials show similarly high lithium mobility.

The extracted diffusion coefficients are used to produce an Arrhenius plot ($\ln D$ vs. $1/T$) for $Li_2Fe(SO_4)_2$ as shown in 4.7. Analysis of such data provides an estimate of the migration activation energy (E_{act}) using the standard Arrhenius relation:

$$D = A \exp(-E_{act}/kT) \tag{4.8}$$

A migration energy of 0.22 eV is derived indicating high Li ion mobility in this sulphate based material, which is important for good rate capability. Although there is no Li-ion

conductivity data for direct comparison, our calculated migration energy is consistent with the low activation energy determined from the static lattice calculations, albeit slightly lower, probably due to the higher MD simulation temperatures.

4.2.4 Surfaces and Particle Morphology

The particle morphology is important because for facile lithium insertion/extraction the predicted 1D conduction channels must terminate at a low energy surface facet. However, direct experimental measurements on surface structures of the sulphates have not been carried out.

The surface structures in this study were simulated with potentials-based methods using the METADISE code [221]. Atoms near to the surface (region I) are allowed to relax while bulk atoms (region II), which represent the rest of the crystal, are kept fixed and ensure that all the ions in region I experience the forces associated with the rest of the crystal and that the energies are fully converged. The surface energy, γ, of a crystal face is defined as the excess in energy of a surface simulation, over the energy of a bulk system, containing the same number of atoms per unit area. The equilibrium morphology of the crystal can be obtained from the surface energies using a Wulff construction. ¥It is noted that the surface calculations on $Li_2Fe(SO_4)_2$ were carried out by Dr Christopher Eames (University of Bath, UK) using the potential model I devised as part of the collaborative work for our paper published in 2014 included in Appendix C. The results are included within this thesis to provide further insight into this family of cathode materials and for additional discussion.

We initially focus on the Fe-based material as a model system and due to its superior electrochemical activity. Thirteen low index crystal facets and their symmetry related equivalent surfaces of $Li_2Fe(SO_4)_2$ have been modelled for the first time and the resulting surface energies are listed in Table 4.8. Due to the highly interconnected nature of the FeO_6 and SO_4 polyhedra, there are no simple planar cuts that are non-polar. In all cases the layers must be reconstructed in order to remove the dipole. Using these calculated surface energies a Wulff construction of the equilibrium morphology has been made which reveals a rhombohedral-like shape (Figure 4.8). For small crystals where rearrangement of the crystal at each stage of the growth process is possible, a morphology close to the equilibrium form would be expected. However, there are no published indexed TEM images of $Li_2Fe(SO_4)_2$ for direct comparison;

Table 4.8: Calculated surface properties of $Li_2Fe(SO_4)_2$.

Surface	Surface energy (J/m^2)	Surface area in morphology (%)
{011}	0.68	65.5
{102}	0.86	2.2
{112}	0.87	0.4
{111}	0.88	1.5
{001}	0.90	1.0
{210}	0.90	27.1
{121}	0.92	2.3
{122}	0.93	0.0
{211}	0.93	0.0
{101}	0.95	0.0
{100}	0.95	0.0
{010}	1.01	0.0
{221}	1.03	0.0

indeed, such comparison is not trivial due to different experimental synthesis methods and possible non-equilibrium conditions. Nevertheless, our focus here is to reveal new information on the surface facets that are exposed, which are significant for lithium extraction/insertion processes.

The {011} facet has the lowest surface energy at 0.68 J/m^2 and makes up two thirds (65.5 %) of the overall surface area of the particle (shown in blue in Figure 4.8a). The {210} surface is the next most dominant surface comprising 27 % of the surface area (shown in red in Figure 4.8b). Earlier in this study we showed that the facile direction for lithium migration is along the channels in the [100] direction. Both the {210} and {102} facets expose these channels (Figure 4.8c). It is well known that the growth environment can have a significant effect upon the morphology of a particle and it may be possible to increase the surface area that allows facile Li access by alteration of the synthesis conditions.

Having predicted the dominance of the {011} and {210} surfaces in the morphology, we present details of both relaxed surface structures in Figure 4.9. A useful quantity here is the relaxation energy, which is the difference between the unrelaxed surface energy of the crystal cleaved from the bulk and the final relaxed surface energy. This quantity gives a measure of the degree of structural change in the surface region as the surface is formed. Structural

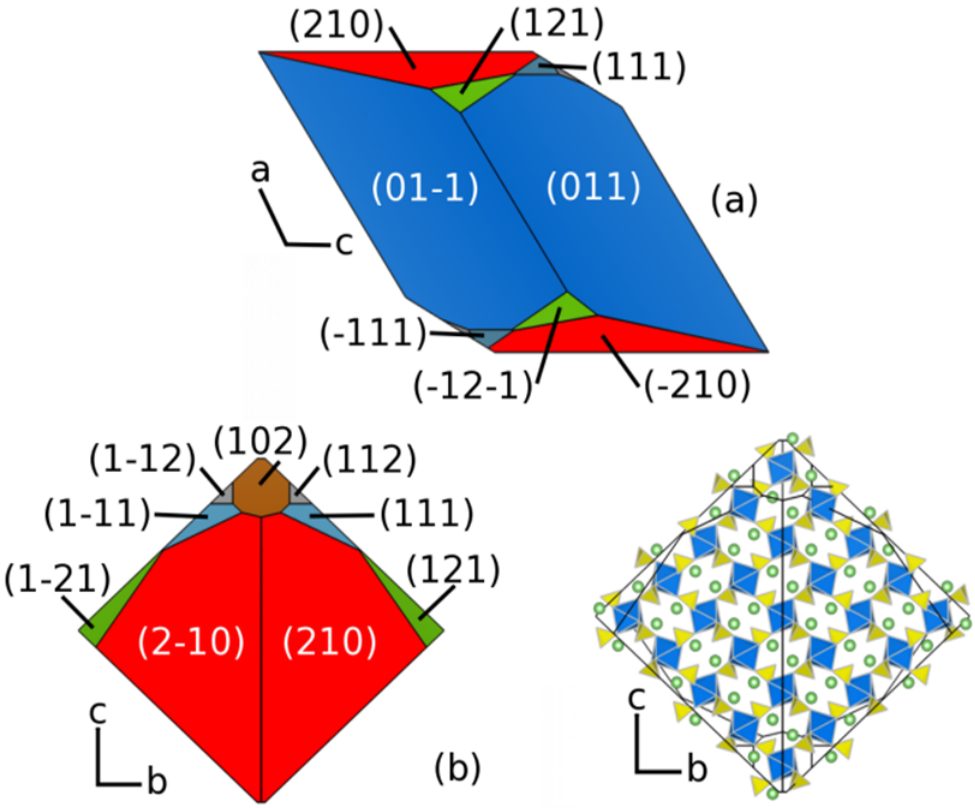

Figure 4.8: Calculated particle morphology of $Li_2Fe(SO_4)_2$; as viewed along (a) the b-axis, (b) the a-axis. In (c) the atomic structure is overlaid upon the a-axis view showing the availability of access to the 1D migration channels.

relaxations in the {011} surface are small which is reflected in the relaxation energy of 0.16 J/m^2. The largest relaxations occur in the topmost layer and these are associated with a small rotation of the terminal SO_4 units, which causes an inward displacement of 0.43 Å in the oxygen ion at the outer vertex and an inward displacement of 0.13 Å in the Li atom that is adjacent to this. There are 50 % lithium vacancies in the topmost layer and half of the SO_4 tetrahedra are absent which gives rise to a degree of rumpling.

By contrast there is significant relaxation at the {210} surface with a large relaxation energy of 1.79 J/m^2. Coordination loss is present in all of the terminal FeO_6 octahedra and the terminal SO_4 units undergo significant tilting. The near surface Li move outwards by up to 1 Å to form part of the terminal layer. As indicated in Figure 4.9(b), the prominence of the {210} surface is significant since it exposes the facile pathway for lithium ion conduction

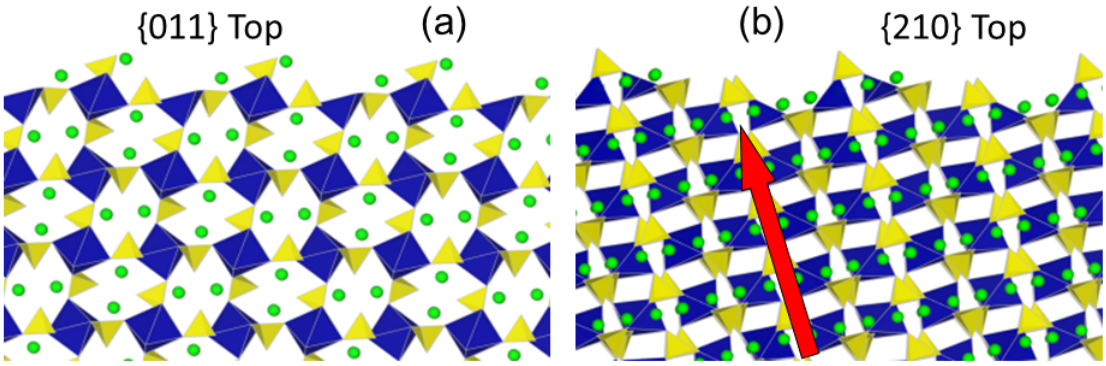

Figure 4.9: side view of relaxed (a) {011} and (b) {210} surfaces of $Li_2Fe(SO_4)_2$. The red arrow indicates the Li migration direction for {210} towards the outermost surface. For the {011} surface Li migration is into the page.

(along the [100] channel), and hence is important for the reversible insertion/de-insertion of lithium ions.

4.3 Chapter Summary

This investigation of the $Li_2M(SO_4)_2$ (M = Fe, Mn, Co) cathode materials has used a combination of DFT and atomistic simulation techniques to examine the voltage trends, Li diffusion paths and crystal morphologies. The key results are as follows:

1. The calculated cell voltage (3.91 V) for $Li_2Fe(SO_4)_2$ was found to be in excellent agreement with that determined experimentally (3.83 V). Characterisation of the experimental structure of the delithiated $LiFe(SO_4)_2$ phase was found to be important in this agreement. $Li_2Mn(SO_4)_2$ is known to be electrochemically inactive and the predicted voltage for $Li_2Co(SO_4)_2$ was found to be 5.20 V, which may be beyond the stability range of the current electrolyte.

2. Our atomistic simulations show good reproduction of the experimental crystal structures of $Li_2M(SO_4)_2$ (M = Fe, Mn, Co). The defect calculations indicate that the formation of all Frenkel, Schottky and Li/M anti-site intrinsic defects is unfavourable for all phases. In particular, the results suggest there would be no significant intrinsic concentration of Fe, Mn or Co on Li sites at operating temperatures within these sulphates. This is in contrast to the $LiFePO_4$ material, which has a small amount of Fe on Li sites.

3. Lithium diffusion simulations reveal low migration energies (∼0.4 – 0.5 eV) along the a-axis channels of $Li_2Fe(SO_4)_2$, $Li_2Mn(SO_4)_2$ and $Li_2Co(SO_4)_2$ suggesting 1D diffusion and good Li mobility which is important for favourable rate capability. MD calculations verify the 1D migration pathways along the a-axis channels, with no evidence of cooperative mechanisms.

4. The calculated equilibrium morphology of $Li_2Fe(SO_4)_2$ adopts a rhombohedral-like shape with {011} and {210} surfaces dominating. The prominence of the {210} surface is significant since it allows access to the facile pathway for lithium ion conduction (along the [100] channel), and hence is important for the reversible insertion/de-insertion of lithium ions.

Chapter 5

$LiFeSO_4OH$ Hydroxysulphate: Lithium Migration Pathways and van der Waals Effects

5.1 Background

Current studies on new cathode materials include the layered hydroxysulphate [105] ($P2_1/c$), with composition $LiFeSO_4OH$. Direct synthesis of layered $LiFeSO_4OH$ was achieved by Tarascon et al. [105]. Upon electrochemical cycling the layered phase was found to offer a voltage of 3.6 V vs. Li/Li^+ for the Fe^{2+}/Fe^{3+} redox couple with a discharge capacity in the range 100-110 mA h g^{-1}. The favourable properties of the layered $LiFeSO_4OH$ phase suggest the possibility for commercial application. Further, the layered hydroxysulphate, tavorite $FeSO_4OH$ (C2/c) has recently been investigated Tarascon et al. [107] who proposed Li could be inserted into this material at a potential of 3.2 V vs. Li/Li^+ for the Fe^{2+}/Fe^{3+} redox couple with a stable discharge capacity of $\sim$110 mA h g^{-1}. Therefore preparation of the lithiated composition of Li_xFeSO_4OH ($P\bar{1}$, where $x < 1$) for this tavorite phase occurs via electrochemical insertion of Li into $FeSO_4OH$ and not by direct synthesis.

To understand the factors influencing the electrochemical behaviour of $LiFeSO_4OH$ it is clear that fundamental knowledge of the underlying lithium transport properties and cell voltage trends is needed on the atomic scale. The present study uses well-established atomistic

simulation and density functional theory (DFT) techniques to investigate these key issues for both layered and tavorite $LiFeSO_4OH$ polymorphs.

5.2 Results and Discussion

5.2.1 Crystal Structure and Potentials

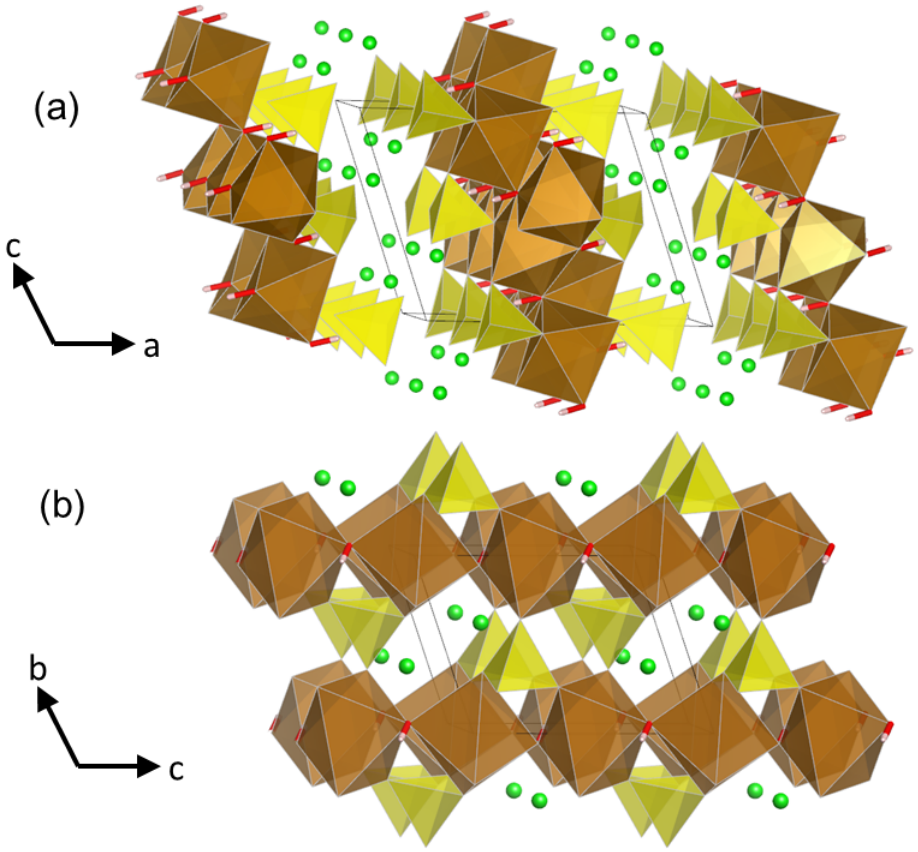

Figure 5.1: Crystal structures of (a) layered and (b) tavorite $LiFeSO_4OH$ polymorphs showing; FeO_6 octahedra (brown), SO_4 tetrahedra (yellow), OH bonds (red with cream tip) and lithium ions (green).

The starting point of the study was to reproduce the experimentally observed crystal structure exhibited by the layered $LiFeSO_4OH$ polymorph. The layered $LiFeSO_4OH$ polymorph crystallises in the monoclinic ($P2_1/c$) space group (Figure 5.1a), with edge-sharing FeO_6 octahedra that form a continuous zigzag chain that runs parallel to the b-axis direction. These chains are connected through shared oxygen vertices to form a layered structure.

On each side of the layer of FeO_6 octahedra SO_4 tetrahedra are linked via oxygen vertices, hydroxyl groups form on the remaining oxygen vertices of the FeO_6 octahedra that are not shared with either SO_4 tetrahedra or other FeO_6 octahedra. Two of the oxygen vertices of the SO_4 tetrahedra are not shared with the FeO_6 octahedra and point into the open channel between the layers where the lithium resides, and as such the lithium atoms are tetrahedrally coordinated.

The delithiated tavorite $FeSO_4OH$ also crystallises in the monoclinic space group. However with no experimental crystal structure reported for the tavorite $LiFeSO_4OH$ polymorph, the structure was set equivalent to that of the related the tavorite $LiFeSO_4F$ in the monoclinic ($P\bar{1}$) space group as suggested by Tarascon et. al [105] who observed a structural change upon discharging the tavorite $FeSO_4OH$ (C2/c). Hence the structure of the tavorite $LiFeSO_4OH$ ($P\bar{1}$) polymorph (Figure 5.1b) is believed to include chains of alternately orientated corner-sharing $FeO_4(OH)_2$ octahedra that run parallel to the c-axis direction and share hydroxyl groups located on opposite oxygen vertices. The remaining oxygen vertices of the FeO_6 octahedra are bonded to a sulphur atom forming Fe-O-S-O-Fe chains that cross-link the structure. Unlike the structure of the layered $LiFeSO_4OH$ polymorph, all of the oxygen vertices of the SO_4 tetrahedra are shared with the FeO_6 octahedra.

Employing the interatomic potential model is assessed primarily be its ability to reproduce observed crystal properties. The Li-O and O-O interatomic potentials were taken directly from the recent study of the related tavorite $LiFeSO_4F$ whilst the Fe-O interaction was obtained by refining parameters from the same study [159]. For the sulphate (SO_4) component, the inter-atomic potential model successfully formulated to simulate M_2SO_4 (M = Na, K, Rb and Cs) and XSO_4 (X = Sr, Ca, Ba) [153–156] was used. This incorporates a Morse potential to describe the intramolecular bond stretching interactions between S and O ions in the sulphate group. Similarly for the hydroxyl (OH) component, the O-H interaction was modelled using an attractive Morse potential. This approach has recently been applied successfully to protonic defects and water incorporation in fuel cell materials [157,158,212]. An additional three-body term was used for the SO_4^{2-} units to account for the angle-dependent nature and rigidity of the O-S-O bonds, as previously used for sulphates [153–156], silicates [186, 187] and phosphates [44, 45, 53]. Table 5.1 lists the interatomic potential parameters that were used in this study to simulate optimised structures of both layered and tavorite phases.

Table 5.1: Interatomic potential and shell model parameters for layered and tavorite $LiFeSO_4OH$.

(a) Buckingham			
Interaction	A / eV	ρ / Å	C / eV•Å^6
Li^{+}... $O^{0.84-}$	4787.6	0.19998	0.0
Li^{+}... $O^{1.4263-}$	4787.6	0.19998	0.0
Fe^{2+}... $O^{0.84-}$	6448.5	0.22	0.0
Fe^{2+}... $O^{1.4263-}$	6448.5	0.22	0.0
$H^{0.4263+}$... $O^{0.84-}$	981.0	0.28	0.0
$O^{0.84-}$... $O^{0.84-}$	103585.030	0.20	25.93
$O^{1.4263-}$... $O^{1.4263-}$	103585.030	0.20	25.93
(b) Morse			
	D_e (eV)	a (Å^{-1})	r_0 (Å)
$O^{0.84-}$... $S^{1.36+}$	5.0	1.20	1.505
$H^{0.4263+}$... $O^{1.4263-}$	7.0525	2.1986	0.9485
(c) Three-body			
	k / eV•rad^{-2}	ϑ_0/ °	
$O^{0.84-}$... $S^{1.36+}$... $O^{0.84-}$	15.0	109.47	
(d) Shell model			
Species	Y / e	k / eV•Å^{-2}	
Fe^{2+}	2.997	19.26	

A direct comparison of the calculated and experimental structures for the layered polymorph is given in Table 5.2, which shows that the calculated unit cell parameters deviate from the experiment by at most 0.09 Å, and in most cases by much less; the same is found for the Li-O, Fe-O, S-O and O-H bond lengths with mean deviations less than 0.03, 0.04, 0.04 and 0.06 Å respectively. The successful reproduction of the highly complex structure of the layered polymorph gives us confidence that the potential model can be used reliably for subsequent defect and migration calculations.

5.2.2 Intrinsic Atomic Defects

Insight into the defect properties of cathode materials is crucial to the full understanding of their electrochemical behaviour. As with the defect reactions in **Chapters 3** and **4**, isolated point defect (vacancy and interstitial) energies were calculated for both layered and tavorite

Table 5.2: Comparison of calculated (interatomic potentials) and experimental [105] structural parameters of layered $LiFeSO_4OH$ ($P2_1/c$)

parameter	calc.	expt.	Δ
a (Å)	9.5692	9.5147	0.0545
b (Å)	5.5756	5.5087	0.0669
c (Å)	7.2870	7.3755	-0.0885
α (°)	90.00	90.00	0.00
β (°)	109.99	109.11	0.88
γ (°)	90.00	90.00	0.00

$LiFeSO_4OH$, which were combined to determine the formation energies for Frenkel and Schottky type intrinsic defects;

Table 5.3: Energies of intrinsic atomic defects in layered and tavorite $LiFeSO_4OH$.

	Energy /eV	
Disorder type	layered	tavorite
Li Frenkel	3.55	2.63
Fe Frenkel	6.38	7.97
Schottky	20.62	19.46
Li/Fe anti-site	2.32	2.99

Examination of the resulting defect energies listed in Table 5.3 reveal two main points. First, the formation of all Frenkel and Schottky defects are unfavourable in both $LiFeSO_4OH$ polymorphs. Second, the anti-site energies are also relatively high, which suggests that there would be no significant concentration of Fe on Li sites at operating temperatures. This is in contrast with the $LiFePO_4$ material, [44, 189, 209] ($E_{\text{anti-site}}$= 1.14 eV) which exhibits cation exchange behaviour between Fe and Li sites. Therefore these results suggest that conduction "blocking" effects involving Fe on Li sites are much less likely in the $LiFeSO_4OH$ polymorphs.

5.2.3 Li-Ion Migration

Examination of the Li ion mobility and pathways in $LiFeSO_4OH$ are of vital importance when considering its charge/discharge rates. However obtaining such insight for complex polyhedral structures from experiment is far from straightforward. Using atomistic simulation techniques, it is possible to examine various possible transport paths for Li^+ conduction. Energy profiles

for conduction paths via the conventional hopping model can be derived by calculating the energy of the migrating ion in the adjacent Li sites. Relaxation of the surrounding lattice (> 1000 ions) is treated explicitly by these defect modelling methods.

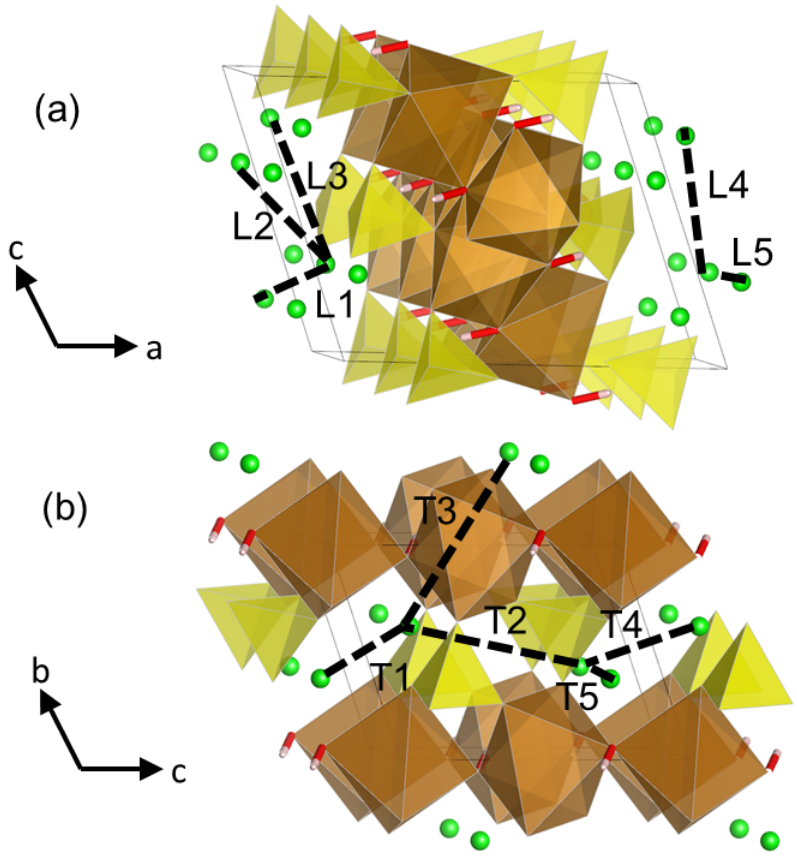

Figure 5.2: Li^+ migration pathways considered for (a) layered and (b) tavorite $LiFeSO_4OH$; labeled L1-L5 and T1-T5 respectively in order of increasing Li-Li separation.

Figure 5.2 shows the different Li diffusion pathways considered within the layered and tavorite $LiFeSO_4OH$ phases. We note that other pathways were considered but were found to be excessively high in energy (> 5 eV). Energy profiles for Li migration along each of these pathways can be mapped out. In this way the position of highest potential energy (i.e., the 'saddle-point' configuration) can be identified from which the migration energy is derived. The resulting lowest migration energies for Li diffusion along each of the five pathways are reported in Table 5.4.

Table 5.4 reveals that the L1 and L2 pathways will allow the lowest energy Li diffusion within the layered phase with energy barriers of 0.19 eV and 0.15 eV respectively. The final

Table 5.4: Energies and Li-Li separations for Li migration in (a) layered and (b) tavorite $LiFeSO_4OH$ for paths shown in Figure 5.2.

(a) layered $LiFeSO_4OH$		
Path	Distance (Å)	Activation Energy (eV)
L1	3.13	0.19
L2	3.49	0.15
L3	4.16	0.73
L4	5.15	> 2.80
L5	5.51	> 2.80
(b) tavorite $LiFeSO_4OH$		
Path	Distance (Å)	Activation Energy (eV)
T1	3.35	0.38
T2	4.75	0.70
T3	4.80	> 2.50
T4	4.90	0.72
T5	5.18	> 2.50

simulated paths for long-range Li^+ diffusion are shown in Figure 5.3. Such relatively low barriers suggest that the layered $LiFeSO_4OH$ will show high Li mobility, which is important for good electrochemical behaviour. The L1 and L2 pathways also involve the shortest Li-Li separations (3.13 Å and 3.49 Å respectively). A higher activation energy barrier of 0.73 eV is calculated for the L3 pathway which has a longer Li-Li separation of 4.16 Å. The remaining pathways (L4 and L5) are found to have high and unfavourable activation energies (> 2.80 eV) probably due to the migration distance exceeding 5 Å. Migration of Li ions from a bc-plane on one side of the layer of FeO_6 and SO_4 polyhedra to Li ions in the bc-plane on the other side would encounter separations of ≥ 8.0 Å in addition to significant steric hindrance, and needless to say these pathways are highly unfavourable.

In short, the combination of the highly favourable L1 and L2 migration pathways suggests that layered $LiFeSO_4OH$ will facilitate long-range diffusion along both the b-axis and c-axis directions, and as such the structure shows two-dimensional (2D) Li migration within the bc-plane. The final simulated paths for long-range Li^+ diffusion are shown in Figure 5.3.

For the tavorite phase Table 5.4 reveals the T1, T2 and T4 pathways have the lowest energy barriers for Li diffusion of 0.38 eV, 0.70 eV and 0.72 eV respectively. These activation energy

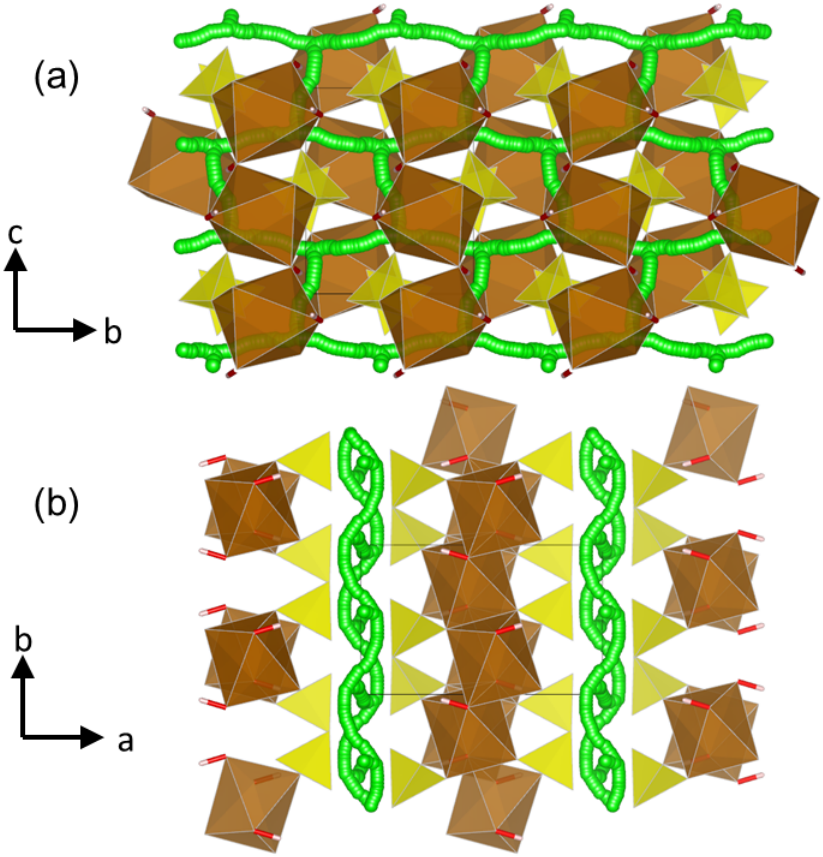

Figure 5.3: Calculated low energy pathways for long-range Li^+ migration along the b- and c-axis directions within layered $LiFeSO_4OH$ with activation energies of ≤ 0.19 eV; simulations indicate quasi-2D transport and non-linear trajectories (Li^+ pathways in green); (a) a-axis view; (b) c-axis view.

barriers for tavorite $LiFeSO_4OH$ suggest reasonable Li mobility, although they are significantly higher than the corresponding values calculated for the layered phase. The simulated paths for long-range Li^+ diffusion within tavorite $LiFeSO_4OH$ are shown in Figure 5.4. The combination of the moderately favourable T1, T2 and T4 migration pathways suggests tavorite $LiFeSO_4OH$ will facilitate long-range diffusion along both a-axis and c-axis directions, and as such the structure shows quasi-two-dimensional (2D) Li migration within the ac-plane.

Our simulations reveal curved paths between adjacent Li sites for both the layered (Figure 5.3) and tavorite phases (Figure 5.4), which produces "wave-like" trajectories for long-range migration. It is worth noting that analogous, curved Li^+ migration paths were first predicted from atomistic simulation studies of $LiFePO_4$ [44] which were subsequently confirmed by neu-

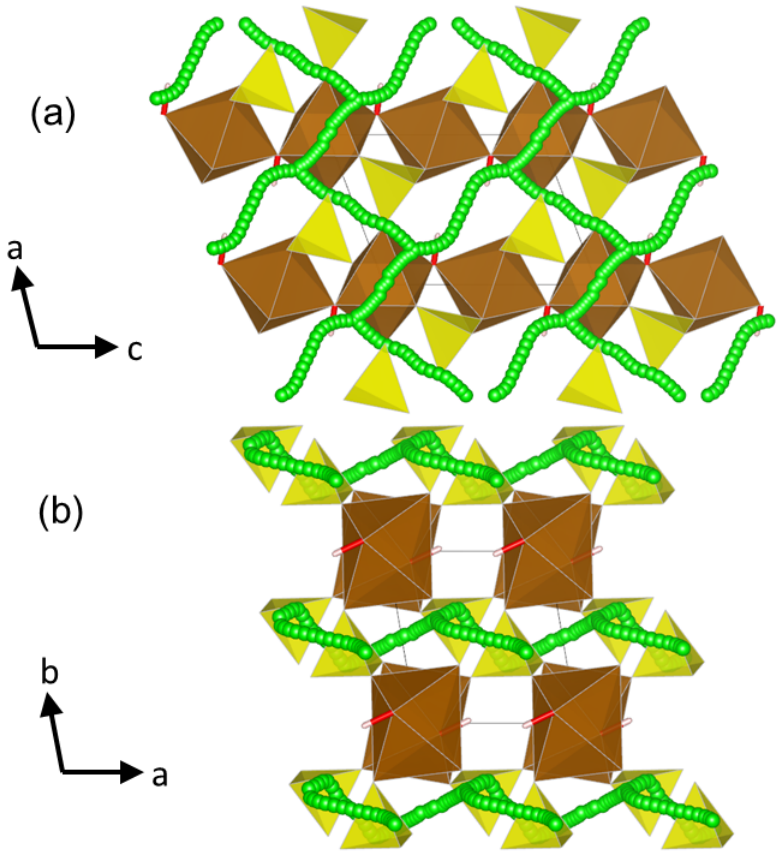

Figure 5.4: Calculated low energy pathways for long-range Li^+ migration along the a- and c-axis directions within tavorite $LiFeSO_4OH$ with activation energies of ≤ 0.72 eV; simulations indicate quasi-2D transport and non-linear trajectories (Li^+ pathways in green); (a) b-axis view; (b) c-axis view.

tron diffraction maximum entropy method (MEM) analysis [42].

5.2.4 Bulk Structure and Cell Voltages

Density functional theory calculations were performed using the plane wave code VASP [201]. Since we required optimised lattice parameters the basis set was converged against the stress which is more sensitive to an under-converged basis set than the forces. A cutoff energy of 850 eV with a k-point mesh density of at least 0.04 $Å^{-1}$ was needed to adequately converge the stress (3×6×4 grid). PAW potentials [183, 202] and the PBE exchange and correlation functional [175] were used. Our calculations employed full spin polarisation and an anti-ferromagnetic ordering of the moments on the Fe atoms was found to be lower in energy than a ferromagnetic

ordering. Anti-ferromagnetism is common in iron sulphate-based cathode materials and has been observed in the related $Li_2Fe(SO_4)_2$, $LiFeSO_4F$ and $NaFeSO_4F$ compounds [104,222–224]. DFT +U was used to correct the interactions inside the Fe d-orbitals with an effective Hubbard U_{eff} = U – J = 4 eV (J = 1 eV); this value is consistent with previous work on other Fe-based cathodes [72, 114, 225, 226]. We should emphasize that the focus of our electronic structure calculations is to enhance understanding of the trends in voltage differences which are not affected by the precise magnitude of the Hubbard U term.

Previous DFT studies on a variety of oxide electrode materials [20, 114, 204–206] have shown that such methods are well suited to probing lithium insertion/extraction properties and to predicting precise trends in cell voltages. For each polymorph we have calculated the open circuit voltage for the Fe^{2+}/Fe^{3+} redox couple using:

$$V = \frac{\epsilon\{LiFeSO_4OH\} - \epsilon\{Li_xFeSO_4OH\} - \{1-x\}\mu\{Li\}}{1-x} \tag{5.1}$$

Where $\varepsilon\{Y\}$ is the total energy of Y and x is the number of lithium atoms per formula unit removed. In practice we have removed one lithium atom per formula unit to produce the end member $FeSO_4OH$. Metallic lithium was used to calculate the chemical potential of a single lithium atom ($\mu\{Li\}$) which is standard practice for cell voltage calculations. To derive the cell voltage we have optimised the $LiFeSO_4OH$ and $FeSO_4OH$ structures and used their minimised energies in equation 5.1.

¥It is noted that the DFT investigation of layered and tavorite polymorphs of $LiFeSO_4OH$ involving the use of electronic structure methods beyond DFT+U (i.e., those that explicitly included the Van der Waals interactions) were carried out by Dr Christopher Eames (University of Bath, UK) as part of the collaborative work for our paper published in 2014 included in the appendix D. The results are included within this thesis for direct comparison with the DFT investigation of tavorite-$LiFeSO_4OH$.

As with the potentials-based calculations we have also assessed various DFT-based methods in terms of the reproduction of the known crystal properties, namely the crystal structure and the cell voltage. Structural optimisation of the as-prepared layered $LiFeSO_4OH$ ($P2_1/c$), layered $FeSO_4OH$ ($P2_1/c$) and tavorite $FeSO_4OH$ (C2/c) was performed based on the crystal structures observed experimentally [105]. As noted, there is no experimental crystal structure

reported for the tavorite $LiFeSO_4OH$ phase, and therefore the structure was set equivalent to that of the related tavorite $LiFeSO_4F$ as suggested by Tarascon et. al. [105] Cell voltage trends of $LiFeSO_4F$ polymorphs have been examined by DFT+U calculations combined with crystallographic and electrostatic analysis [227].

In many layered materials such as graphite, boron nitride and V_2O_5, long range dispersion interactions between the layers are known to be significant [228–230]. Since standard DFT methods do not include such Van der Waals (vdW) interactions we have tested a vdW enhanced DFT scheme that includes an explicit exchange correlation vdW-functional (optPBE-vdW [231]). In general, we find that this latter vdW exchange correlation functional method better reproduces the structures and voltages of the layered phase; in the remainder of this work we report results obtained in this way. We note that other recent studies have shown the significance of dispersion-corrected DFT in treating ion intercalation in graphite [232, 233] and organic cathode materials [234, 235] but with limited work on inorganic polyanion-type cathodes.

Table 5.5: Comparison of calculated (DFT and DFT+optPBE-vdW) and experimental [105] structural parameters of layered and tavorite $LiFeSO_4OH$ and $FeSO_4OH$.

Layered $LiFeSO_4OH$					
Parameter	Expt	DFT+U	Δ	DFT+U+optPBE-vdW	Δ
a (Å)	9.5147(1)	9.7470	+0.2323	9.5655	+0.0508
b (Å)	5.5087(1)	5.5424	+0.0337	5.5099	+0.0012
c (Å)	7.3755(1)	7.4956	+0.1201	7.3950	+0.0195
β (°)	109.109(6)	110.020	+0.911	109.042	-0.067
Volume (Å^3)	365.28(1)	380.46	+15.18	368.42	+0.14
Layered $FeSO_4OH$					
Parameter	Expt†	DFT+U	Δ	DFT+U+optPBE-vdW	Δ
a (Å)	9.481(3)	9.7826	+0.3016	9.3698	-0.1112
b (Å)	5.296(2)	5.4023	+0.1063	5.3258	+0.0298
c (Å)	7.207(2)	7.4670	+0.2600	7.3756	+0.1686
β (°)	110.55(3)	111.661	+1.111	112.366	+1.816
Volume (Å^3)	338.9(2)	366.76	+27.86	340.37	+1.47
Tavorite $LiFeSO_4OH$					
Parameter	Expt‡	DFT+U	Δ‡	DFT+U+optPBE-vdW	Δ‡
a (Å)	-	5.17706	-	5.12721	-
b (Å)	-	5.65299	-	5.62762	-
c (Å)	-	7.33368	-	7.22731	-
α (°)	-	106.155	-	106.582	-
β (°)	-	106.433	-	107.052	-
γ (°)	-	97.398	-	97.558	-
Volume (Å^3)	-	192.651	-	185.732	-
Tavorite $FeSO_4OH$					
Parameter	Expt	DFT+U	Δ	DFT+U+optPBE-vdW	Δ
a (Å)	5.1249	5.30239	+0.1775	5.11732	-0.0078
b (Å)	5.4512	5.29350	-0.1577	5.17238	-0.2788
c (Å)	7.1085	7.32244	+0.2139	7.30275	+0.1932
α (°)	106.24	105.741	-0.499	107.612	+1.372
β (°)	108.17	108.638	+0.468	110.432	+2.262
γ (°)	101.30	98.489	-2.811	93.001	-8.299
Volume (Å^3)	172.21	181.155	+8.895	169.916	-2.290

†Delithiated composition of $Li_{0.1}FeSO_4OH$

‡There is no available experimental structural data for tavorite $LiFeSO_4OH$

Table 5.6: Comparison of calculated and experimental cell voltages (vs. Li/Li^+) for layered and tavorite hydroxysulphates.

Technique	Layered (V)	Tavorite (V)
Experiment	3.60	3.20
DFT+U	4.28	3.40
DFT+U+optPBE-vdW	3.87	3.40

The calculated structural parameters are presented in Table 5.5. It can be seen that using an explicit van der Waals functional (DFT+U+optPBE-vdW) provides a better agreement with the experimental structures than standard DFT+U. The improvement is mainly due to a more accurate inter-layer spacing obtained by introducing dispersion interactions. The unit cell a parameter, which is almost parallel to the inter-layer direction, can be used to assess the difference in the inter-layer spacing between experiment and calculations. For $LiFeSO_4OH$ the Δa difference with experiment is reduced from +2.4 % with DFT to +0.5 % with DFT+optPBE-vdW. For $FeSO_4OH$ the Δa difference is reduced from +3.2 % to -1.2 %. We note here that the composition in the delithiated experimental data is $Li_{0.1}FeSO_4OH$; possible extraction of a further 0.1 Li per formula unit would decrease the inter-layer spacing slightly, closer to the calculated $FeSO_4OH$ structure.

Using the total energies of these relaxed structures an average intercalation voltage has been derived for each phase according to equation 5.1 and these are listed in Table 5.6. For the layered phase the cell voltage computed when van der Waals effects are not included is severely overestimated by about 0.7 V, which is unusually high for DFT+U calculations. In contrast, the calculated voltage using optPBE-vdW is 3.87 V in much better agreement with the measured value of 3.6 V.

As a comparison, we have also computed the voltage of the tavorite structure of $LiFeSO_4OH$ using both standard DFT+U and DFT+U+optPBE-vdW. The calculated voltage of 3.40 V vs. 3.20 V from experiment is not affected by the inclusion of vdW interactions; this result suggests that, as expected, dispersion interactions do not play a major role in the tavorite system. Nevertheless, the tavorite phase provides a useful 'reference' system to compare against layered $LiFeSO_4OH$ and illustrates how significant the effect of vdW interactions is on the voltage of the layered phase.

5.3 Chapter Summary

This investigation of the layered-$LiFeSO_4OH$ cathode material has used a combination of atomistic simulation and density functional theory (DFT) techniques to provide fresh insights into the defect chemistry, Li^+ migration pathways and structural van der Waals effects. For comparison, we have also investigated the possible tavorite $LiFeSO_4OH$ phase. The key results can be summarised as follows:

1. Our atomistic simulations show good reproduction of the observed structure of the layered $LiFeSO_4OH$ phase, and a realistic prediction for the tavorite $LiFeSO_4OH$ structure. The defect calculations indicate that the formation of all Frenkel, Schottky and Li/Fe anti-site intrinsic defects is unfavourable for both polymorphs. In particular, the results suggest there would be no significant intrinsic concentration of Fe on Li sites at operating temperatures in the hydroxysulphates. This is in contrast to the $LiFePO_4$ material, which has a small amount of Fe on Li sites.

2. Investigation of the lithium diffusion in layered $LiFeSO_4OH$ reveals curved pathways in the bc-plane with low migration energies ($\sim$0.2 eV), suggesting high Li mobility in a 2D network, which is important for good rate capability and capacity retention. Lithium diffusion within tavorite $LiFeSO_4OH$ is found to be parallel to the a- and c-axes and with higher activation energies ($\sim$0.7 eV) thus suggesting much slower 2D Li mobility compared to the layered polymorph.

3. DFT calculations show that there are significant inter-layer van der Waals (vdW) interactions in the layered phase, which are not fully incorporated in conventional DFT and have not been widely examined in inorganic polyanion-type cathodes. The reproduction of the experimental structure and voltage of layered $LiFeSO_4OH$ is only achieved if these dispersion forces are included through the DFT methodology. By contrast, the inclusion of vdW effects in the tavorite phase does not alter the calculated parameters, which are already in good agreement with experiment and indicate a key difference between the two $LiFeSO_4OH$ structures.

In general, this study indicates the importance of including van der Waals effects in DFT calculations on layered-structured lithium (and sodium) battery materials.

Chapter 6

Conclusions and Future Work

6.1 General Remarks

This thesis highlights recent computer modelling studies of a range of polyanion positive electrode materials for use in lithium- and sodium-ion batteries. The discovery and development of new materials are crucial for the next-generation of rechargeable lithium and sodium batteries for potential use in portable electronics and electric vehicles. Through investigation of the atomic-scale properties of these materials, I have attempted to provide further insights into the fundamental defect, ion-transport, cell voltage and surface related properties relevant to their electrochemical behaviour. Moreover, every effort has been made to make the scope of our simulations predictive in an attempt to further advance the materials science that underpins the development of rechargeable battery technology. It would appear appropriate to conclude this thesis by providing a review of the investigations undertaken; outlining the main findings and suggesting possible areas through which each study could be extended.

6.2 Pyrophosphate Cathodes $Li_2FeP_2O_7$, $Na_2FeP_2O_7$ and $Na_2MnP_2O_7$: Structural and Ion Diffusion Properties

In **chapter 3** an investigation was undertaken into the defect chemistry, Li^+ migration pathways and cation doping effects of the $Li_2FeP_2O_7$ cathode material. In addition to which the defect and Na^+ ion conduction paths in $Na_2MP_2O_7$ (M = Fe, Mn) were examined and

compared with those for $Li_2FeP_2O_7$.

(i) Conclusions: The complex experimental crystal structures of all pyrophosphates were characterised and our atomistic simulations showed good reproduction of their observed structures. Intrinsic defect calculations suggest the stability of the pyrophosphate framework towards oxygen evolution, which is important for operational safety. The most favourable intrinsic defect type is the Li/Fe and Na/M anti-site, which would be temperature dependent and hence sensitive to experimental synthesis conditions.

Lithium diffusion within $Li_2FeP_2O_7$ will follow non-linear, curved paths in the b-axis and c-axis directions via Li1/Li3 sites, which show low migration energies (0.40 eV). In comparison, both $Na_2FeP_2O_7$ and $Na_2MnP_2O_7$ are predicted to exhibit curved diffusion pathways parallel to the a-, b- and c-axes with low migration energies ($\sim$0.50 eV). Hence, in contrast to 1D diffusion in $LiFePO_4$, the pyrophosphate framework appears to support 2D Li^+ diffusion in $Li_2FeP_2O_7$ and 3D Na^+ diffusion in $Na_2MP_2O_7$, which is important for good rate capability and for the function of particles without nano-sizing. These results and the relatively low volume change on Na-ion extraction (< 5 %) are consistent with the high rate kinetics observed for $Na_2FeP_2O_7$.

For the $Li_2FeP_2O_7$ the lowest anti-site migration energies (0.59 eV) were found for net diffusion within the a-axis and b-axis channels, suggesting that the presence of any anti-site defects along these channel would have the smallest effect on lithium diffusion kinetics.

Within $Li_2FeP_2O_7$ favourable doping is found for Na^+ on the Li^+ site, and isovalent dopants (e.g., Mn^{2+}, Co^{2+}, Cu^{2+}) on the Fe^{2+} site; the latter could be used in attempts to increase the Fe^{2+}/Fe^{3+} redox potential towards 4V. In contrast, supervalent doping (especially V^{5+} and Nb^{5+}) appears unfavourable on both $Li^+$and Fe^{2+} sites; the charge-compensation mechanism found for such doping does not alter the Fe^{2+} valence state and hence is unlikely to enhance electronic conductivity.

(ii) Future work: There are several areas of future work that could be undertaken in order to extend this study. There is still much to be resolved over the exact alkali-ion diffusion mechanisms in these $Li_2FeP_2O_7$ and $Na_2MP_2O_7$ (M = Fe, Mn) cathode materials. Therefore, it would be interesting to investigate the diffusion mechanisms and dimensionality more fully for these pyrophosphate structures through MD simulations. With anti-site type defects found to be intrinsic within the pyrophosphate framework, it would be of particular interest to

compare simulations with and without a small concentration of anti-sites defects in order to assess the effect on diffusion behaviour. For the $Na_2MP_2O_7$ (M = Fe, Mn) pyrophosphates it would be interesting to use DFT techniques to study the energetics of different properties upon sodium removal. One such property of significant interest for sodium based cathodes, is the volume change. Materials found to have large changes in volume seem to show poor conductivity. With the dopant calculations for $Li_2FeP_2O_7$ revealing favourable low solution energies for isovalent dopants and recent reports of enhanced redox potentials approaching 4.0 V upon Mn^{2+} incorporation [70] an additional interesting avenue for further investigation would be to probe the $Li_{2-x}(Fe_{1-y}Mn_y)P_2O_7$ solid solution. Using DFT techniques it would be interesting to study the energetics of manganese incorporation and its effect upon the voltage. Further, the substitution of Fe ions with Mn ions in other cathode materials has been shown to lead to structural distortions, due to the presence of Jahn-Teller active Mn^{3+} ions. Therefore a full study of the surfaces and crystal morpohologies of such solid solutions could be valuable.

6.3 $Li_2M(SO_4)_2$ (M = Fe, Mn, Co) Sulphates : Atomic-Scale Studies of Lithium Diffusion, Surfaces and Voltage Trends

In **chapter 4** a combination of DFT and atomistic simulation techniques were used to provide insights into the voltage trends, Li diffusion paths and crystal morphologies of the $Li_2M(SO_4)_2$ (M = Fe, Mn, Co) cathode materials.

(i) Conclusions: The calculated cell voltage (3.91 V) for $Li_2Fe(SO_4)_2$ was found to be in excellent agreement with that determined experimentally (3.83 V). Characterisation of the experimental structure of the delithiated $LiFe(SO_4)_2$ phase was found to be important in this agreement. $Li_2Mn(SO_4)_2$ is known to be electrochemically inactive and the predicted voltage for $Li_2Co(SO_4)_2$ was found to be 5.20 V, which may be beyond the stability range of the current electrolyte.

Our atomistic simulations show good reproduction of the experimental crystal structures of $Li_2M(SO_4)_2$ (M = Fe, Mn, Co). The defect calculations indicate that the formation of all Frenkel, Schottky and Li/M anti-site intrinsic defects is unfavourable for all phases. In particular, the results suggest there would be no significant intrinsic concentration of Fe, Mn or Co on Li sites at operating temperatures within these sulphates. This is in contrast to the

$LiFePO_4$ material, which has a small amount of Fe on Li sites.

Lithium diffusion simulations reveal low migration energies ($\sim 0.4 - 0.5$ eV) along the a-axis channels of $Li_2Fe(SO_4)_2$, $Li_2Mn(SO_4)_2$ and $Li_2Co(SO_4)_2$ suggesting 1D diffusion and good Li mobility which is important for favourable rate capability. MD calculations verify the 1D migration pathways along the a-axis channels, with no evidence of cooperative "knock-on" mechanisms.

The calculated equilibrium morphology of $Li_2Fe(SO_4)_2$ adopts a rhombohedral-like shape with {011} and {210} surfaces dominating. The prominence of the {210} surface is significant since it allows access to the facile pathway for lithium ion conduction (along the [100] channel), and hence is important for the reversible insertion/de-insertion of lithium ions.

(ii) Future work: Further work investigating the activation energies for lithium diffusion within the charged state of these $LiM(SO_4)_2$ (M = Fe, Mn, Co) sulphate materials would be of interest. It would be interesting to run a series of phonon calculations to examine the lack of electrochemical activity observed for both the Mn and Co phases. In particular, for the Mn-analogue we would like to determine whether structural distortion, caused by the presence of the Jahn-Teller active Mn^{3+} within the delithiated state is a cause for the mechanical instability of this phase.

6.4 $LiFeSO_4OH$ Hydroxysulphate: Lithium Migration Pathways and van der Waals Effects

In **chapter 5**, an investigation of the $LiFeSO_4OH$ cathode material was completed using a combination of atomistic simulation and DFT techniques to examine the Li^+ migration pathways and structural van der Waals effects.

(i) Conclusions: Our atomistic simulations show good reproduction of the observed structure of the layered $LiFeSO_4OH$ phase, and a realistic prediction for the tavorite $LiFeSO_4OH$ structure. The defect calculations indicate that the formation of all Frenkel, Schottky and Li/Fe anti-site intrinsic defects is unfavourable for both polymorphs. In particular, the results suggest there would be no significant intrinsic concentration of Fe on Li sites at operating temperatures in the hydroxysulphates. This is in contrast to the $LiFePO_4$ material, which has a small amount of Fe on Li sites.

Investigation of the lithium diffusion in layered $LiFeSO_4OH$ reveals curved pathways in the bc-plane with low migration energies (∼0.2 eV), suggesting high Li mobility in a 2D network, which is important for good rate capability and capacity retention. Lithium diffusion within tavorite $LiFeSO_4OH$ is found to be parallel to the a- and c-axes and with higher activation energies (∼0.7 eV) thus suggesting much slower 2D Li mobility compared to the layered polymorph.

DFT calculations show that there are significant inter-layer van der Waals (vdW) interactions in the layered phase, which are not fully incorporated in conventional DFT and have not been widely examined in inorganic polyanion-type cathodes. The reproduction of the experimental structure and voltage of layered $LiFeSO_4OH$ is only achieved if these dispersion forces are included through the DFT methodology. By contrast, the inclusion of vdW effects in the tavorite phase does not alter the calculated parameters, which are already in good agreement with experiment and indicate a key difference between the two $LiFeSO_4OH$ structures.

In general, this study indicates the importance of including van der Waals effects in DFT calculations on layered-structured lithium (and sodium) battery materials.

(ii) Future work: It would be of interest to investigate the diffusion mechanisms and dimensionality of the different hydroxysulphate polymorphs via an extensive MD study. Addtionally, it would be interesting to investigate the 3d-metal hydroxysulphate family of cathode materials for which two new phases, namely $LiMnSO_4OH$ and $LiCoSO_4OH$, are found to crystallise with layered structures. For the Mn-analogue no electrochemical activity within the stability range of the electrolyte has been observed, whilst for the Co-analogue redox-activity in excess of 4.7 V has been observed. Therefore, using simulation techniques based on both atomistic modelling (static lattice and MD) and electronic structure (DFT) we would hope to provide systematic surveys of both materials. Once more, we would also be interested, in running phonon calculations for the Mn-analogue to investigate the lack of electrochemical activity observed for this phase.

Bibliography

[1] MacKay, D. J. C. *Sustainable Energy - without the hot air*. UIT, Cambridge, (2008).

[2] Cicerone, R. J. and Nurse, P. *Climate Change Evidence & Causes*. The Royal Society, (2014).

[3] Islam, M. S. *Journal of Materials Chemistry* **17**, 3069 (2007).

[4] Palacin, M. R. *Chemical Society Reviews* **38**, 2565 (2009).

[5] Islam, M. S. and Nazar, L. F. *Journal of Materials Chemistry* **21**, 9810 (2011).

[6] Goodenough, J. B. and Kim, Y. *Chemistry of Materials* **22**, 587 (2010).

[7] Dell, R. *Journal of Power Sources* **100**, 2 (2001).

[8] Whittingham, M. S., Savinell, R. F., and Zawodzinski, T. *Chemical Reviews* **104**, 4243 (2004).

[9] Winter, M. and Brodd, R. J. *Chemical Reviews* **104**, 4245 (2004).

[10] Bruce, P. G. *Solid State Sciences* **7**, 1456 (2005).

[11] Tarascon, J.-M. *ChemSusChem* **1**, 777 (2008).

[12] Whittingham, M. S. *Mrs Bulletin* **33**, 411 (2008).

[13] Rolison, D. R. and Nazar, L. F. *MRS Bulletin* **36**, 486 (2011).

[14] Dunn, B., Kamath, H., and Tarascon, J.-M. *Science* **334**, 928 (2011).

[15] Whittingham, M. S. *Proceedings of the IEEE* **100**, 1518 (2012).

[16] Tarascon, J. M. and Armand, M. *Nature* **414**, 359 (2001).

[17] Whittingham, M. S. *Chemical Reviews* **104**, 4271 (2004).

[18] Armand, M. and Tarascon, J. M. *Nature* **451**, 652 (2008).

[19] Nishi, Y. *Journal of Power Sources* **100**, 101 (2001).

[20] Islam, M. S. and Fisher, C. A. J. *Chemical Society reviews* **43**, 185 (2014).

[21] Hadlington, S. *Chemistry World* **4**, 58 (2007).

[22] Bruce, P. G. *Chemical Communications* , 1817 (1997).

[23] Whittingham, M. S. *Dalton Transactions* , 5424 (2008).

[24] Guyomard, D. and Tarascon, J. M. *Journal of Power Sources* **54**, 92 (1995).

[25] Chen, Z. H., Zhang, L. Z., West, R., and Amine, K. *Electrochimica Acta* **53**, 3262 (2008).

[26] Chew, S. Y., Sun, J. Z., Wang, J. Z., Liu, H. K., Forsyth, M., and MacFarlane, D. R. *Electrochimica Acta* **53**, 6460 (2008).

[27] Xie, H., Tang, Z. Y., Li, Z. Y., He, Y. B., Liu, Y., and Wang, H. *Journal of Solid State Electrochemistry* **12**, 1497 (2008).

[28] Green, M., Fielder, E., Scrosati, B., Wachtler, M., and Moreno, J. S. *Electrochemical and Solid-State Letters* **6**, A75 (2003).

[29] Larcher, D., Beattie, S., Morcrette, M., Edström, K., Jumas, J.-C., and Tarascon, J.-M. *Journal of Materials Chemistry* **17**, 3759 (2007).

[30] Beattie, S. D., Larcher, D., Morcrette, M., Simon, B., and Tarascon, J.-M. *Journal of The Electrochemical Society* **155**, A158 (2008).

[31] Ji, L., Lin, Z., Alcoutlabi, M., and Zhang, X. *Energy & Environmental Science* **4**, 2682 (2011).

[32] Deng, D., Kim, M. G., Lee, J. Y., and Cho, J. *Energy & Environmental Science* **2**, 818 (2009).

[33] Szczech, J. R. and Jin, S. *Energy & Environmental Science* **4**, 56 (2011).

[34] Lafont, U., Carta, D., Mountjoy, G., Chadwick, A. V., and Kelder, E. M. *The Journal of Physical Chemistry C* **114**, 1372 (2010).

[35] Whittingham, M. S. *Science* **192**, 1126 (1976).

[36] Padhi, A. K., Nanjundaswamy, K. S., and Goodenough, J. B. *Journal of the Electrochemical Society* **144**, 1188 (1997).

[37] Armstrong, A. R., Paterson, A. J., Robertson, A. D., and Bruce, P. G. *Chemistry of Materials* **14**, 710 (2002).

[38] Thackeray, M., David, W., Bruce, P., and Goodenough, J. *Materials Research Bulletin* **18**, 461 (1983).

[39] Lafont, U., Locati, C., Borghols, W., Lasinska, A., Dygas, J., Chadwick, A., and Kelder, E. *Journal of Power Sources* **189**, 179 (2009).

[40] Nanjundaswamy, K. S., Padhi, A. K., Goodenough, J. B., Okada, S., Ohtsuka, H., Arai, H., and Yamaki, J. *Solid State Ionics* **92**, 1 (1996).

[41] Fisher, C. A. J. and Islam, M. S. *Journal of Materials Chemistry* **18**, 1209 (2008).

[42] Nishimura, S., Kobayashi, G., Ohoyama, K., Kanno, R., Yashima, M., and Yamada, A. *Nature Materials* **7**, 707 (2008).

[43] Ellis, B. L., Lee, K. T., and Nazar, L. F. *Chemistry of Materials* **22**, 691 (2010).

[44] Islam, M. S., Driscoll, D. J., Fisher, C. A. J., and Slater, P. R. *Chemistry of Materials* **17**, 5085 (2005).

[45] Fisher, C. A. J., Prieto, V. M. H., and Islam, M. S. *Chemistry of Materials* **20**, 5907 (2008).

[46] Chung, S. Y., Choi, S. Y., Yamamoto, T., and Ikuhara, Y. *Physical Review Letters* **100** (2008).

[47] Chung, S. Y., Choi, S. Y., Yamamoto, T., and Ikuhara, Y. *Angewandte Chemie International Edition* **48**, 543 (2009).

[48] Xu, Y.-N. *Journal of Applied Physics* **95**, 6583 (2004).

[49] Rissouli, K., Benkhouja, K., Ramos-Barrado, J., and Julien, C. *Materials Science and Engineering: B* **98**, 185 (2003).

[50] Okada, S., Sawa, S., Egashira, M., Yamaki, J., Tabuchi, M., Kageyama, H., Konishi, T., and Yoshino, A. *Journal of Power Sources* **97**, 430 (2001).

[51] Yamada, A., Hosoya, M., Chung, S. C., Kudo, Y., Hinokuma, K., Liu, K. Y., and Nishi, Y. *Journal of Power Sources* **119**, 232 (2003).

[52] Yonemura, M., Yamada, A., Takei, Y., Sonoyama, N., and Kanno, R. *Journal of The Electrochemical Society* **151**, A1352 (2004).

[53] Gardiner, G. R. and Islam, M. S. *Chemistry of Materials* **22**, 1242 (2010).

[54] Yoncheva, M., Stoyanova, R., Zhecheva, E., Alcántara, R., Ortiz, G., and Tirado, J. *Electrochimica Acta* **54**, 1694 (2009).

[55] Meng, X., Dou, S., and Wang, W.-l. *Journal of Power Sources* **184**, 489 (2008).

[56] Bréger, J., Meng, Y. S., Hinuma, Y., Kumar, S., Kang, K., Shao-Horn, Y., Ceder, G., and Grey, C. P. *Chemistry of Materials* **18**, 4768 (2006).

[57] Amine, K., Tukamoto, H., Yasuda, H., and Fujita, Y. *Journal of Power Sources* **68**, 604 (1997).

[58] Zhecheva, E., Stoyanova, R., Gorova, M., Lavela, P., and Tirado, J. *Solid State Ionics* **140**, 19 (2001).

[59] Wolfenstine, J. and Allen, J. *Journal of Power Sources* **136**, 150 (2004).

[60] Yamada, A., Kudo, Y., and Liu, K.-Y. *Journal of The Electrochemical Society* **148**, A747 (2001).

[61] Yamada, A. and Chung, S. C. *Journal of the Electrochemical Society* **148**, A960 (2001).

[62] Wolfenstine, J. and Allen, J. *Journal of Power Sources* **142**, 389 (2005).

[63] Yamada, A., Kudo, Y., and Liu, K.-Y. *Journal of The Electrochemical Society* **148**, A1153 (2001).

[64] Delacourt, C., Laffont, L., Bouchet, R., Wurm, C., Leriche, J. B., Morcrette, M., Tarascon, J. M., and Masquelier, C. *Journal of the Electrochemical Society* **152**, A913 (2005).

[65] Li, G., Azuma, H., and Tohda, M. *Electrochemical and Solid-State Letters* **5**, A135 (2002).

[66] Amine, K., Yasuda, H., and Yamachi, M. *Electrochemical and Solid State Letters* **3**, 178 (2000).

[67] Nishimura, S., Nakamura, M., Natsui, R., and Yamada, A. *Journal of the American Chemical Society* **132**, 13596 (2010).

[68] Kim, H., Lee, S., Park, Y. U., Kim, J., Jeon, S., and Kang, K. *Chemistry of Materials* **23**, 3930 (2011).

[69] Barpanda, P., Ye, T., Chung, S.-C., Yamada, Y., Nishimura, S.-i., and Yamada, A. *Journal of Materials Chemistry* **22**, 13455 (2012).

[70] Furuta, N., Nishimura, S., Barpanda, P., and Yamada, A. *Chemistry of Materials* **24**, 1055 (2012).

[71] Jain, A., Hautier, G., Moore, C., Kang, B., Lee, J., Chen, H. L., Twu, N., and Ceder, G. *Journal of the Electrochemical Society* **159**, A622 (2012).

[72] Zhou, H., Upreti, S., Chernova, N. A., Hautier, G., Ceder, G., and Whittingham, M. S. *Chemistry of Materials* **23**, 293 (2011).

[73] Zhou, H., Upreti, S., Chernova, N. A., and Whittingham, M. S. *Acta Crystallographica Section E-Structure Reports Online* **67**, I58 (2011).

[74] Salah, A. A., Jozwiak, P., Garbarczyk, J., Benkhouja, K., Zaghib, K., Gendron, F., and Julien, C. M. *Journal of Power Sources* **140**, 370 (2005).

[75] Wurm, C., Morcrette, M., Rousse, G., Dupont, L., and Masquelier, C. *Chemistry of Materials* **14**, 2701 (2002).

[76] Kim, J., Middlemiss, D. S., Chernova, N. A., Zhu, B. Y. X., Masquelier, C., and Grey, C. P. *Journal of the American Chemical Society* **132**, 16825 (2010).

[77] Adam, L., Guesdon, A., and Raveau, B. *Journal of Solid State Chemistry* **181**, 3110 (2008).

[78] Masquelier, C. and Croguennec, L. *Chemical Reviews* **113**, 6552 (2013).

[79] Etacheri, V., Marom, R., Elazari, R., Salitra, G., and Aurbach, D. *Energy & Environmental Science* **4**, 3243 (2011).

[80] Gong, Z. L. and Yang, Y. *Energy & Environmental Science* **4**, 3223 (2011).

[81] Ellis, B. L. and Nazar, L. F. *Current Opinion in Solid State & Materials Science* **16**, 168 (2012).

[82] Palomares, V., Serras, P., Villaluenga, I., Hueso, K. B., Carretero-Gonzalez, J., and Rojo, T. *Energy & Environmental Science* **5**, 5884 (2012).

[83] Delmas, C., Braconnier, J. J., Fouassier, C., and Hagenmuller, P. *Solid State Ionics* **3**, 165 (1981).

[84] Komaba, S., Takei, C., Nakayama, T., Ogata, A., and Yabuuchi, N. *Electrochemistry Communications* **12**, 355 (2010).

[85] Yabuuchi, N., Kajiyama, M., Iwatate, J., Nishikawa, H., Hitomi, S., Okuyama, R., Usui, R., Yamada, Y., and Komaba, S. *Nature Materials* **11**, 512 (2012).

[86] Moreau, P., Guyomard, D., Gaubicher, J., and Boucher, F. *Chemistry of Materials* **22**, 4126 (2010).

[87] Jian, Z. L., Zhao, L., Pan, H. L., Hu, Y. S., Li, H., Chen, W., and Chen, L. Q. *Electrochemistry Communications* **14**, 86 (2012).

[88] Barker, J., Saidi, M. Y., and Swoyer, J. L. *Electrochemical and Solid State Letters* **6**, A1 (2003).

[89] Ellis, B. L., Makahnouk, W. R. M., Makimura, Y., Toghill, K., and Nazar, L. F. *Nature Materials* **6**, 749 (2007).

[90] Barpanda, P., Chotard, J. N., Recham, N., Delacourt, C., Ati, M., Dupont, L., Armand, M., and Tarascon, J. M. *Inorganic Chemistry* **49**, 7401 (2010).

[91] Ong, S. P., Chevrier, V. L., Hautier, G., Jain, A., Moore, C., Kim, S., Ma, X., and Ceder, G. *Energy & Environmental Science* **4**, 3680 (2011).

[92] Tripathi, R., Wood, S. M., Islam, M. S., and Nazar, L. F. *Energy & Environmental Science* **6**, 2257 (2013).

[93] Doeff, M. M., Ma, Y. P., Visco, S. J., and Dejonghe, L. C. *Journal of the Electrochemical Society* **140**, L169 (1993).

[94] Stevens, D. A. and Dahn, J. R. *Journal of the Electrochemical Society* **148**, A803 (2001).

[95] Tran, T. T. and Obrovac, M. N. *Journal of the Electrochemical Society* **158**, A1411 (2011).

[96] Senguttuvan, P., Rousse, G., Seznec, V., Tarascon, J. M., and Palacin, M. R. *Chemistry of Materials* **23**, 4109 (2011).

[97] Barpanda, P., Ye, T., Nishimura, S., Chung, S. C., Yamada, Y., Okubo, M., Zhou, H. S., and Yamada, A. *Electrochemistry Communications* **24**, 116 (2012).

[98] Barpanda, P., Liu, G., Ling, C. D., Tamaru, M., Avdeev, M., Chung, S.-C., Yamada, Y., and Yamada, A. *Chemistry of Materials* **25**, 3480 (2013).

[99] Kim, H., Shakoor, R. A., Park, C., Lim, S. Y., Kim, J. S., Jo, Y. N., Cho, W., Miyasaka, K., Kahraman, R., Jung, Y., and Choi, J. W. *Advanced Functional Materials* **23**, 1147 (2013).

[100] Barpanda, P., Ye, T., Avdeev, M., Chung, S. C., and Yamada, A. *Journal of Materials Chemistry A* **1**, 4194 (2013).

[101] Park, C. S., Kim, H., Shakoor, R. A., Yang, E., Lim, S. Y., Kahraman, R., Jung, Y., and Choi, J. W. *Journal of the American Chemical Society* **135**, 2787 (2013).

[102] Erragh, F., Boukhari, A., Elouadi, B., and Holt, E. M. *Journal of Crystallographic and Spectroscopic Research* **21**, 321 (1991).

[103] Reynaud, M., Ati, M., Melot, B. C., Sougrati, M. T., Rousse, G., Chotard, J. N., and Tarascon, J. M. *Electrochemistry Communications* **21**, 77 (2012).

[104] Reynaud, M., Rousse, G., Chotard, J.-N., Rodríguez-Carvajal, J., and Tarascon, J.-M. *Inorganic chemistry* **52**, 10456 (2013).

[105] Subban, C. V., Ati, M., Rousse, G., Abakumov, A. M., Van Tendeloo, G., Janot, R., and Tarascon, J.-M. *Journal of the American Chemical Society* **135**, 3653 (2013).

[106] Reddy, M. A., Pralong, V., Caignaert, V., Varadaraju, U. V., and Raveau, B. *Electrochemistry Communications* **11**, 1807 (2009).

[107] Ati, M., Sougrati, M. T., Rousse, G., Recham, N., Doublet, M. L., Jumas, J. C., and Tarascon, J. M. *Chemistry of Materials* **24**, 1472 (2012).

[108] Barker, J., Saidi, M. Y., and Swoyer, J. L. *Journal of The Electrochemical Society* **151**, A796 (2004).

[109] Padhi, A. K., Nanjundaswamy, K. S., Masquelier, C., and Goodenough, J. B. *Journal of the Electrochemical Society* **144**, 2581 (1997).

[110] Recham, N., Chotard, J. N., Dupont, L., Delacourt, C., Walker, W., Armand, M., and Tarascon, J. M. *Nature Materials* **9**, 68 (2010).

[111] Tripathi, R., Ramesh, T. N., Ellis, B. L., and Nazar, L. F. *Angewandte Chemie International Edition* **49**, 8738 (2010).

[112] Nyten, A., Abouimrane, A., Armand, M., Gustafsson, T., and Thomas, J. O. *Electrochemistry Communications* **7**, 156 (2005).

[113] Islam, M. S., Dominko, R., Masquelier, C., Sirisopanaporn, C., Armstrong, A. R., and Bruce, P. G. *Journal of Materials Chemistry* **21**, 9811 (2011).

[114] Eames, C., Armstrong, A. R., Bruce, P. G., and Islam, M. S. *Chemistry of Materials* **24**, 2155 (2012).

[115] Choi, N.-S., Chen, Z., Freunberger, S. A., Ji, X., Sun, Y.-K., Amine, K., Yushin, G., Nazar, L. F., Cho, J., and Bruce, P. G. *Angewandte Chemie International Edition* **51**, 9994 (2012).

[116] Bruce, P. G., Freunberger, S. A., Hardwick, L. J., and Tarascon, J.-M. *Nature materials* **11**, 19 (2012).

[117] Jung, H.-G., Hassoun, J., Park, J.-B., Sun, Y.-K., and Scrosati, B. *Nature chemistry* **4**, 579 (2012).

[118] Ji, X. and Nazar, L. F. *Journal of Materials Chemistry* **20**, 9821 (2010).

[119] Black, R., Adams, B., and Nazar, L. F. *Advanced Energy Materials* **2**, 801 (2012).

[120] Peng, Z., Freunberger, S. A., Chen, Y., and Bruce, P. G. *Science (New York, N.Y.)* **337**, 563 (2012).

[121] Demir-Cakan, R., Morcrette, M., Guéguen, A., Dedryvère, R., and Tarascon, J.-M. *Energy & Environmental Science* **6**, 176 (2013).

[122] Abraham, K. M. and Jiang, Z. *Journal of The Electrochemical Society* **143**, 1 (1996).

[123] Visco, S. J., Katz, B. D., Nimon, Y. S., and De-Jonghe, L. C. *Li/Air non-aqueous batteries. US Patent 20070117007* (2007).

[124] Stevens, P., Toussaint, G., Caillon, G., Viaud, P., Vinatier, P., Cantau, C., Fichet, O., Sarrazin, C., and Mallouki, M. *ECS Transactions* **28**, 1 (2010).

[125] Catlow, C. R. A. *Computer Modelling in Inorganic Crystallography* , Academic press, San Diego (1997).

[126] Catlow, C. R. A., Gale, J. D., and Grimes, R. W. *Journal of Solid State Chemistry* **106**, 13 (1993).

[127] Gale, J. D. *Journal of the Chemical Society-Faraday Transactions* **93**, 629 (1997).

[128] Islam, M. S. and Slater, P. R. *Mrs Bulletin* **34**, 935 (2009).

[129] Walsh, A., Sokol, A. A., and Catlow, C. R. A. *Computational Approaches to Energy Materials*. In Wiley-Blackwell, (2013).

[130] Koch, W. and Holthausen, M. C. (2001).

[131] Gale, J. D. and Rohl, A. L. *Molecular Simulation* **29**, 291 (2003).

[132] Smith, W. and Forester, T. R. *Journal of Molecular Graphics* **14**, 136 (1996).

[133] Smith, W., Yong, C., and Rodger, P. *Molecular Simulation* **28**, 385 (2002).

[134] Kresse, G. and Hafner, J. *Physical Review B* **49**, 14251 (1994).

[135] Kresse, G. and Furthmüller, J. *Computational Materials Science* **6**, 15 (1996).

[136] Catlow, C. R. A., Guo, Z. X., Miskufova, M., Shevlin, S. A., Smith, A. G. H., Sokol, A. A., Walsh, A., Wilson, D. J., and Woodley, S. M. *Philosophical transactions. Series A, Mathematical, physical, and engineering sciences* **368**, 3379 (2010).

[137] Catlow, C. R. A., Bell, R. G., and Gale, J. D. *Journal of Materials Chemistry* **4**, 781 (1994).

[138] Sayle, D., Catlow, C., Perrin, M., and Nortier, P. *Journal of Physics and Chemistry of Solids* **56**, 799 (1995).

[139] Leach, A. R. *Molecular Modelling, Principles and Applications.* Pearson, Prentice Hall, second edition, (2001).

[140] Shanno, D. F. *Mathematics of Computation* **24**, 647 (1970).

[141] Mills, G., Jonsson, H., and Schenter, G. K. *Surface Science* **324**, 305 (1995).

[142] Henkelman, G. and Jonsson, H. *The Journal of Chemical Physics* **113**, 9978 (2000).

[143] Henkelman, G., Uberuaga, B. P., and Jonsson, H. *The Journal of Chemical Physics* **113**, 9901 (2000).

[144] Verlet, L. *Physical Review* **159**, 98 (1967).

[145] Berendsen, H. J. C., Postma, J. P. M., van Gunsteren, W. F., DiNola, A., and Haak, J. R. *The Journal of Chemical Physics* **81**, 3684 (1984).

[146] Born, M. *Physik* **1**, 45 (1920).

[147] Buckingham, R. A. *Proceedings of the Royal Society A: Mathematical, Physical and Engineering Sciences* **168**, 264 (1938).

[148] Morse, P. *Physical Review* **34**, 57 (1929).

[149] Islam, M. S. *Journal of Materials Chemistry* **10**, 1027 (2000).

[150] Malavasi, L., Fisher, C. A. J., and Islam, M. S. *Chemical Society reviews* **39**, 4370 (2010).

[151] Kendrick, E., Kendrick, J., Knight, K. S., Islam, M. S., and Slater, P. R. *Nature Materials* **6**, 871 (2007).

[152] Clark, J. M., Nishimura, S., Yamada, A., and Islam, M. S. *Angewandte Chemie International Edition* **51**, 13149 (2012).

[153] Allan, N. L., Rohl, A. L., Gay, D. H., Catlow, C. R. A., Davey, R. J., and Mackrodt, W. C. *Faraday Discussions* **95**, 273 (1993).

[154] Redfern, S. E. and Parker, S. C. *Journal of the Chemical Society-Faraday Transactions* **94**, 1947 (1998).

[155] Sastre, G. and Gale, J. D. *Chemistry of Materials* **17**, 730 (2005).

[156] Gomez-Hortiguela, L., Cora, F., Catlow, C. R. A., and Perez-Pariente, J. *Journal of the American Chemical Society* **126**, 12097 (2004).

[157] Panchmatia, P. M., Orera, A., Kendrick, E., Hanna, J. V., Smith, M. E., Slater, P. R., and Islam, M. S. *Journal of Materials Chemistry* **20**, 2766 (2010).

[158] Stokes, S. J. and Islam, M. S. *Journal of Materials Chemistry* **20**, 6258 (2010).

[159] Tripathi, R., Gardiner, G. R., Islam, M. S., and Nazar, L. F. *Chemistry of Materials* **23**, 2278 (2011).

[160] Evjen, H. M. *Physical Review* **39**, 675 (1932).

[161] Ewald, P. P. *Ann. Phys.* **369**, 253 (1921).

[162] Catlow, C. R. A. *Solid State Ionics* **8**, 89 (1983).

[163] Dick, B. G. and Overhauser, A. W. *Physical Review* **112**, 90 (1958).

[164] Lewis, G. V. and Catlow, C. R. A. *Journal of Physics C-Solid State Physics* **18**, 1149 (1985).

[165] Mott, N. F. and Littleton, M. J. *Transactions of the Faraday Society* **34**, 485 (1938).

[166] Islam, M. S. *Molecular Simulation* **21**, 127 (1998).

[167] Kohn, W. *Reviews of Modern Physics* **71**, 1253 (1999).

[168] Thomas, L. H. *Mathematical Proceedings of the Cambridge Philosophical Society* **23**, 542 (1927).

[169] Fermi, E. *Rend. Accad. Naz. Lincei* **6**, 602 (1927).

[170] Dirac, P. A. M. *Mathematical Proceedings of the Cambridge Philosophical Society* **26**, 376 (1930).

[171] Hohenberg, P. and Kohn, W. *Physical Review* **136**, B864 (1964).

[172] Kohn, W. and Sham, L. J. *Physical Review* **140**, A1133 (1965).

[173] Schrödinger, E. *Physical Review* **28**, 1049 (1926).

[174] Born, M. and Oppenheimer, R. *Annalen der Physik* **389**, 457 (1927).

[175] Perdew, J. P., Burke, K., and Ernzerhof, M. *Physical Review Letters* **77**, 3865 (1996).

[176] Perdew, J. P. and Wang, Y. *Physical Review B* **45**, 13244 (1992).

[177] Wu, Z. and Cohen, R. *Physical Review B* **73**, 235116 (2006).

[178] Anisimov, V. I., Aryasetiawan, F., and Lichtenstein, A. I. *Journal of Physics: Condensed Matter* **9**, 767 (1997).

[179] Hubbard, J. *Proceedings of the Royal Society A: Mathematical, Physical and Engineering Sciences* **285**, 542 (1965).

[180] Anisimov, V. I., Zaanen, J., and Andersen, O. K. *Physical Review B* **44**, 943 (1991).

[181] Fock, V. *Z. Physik.* **61**, 126 (1930).

[182] Hartree, D. R. and Hartree, W. *Proc. R. Soc. Lond. A.* **150**, 9 (1935).

[183] Blochl, P. E. *Physical Review B* **50**, 17953 (1994).

[184] Payne, M. C., Arias, T. A., and Joannopoulos, J. D. *Reviews of Modern Physics* **64**, 1045 (1992).

[185] Monkhorst, H. J. and Pack, J. D. *Physical Review B* **13**, 5188 (1976).

[186] Kuganathan, N. and Islam, M. S. *Chemistry of Materials* **21**, 5196 (2009).

[187] Armstrong, A. R., Kuganathan, N., Islam, M. S., and Bruce, P. G. *Journal of the American Chemical Society* **133**, 13031 (2011).

[188] Armstrong, A. R., Lyness, C., Panchmatia, P. M., Islam, M. S., and Bruce, P. G. *Nature Materials* **10**, 223 (2011).

[189] Chen, J. J., Vacchio, M. J., Wang, S. J., Chernova, N., Zavalij, P. Y., and Whittingham, M. S. *Solid State Ionics* **178**, 1676 (2008).

[190] Li, J. Y., Yao, W. L., Martin, S., and Vaknin, D. *Solid State Ionics* **179**, 2016 (2008).

[191] Sebastian, L. and Gopalakrishnan, J. *Journal of Materials Chemistry* **13**, 433 (2003).

[192] Shimizu, D., Nishimura, S.-i., Barpanda, P., and Yamada, A. *Chemistry of Materials* **24**, 2598 (2012).

[193] Ammundsen, B., Roziere, J., and Islam, M. S. *Journal of Physical Chemistry B* **101**, 8156 (1997).

[194] Zhu, Y., Xu, Y., Liu, Y., Luo, C., and Wang, C. *Nanoscale* **5**, 780 (2013).

[195] Read, M. S. D., Saiful Islam, M., Watson, G. W., King, F., and Hancock, F. E. *Journal of Materials Chemistry* **10**, 2298 (2000).

[196] Balducci, G., Islam, M. S., Kašpar, J., Fornasiero, P., and Graziani, M. *Chemistry of Materials* **12**, 677 (2000).

[197] Freeman, C. and Catlow, C. *Journal of Solid State Chemistry* **85**, 65 (1990).

[198] Olson, C. L., Nelson, J., and Islam, M. S. *Journal of Physical Chemistry B* **110**, 9995 (2006).

[199] Braithwaite, J. S., Catlow, C. R. A., Gale, J. D., and Harding, J. H. *Chemistry of Materials* **11**, 1990 (1999).

[200] Mather, G. C., Fisher, C. A., and Islam, M. S. *Chemistry of Materials* **22**, 5912 (2010).

[201] Kresse, G. and Furthmuller, J. *Physical Review B* **54**, 11169 (1996).

[202] Kresse, G. and Joubert, D. *Physical Review B* **59**(3), 1758–1775 (1999).

[203] Mueller, T., Hautier, G., Jain, A., and Ceder, G. *Chemistry of Materials* **23**, 3854 (2011).

[204] Zhou, F., Cococcioni, M., Marianetti, C. A., Morgan, D., and Ceder, G. *Physical Review B* **70**, 23 (2004).

[205] Ceder, G., Aydinol, M. K., and Kohan, A. F. *Computational Materials Science* **8**, 161 (1997).

[206] Arrouvel, C., Parker, S. C., and Islam, M. S. *Chemistry of Materials* **21**, 4778 (2009).

[207] Van der Ven, A., Marianetti, C., Morgan, D., and Ceder, G. *Solid State Ionics* **135**, 21 (2000).

[208] Baur, W. H. *Acta Crystallographica Section B-Structural Science* **30**, 1195 (1974).

[209] Maier, J. and Amin, R. *Journal of the Electrochemical Society* **155**, A339 (2008).

[210] Khan, M. S., Islam, M. S., and Bates, D. R. *Journal of Materials Chemistry* **8**, 2299 (1998).

[211] Tealdi, C., Mustarelli, P., and Islam, M. S. *Advanced Functional Materials* **20**, 3874 (2010).

[212] Panchmatia, P. M., Orera, A., Rees, G. J., Smith, M. E., Hanna, J. V., Slater, P. R., and Islam, M. S. *Angewandte Chemie International Edition* **50**, 9328 (2011).

[213] Tealdi, C., Ferrara, C., Mustarelli, P., and Islam, M. S. *Journal of Materials Chemistry* **22**, 8969 (2012).

[214] Wang, Q. S., Sun, J. H., Chen, C. H., and Zhou, X. M. *Journal of Thermal Analysis and Calorimetry* **92**, 563 (2008).

[215] Park, M., Zhang, X., Chung, M., Less, G. B., and Sastry, A. M. *Journal of Power Sources* **195**, 7904 (2010).

[216] Jeevan-Kumar, P., Jayanth-Babu, K., Hussain, O. M., and Julien, C. M. *Ionics* **19**, 421 (2012).

[217] Zheng, W., Xu, X., Cheng, L., Shui, M., Shu, J., Gao, S., Lu, Z., Feng, L., and Ren, Y. *Ionics* **19**, 1509 (2013).

[218] West, W. C., Soler, J., Smart, M. C., Ratnakumar, B. V., Firdosy, S., Ravi, V., Anderson, M. S., Hrbacek, J., Lee, E. S., and Manthiram, A. *Journal of The Electrochemical Society* **158**, A883 (2011).

[219] Gozu, M., Świerczek, K., and Molenda, J. *Journal of Power Sources* **194**, 38 (2009).

[220] Shaju, K. M., Subba Rao, G. V., and Chowdari, B. V. R. *Journal of The Electrochemical Society* **151**, A1324 (2004).

[221] Watson, G. W., Kelsey, E. T., DeLeeuw, N. H., Harris, D. J., and Parker, S. C. *Journal of the Chemical Society-Faraday Transactions* **92**, 433 (1996).

[222] Rousse, G. and Tarascon, J. M. *Chemistry of Materials* **26**, 394 (2014).

[223] Melot, B. C., Rousse, G., Chotard, J.-N., Ati, M., Rodriguez-Carvajal, J., Kemei, M. C., and Tarascon, J.-M. *Chemistry of Materials* **23**, 2922 (2011).

[224] Melot, B. C., Rousse, G., Chotard, J.-N., Kemei, M. C., Rodriguez-Carvajal, J., and Tarascon, J.-M. *Physical Review B* **85**, 094415 (2012).

[225] Zhou, F., Cococcioni, M., Kang, K., and Ceder, G. *Electrochemistry Communications* **6**, 1144 (2004).

[226] Arroyo-de Dompablo, M. E., Armand, M., Tarascon, J. M., and Amador, U. *Electrochemistry Communications* **8**, 1292 (2006).

[227] Ben Yahia, M., Lemoigno, F., Rousse, G., Boucher, F., Tarascon, J.-M., and Doublet, M.-L. *Energy & Environmental Science* **5**, 9584 (2012).

[228] Rydberg, H., Dion, M., Jacobson, N., Schröder, E., Hyldgaard, P., Simak, S., Langreth, D., and Lundqvist, B. *Physical Review Letters* **91**, 126402 (2003).

[229] Bučko, T., Hafner, J., Lebègue, S., and Ángyán, J. G. *The journal of physical chemistry. A* **114**, 11814 (2010).

[230] Marom, N., Bernstein, J., Garel, J., Tkatchenko, A., Joselevich, E., Kronik, L., and Hod, O. *Physical Review Letters* **105**, 046801 (2010).

[231] Klimeš, J., Bowler, D. R., and Michaelides, A. *Physical Review B* **83**, 195131 (2011).

[232] Persson, K. A., Hinuma, Y., Meng, Y. S., Van der Ven, A., and Ceder, G. *Physical Review B* **82**, 125416 (2010).

[233] Wang, Z., Selbach, S. M., and Grande, T. *RSC Advances* **4**, 4069 (2014).

[234] Frayret, C., Izgorodina, E. I., MacFarlane, D. R., Villesuzanne, A., Barrès, A.-L., Politano, O., Rebeix, D., and Poizot, P. *Physical Chemistry Chemical Physics* **14**, 11398 (2012).

[235] Ramos-Sanchez, G., Callejas-Tovar, A., Scanlon, L. G., and Balbuena, P. B. *Physical Chemistry Chemical Physics* **16**, 743 (2014).

Appendix A

Glossary of electrochemistry terminology

Anode: The electrode at which oxidation occurs during the electrochemical reaction.

Capacity: For a cell this is the product of the discharge current and the length of time for which a cell can be discharged until its voltage drops below a specified level (Ah). The **theoretical capacity** is the maximum possible capacity of the active materials available. In an electrode material the capacity is equivalent to the charge stored per unit mass (**specific capacity**) or volume (**volumetric capacity**), which are respectively expressed by the units mA h g^{-1} or A h l^{-1}.

Cathode: The electrode at which reduction occurs during the electrochemical reaction.

Cell voltage: The difference in potential between the anode and the cathode.

Current density: Current flow per unit area of an electrode.

C-rate: The rate of charge/discharge defined in units of amperes. It is also known as the hourly rate, and is equivalent to the capacity of a battery divided by 1 hour.

Energy density: The gravimetric energy density defines the energy stored per unit weight (W h kg^{-1}), whilst the volumetric energy density defines the energy stored per unit volume (W h l^{-1}). This is shown by the equation $E = V_e Q$, where V_e is the potential of the electrode and Q is the capacity, the product of which is the energy density (E).

Open circuit voltage: The difference in potential between the anode and the cathode when there is no load. Upon the addition of a load the cell voltage drops to leave a smaller

potential difference between the electrodes known as the **operating voltage**, due to internal resistance and polarisation.

Potential: The energy required to move an electron into a material from infinity.

Specific energy: Per unit weight of the cell this is the energy generated (W h kg^{-1}).